SAPIENZA
UNIVERSITÀ DI ROMA

Dottorato di Ricerca in Telerilevamento

Passive Radar based on WiFi transmissions: signal processing schemes and experimental results

Candidato: Paolo Falcone

Tutor: Prof. Pierfrancesco Lombardo

Ciclo XXV

Contents

List of Figures

List of Tables

Preface

Aim of this work is to study innovative techniques and processing strategies for a new passive sensor for short range surveillance.

The principle of work of the sensor will be based on the passive radar principle, and WiFi transmissions - which usually provide Internet access within local areas - will be exploited by the passive sensor to detect, localize and classify targets.

This work fits into the framework of the research activity on passive radar systems, which has received more and more interest in last decade by the international scientific community (see, as an example, [1] and [2]). However, many of the developed passive radar systems have been conceived for long range surveillance applications (e.g., air traffic control) and are almost based on broadcast transmitters, both analogic (FM radio and UHF television broadcasts) and digital (Digital Audio Broadcasting, DAB, and Digital Video Broadcasting-Terrestrial, DVB-T).

With reference to shorter range surveillance applications, aiming at the detection and localization of designated vehicles, human beings or man-made objects, wider bandwidth signals of opportunity should be exploited to achieve the required range resolution. To this purpose, WiFi transmissions represent the more suitable solution for their characteristics of: (i) reasonable bandwidth (range resolution); (ii) coverage (wireless networking applications are proliferating at a very rapid rate for both commercial and private use); (iii) transmitted power (especially for wide areas, both in public and

private premises); and (iv) an excellent accessibility (intended as the capability of accessing a clean copy of the transmitted signal).

However effective techniques should be designed to enable the practical operation of the resulting system and to rise the specific challenges issued by advanced applications. In this work, an overview of the encountered issues and the proposed solutions are presented for the WiFi-based passive radar by giving an insight into its potentialities by means of experimental results.

In particular, the treatment is organized as follows.

In Chapter 1 the passive radar principle is illustrated together with a brief recall of the bistatic radar equation and the geometry range/Doppler frequency relationships. Chapter 2 describes the WiFi signals characteristics thus providing an input for the design of the processing strategies presented in Chapter 3 for the control of the signal Ambiguity Function. Experimental results are presented in Chapter 4 both to test the Ambiguity Function control scheme and to detect moving targets. It will be clear that the detection capabilities of the conceived system might be strongly limited by the stationary (disturbance) contributions collected with the target's echo. Thus, a proper cancellation scheme will be presented in Chapter 5 and its effectiveness will be demonstrated against the same experiments previously discussed in Chapter 4. At this stage, the overall WiFi-based passive radar processing scheme for target detection will be presented and discussed.

Aiming at moving the processing scheme toward its real time working, some of its stages have been re-designed to fit an FPGA device. The developed Simulink® models - whose effectiveness has been tested with hardware-software co-simulations - are presented in Chapter 6.

Based on the digital nature of the exploited signals of opportunity, the attractive possibility of avoiding the use of the additional receiving channel usually exploited by a passive radar to collect the transmitted signal (reference signal) is investigated in Chapter 7. This can be achieved by properly extracting the reference signal from the data collected at the surveillance receiving channel, by

exploiting the knowledge of the WiFi Standards. This approach - which might be useful for a great variety of passive radar systems - is shown to yield comparable performance with respect to the conventional approach while yielding a remarkable saving in terms of system complexity.

Chapters 8 and 9 present the processing schemes conceived to enable advanced passive radar applications. In particular, in Chapter 8 a multistatic WiFi-based passive radar system is considered to localize and track moving targets. Different localization algorithms (based on range/Doppler frequency/angle of arrival measurements) will be presented and their performance will be compared with reference to a target localization experiment. On the other hand, aiming at enabling Automatic Target Recognition procedures, Chapter 9 investigates the possibility of classify moving targets by exploiting their cross-range motion component through ISAR processing strategies. Experimental results will be shown for the case of two identical cars moving one behind the other.

Finally, Chapter 10 discusses a specific example of this type of application investigated as a part of the ATOM (Airport detection and Tracking Of dangerous Materials by passive and active sensors arrays) project funded by the EU under the 7th Framework Program for Aeronautics. In particular, the main objectives of ATOM will be briefly presented together with the results of the demonstration of the WiFi-based passive radar for detection and localization of human beings in indoor areas.

Chapter 1

Passive radar principle of work

As it is well known, conventional (active) radar systems emit pulses of radio energy which bounce off targets. By performing a matched filtering operation against the tiny part of the back-scattered energy, it is then possible to detect (and possibly localize) the target.

Unlike active radar systems, *passive bistatic radar* (PBR) systems rely on preexisting transmitter infrastructures to perform target detection which results in the exciting possibility of low cost surveillance, covert operation, reduced pollution of the electromagnetic environment, low vulnerability to deliberate interference, etc.

Three examples of application of the PBR principle, are depicted in Figure 1.1. In particular, Figure 1.1(a) refers to the case of *long range surveillance* where the PBR might be used in supporting conventional radar systems for air traffic control (an example of such an application is provided in [3], where the PBR based on Frequency Modulated - FM signals is presented). A medium range application of the PBR principle, is depicted in Figure 1.1(b) for the case of an airport ground radar. In this example, it has been assumed that

WiMAX trasmissions, as specified by the IEEE 802.16 Standards ([4]), might be used as waveform of opportunity. Finally, a short range application of the PBR principle is shown in Figure 1.1(c) for the *indoor* surveillance case, where it has been assumed that the WiFi ([5]) acces points might act as transmitters of opportunity.

Figure 1.1(a) also shows the basic PBR processing scheme. It can reasonably be assumed that many points of the basic processing scheme are in common between PBRs for different applications.

In particular, with reference to Figure 1.1(a), it can be noted that the low level signal reflected from the target is collected by the PBR receiver (surveillance channel) using a directive antenna steered toward the area where surveillance is desired. The surveillance channel should ideally collect only the signals reflected by desired targets; in reality, it is affected also by a fraction of the direct signal coming from the transmitter and received by the side/backlobe of the surveillance antenna, and by strong clutter/multipath echoes. These undesired contributions can mask the low signals reflected from targets and/or introduce false alarms. Usually, directive antennas are used which are characterized by a front to back ratio greater than 20 dB in order to partially reject the direct signal at the surveillance channel (by properly pointing the antenna whit its pattern null in the direction of the selected transmitter of opportunity). However, this approach can not yield a complete disturbance removal, so the signal collected at the reference channel is first used to remove undesired contributions on the surveillance channel. After the cancellation stage, the detection process is based on the evaluation of the bistatic range-velocity Cross-Correlation Function (2D-CCF) between the surveillance and the reference signal. A Constant False Alarm Rate (CFAR) threshold can be then applied against the obtained map to automatically detect the potential targets according to a specific CFAR detection scheme.

In the following Chapters, the main peculiarities of the WiFi-based PBR will be identified together with its potentialities. Innovative processing techniques will be then presented to rise the specific challenges issued by advanced applications.

To complete the introductory picture, the following Sections provide a brief overview of both the bistatic radar equation and the geometry relationships for passive radar.

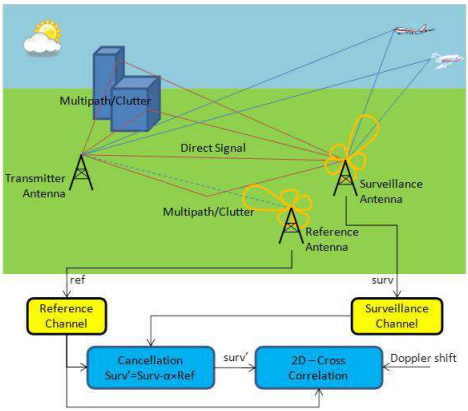

(a)

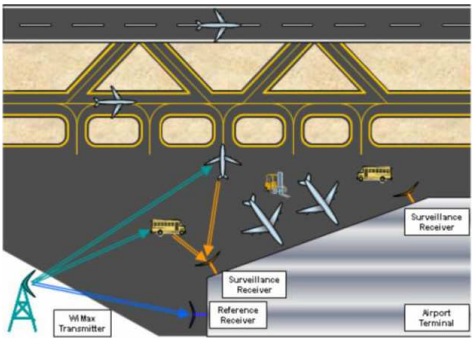

(b)

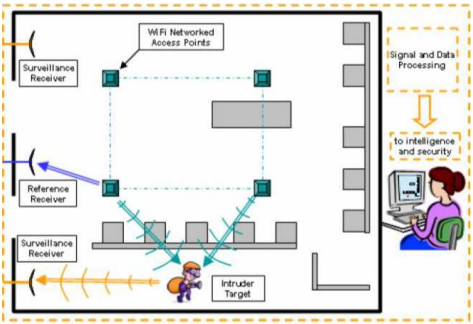

(c)

Figure 1.1: Example of Passive Radar systems: (a) for long range surveillance; (b) for medium/short range surveillance; (c) for short range/indoor surveillance.

1.1 Bistatic radar equation

With reference to the geometry sketched in Figure 1.2, the received power can be expressed as:

$$P_R = \frac{P_T G_T}{4\pi R_{\mathrm{TX,TGT}}^2} \frac{\sigma_b}{4\pi R_{\mathrm{TGT,RX}}^2} \frac{G_R \lambda^2}{4\pi} \tag{1.1}$$

where:

- P_R is the received power;
- P_T is the transmitted power;
- G_T is the transmitter antenna gain;
- G_R is the receiver antenna gain;
- λ is the signal wavelength;
- σ_b is the Bistatic Radar Cross-Section (BRCS);
- $R_{\mathrm{TX,TGT}}$ is the transmitter-target distance; and
- $R_{\mathrm{TGT,RX}}$ is the receiver-target distance.

The first factor in the right-hand side of Equation 1.1 represents the power density per surface unit emitted by the transmitter, the second factor is the portion of power scattered from the target in the receiver direction, the third factor represents the antenna effective area, expressed as a function of the receiver gain.

The received power P_R can be replaced with the smallest received power that can be detected by the radar, S_{MIN}, expressed by

$$P_R = S_{\mathrm{MIN}} = HT_0 B_n F_n \mathrm{SNR}_{\mathrm{MIN}} \tag{1.2}$$

and also the loss factors L_{PT} and L_{PR} (both lower or equal than one), which represent the losses from transmitter to target and from

receiver to target, respectively, can be included, thus obtaining the following relation:

$$\mathrm{SNR} = \frac{P_R}{P_N} = \frac{P_T G_T G_R \lambda^2 L_{\mathrm{PT}} L_{\mathrm{PR}} \sigma_b}{(4\pi)^3 R^2_{\mathrm{TX,TGT}} R^2_{\mathrm{TGT,RX}} K T_0 B_n F_n} \tag{1.3}$$

In the bistatic triangle of Figure 1.2, formed by target, transmitter and receiver, if the product between $R_{\mathrm{TX,TGT}}$ and $R_{\mathrm{TGT,RX}}$ is constant, the locus of points defined by target positions is known as Oval of Cassini. These ovals are composed by points characterized by constant power levels (SNR) at the receiver; in order to obtain the Cassini Ovals, all the parameter of the bistatic radar equation have to be considered as constant except for $R_{\mathrm{TX,TGT}}$ and $R_{\mathrm{TGT,RX}}$, so that Equation 1.3 can be written as

$$\mathrm{SNR} = \frac{k}{R^2_{\mathrm{TX,TGT}} R^2_{\mathrm{TGT,RX}}} \tag{1.4}$$

with

$$k = \frac{P_T G_T G_R \lambda^2 L_{\mathrm{PT}} L_{\mathrm{PR}} \sigma_b}{(4\pi)^3 K T_0 B_n F_n} \tag{1.5}$$

This simplified version of bistatic radar equation highlights that, for each point of the space, the SNR measured at the receiver depends on the target position with respect to both the transmitter and the receiver.

1.2 Passive Radar measurements

Typical PBR systems are able to provide, after the target detection step, an estimation of the target bistatic range and velocity. This is a quite common situation for a single passive radar sensor (single transmitter-receiver bistatic couple).

In particular:

- the bistatic range R_B (sum of the distances between the transmitter of opportunity and the target, $R_{\mathrm{TX,TGT}}$, and between the

target and the receiver $R_{\text{TGT,RX}}$) is obtained directly from the measured time of arrival τ of the target echo, according to the following expression:

$$R_B = R_{\text{TX,TGT}} + R_{\text{TGT,RX}} = \tau c \tag{1.6}$$

where c is the speed of the light; while

- the bistatic velocity v_B (the sum of the velocity components of the target along the path transmitter-target $v_{\text{TX,TGT}}$ and the path target-receiver $v_{\text{TGT,RX}}$) is obtained directly from the measured Doppler frequency f_D of the target echo:

$$v_B = v_{\text{TX,TGT}} + v_{\text{TGT,RX}} = f_D \lambda \tag{1.7}$$

where λ is wavelength of the transmitted signal of opportunity.

The measurement accuracy can be expressed as function of the bistatic resolution and the target SNR, according to [6]. For the range and the Doppler measurements, the accuracy is given by, respectively:

$$\sigma_R = \frac{\Delta R}{\sqrt{2\text{SNR}}} \tag{1.8}$$

$$\sigma_{f_D} = \frac{\Delta f_D}{\sqrt{2\text{SNR}}} \tag{1.9}$$

where, ΔR and Δf_D are, respectively, the range and the Doppler frequency bistatic resolutions.

Aiming at improving the localization and tracking capabilities of the PBR system, a third measure might be taken: the target echo Direction of Arrival (DoA). As it will briefly discussed in the following, in order to accomplish this result, it is necessary to consider a pair of antenna elements (which requires a dual channel receiving system) per each receiving sensor, as depicted in Figure 1.2.

The estimation of the DoA is based on the measure of the target echo-phase difference at the receiving channels. In particular, such

phase difference can be estimated as follows:

$$\hat{\Delta\phi} = \arg\left(\frac{x_2}{x_1}\right) \tag{1.10}$$

where x_1 and x_2 are the 2D-CCF samples at the detected target location for RX1 and RX2, respectively. With reference to Figure 1.2, it can be easily demonstrated that the phase difference in Equation 1.10 is directly related to the target DoA ϑ:

$$\Delta\phi = \frac{2\pi}{\lambda}\Delta r = 2\pi\frac{d}{\lambda}\sin\vartheta \tag{1.11}$$

where d is the distance between the receiving antennas. Thus, the DoA can be evaluated as:

$$\text{DoA} = \hat{\vartheta} = \text{asin}\left[\frac{\hat{\Delta\phi}}{2\pi}\frac{\lambda}{d}\right] \tag{1.12}$$

The DoA measurement accuracy can be expressed as (see Appendix 1.A for details):

$$\sigma_{\text{DoA}} = \frac{\lambda}{2\pi d\cos\vartheta\sqrt{2\text{SNR}}} \tag{1.13}$$

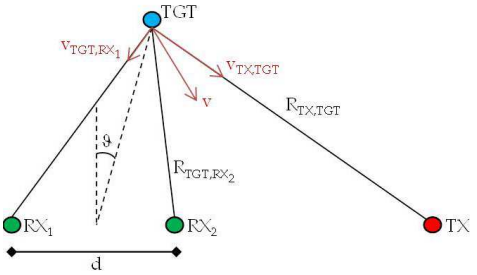

Figure 1.2: Bistatic geometry and passive radar measurements.

1.A Direction of Arrival measurement accuracy

In this Section, an expression for the Direction of Arrival measurement accuracy is derived. With reference to the sketch of Figure 1.2, we assume that the 2D-CCF samples at the detected target location for RX1 and RX2 are, respectively:

$$x_1 = A\exp(-\iota\Delta\phi/2) + n_1 \tag{1.14}$$

$$x_2 = A\exp(\iota\Delta\phi/2) + n_2 \tag{1.15}$$

where A is the complex amplitude ($A = |A|\exp(\iota\phi_0)$), $\Delta\phi$ is the phase difference at the receiving channels due to the path difference and n represents the system noise.

The phase difference can be estimated as the argument of the ratio x_2/x_1, we obtain:

$$\frac{x_2}{x_1} = \frac{A\exp(\iota\Delta\phi/2) + n_2}{A\exp(-\iota\Delta\phi/2) + n_1} = \exp(\iota\Delta\phi)\frac{1 + n_2/A\exp(\iota\Delta\phi/2)}{1 + n_1/A\exp(-\iota\Delta\phi/2)} \tag{1.16}$$

As a consequence, the estimation of the phase difference is given by the sum of the actual value and an error component:

$$\hat{\Delta\phi} = \Delta\phi + \arg\underbrace{\left\{\frac{1 + n_2/A\exp(\iota\Delta\phi/2)}{1 + n_1/A\exp(-\iota\Delta\phi/2)}\right\}}_{X} = \tag{1.17}$$

$$= \Delta\phi + \mathrm{Im}\{\ln\{X\}\}$$

Thus, the error component in the estimation of the phase difference is given by:

$$e_{\Delta\phi} = \mathrm{Im}\{\ln\{X\}\} \tag{1.18}$$

The term X in Equation 1.17 can be written as:

$$X = \frac{1 + \frac{n_2'}{|A|}}{1 + \frac{n_1'}{|A|}} \tag{1.19}$$

where n_1' and n_2' are phase-shifted versions of the system noise. Thus, its natural logarithm, for A greater than the noise component, become:

$$\ln(X) \approx \frac{1}{|A|}(n_2' - n_1') \tag{1.20}$$

By substituting into Equation 1.18 one obtains:

$$e_{\Delta\phi} = \mathrm{Im}\{\ln\{X\}\} = \frac{1}{|A|}(n_{2I}' - n_{1I}') \tag{1.21}$$

Its mean value and variance can be evaluated under the assumption that the system noise is Gaussian distributed with zero mean and variance σ_n^2.

$$E\{e_{\Delta\phi}\} = 0 \tag{1.22}$$

$$E\{e_{\Delta\phi}^2\} = \frac{1}{|A|^2} E\left\{(n_{2I}' - n_{1I}')^2\right\} = \frac{\sigma_n^2}{|A|^2} = \frac{1}{\mathrm{SNR}} \tag{1.23}$$

The Direction of Arrival ϑ is directly evaluated from the measured phase difference:

$$\hat{\vartheta} = \mathrm{asin}\left(\frac{\hat{\Delta\phi}\lambda}{2\pi d}\right) = \mathrm{asin}\left(\frac{\Delta\phi\lambda}{2\pi d} + \frac{e_{\Delta\phi}\lambda}{2\pi d}\right) \tag{1.24}$$

For small errors, the equation above can be approximated as follows:

$$\begin{aligned}\hat{\vartheta} &\approx \mathrm{asin}\left(\frac{\Delta\phi\lambda}{2\pi d}\right) + \frac{1}{\sqrt{1 - \left(\frac{\Delta\phi\lambda}{2\pi d}\right)^2}} \frac{e_{\Delta\phi}\lambda}{2\pi d} = \\ &= \vartheta + \frac{1}{\sqrt{1 - \sin^2\vartheta}} \frac{e_{\Delta\phi}\lambda}{2\pi d} = \vartheta + \frac{\lambda}{2\pi d \cos\vartheta} e_{\Delta\phi}\end{aligned} \tag{1.25}$$

Thus the error on the estimation of the Direction of Arrival ϑ is:

$$e_\vartheta = \frac{\lambda}{2\pi d \cos\vartheta} e_{\Delta\phi} \tag{1.26}$$

which has mean value and variance given by:

$$E\{e_\vartheta\} = 0 \tag{1.27}$$

$$E\{e_\vartheta^2\} = \left(\frac{\lambda}{2\pi d \cos\vartheta}\right)^2 E\{e_{\Delta\phi}^2\} = \left(\frac{\lambda}{2\pi d \cos\vartheta}\right)^2 \frac{1}{\mathrm{SNR}} \tag{1.28}$$

The expression in Equation 1.28 gives the accuracy of the Direction of Arrival measurement.

Chapter 2

WiFi waveform and Ambiguity Function characteristics

In this Chapter the main characteristics of IEEE 802.11 Standards ([5]) are summarized and the corresponding Auto-Correlation Function (ACF) is evaluated and analyzed according to the results reported in [7]. In particular, the analysis is reported for the cases of the most common transmission modulations foreseen by IEEE Standards.

Finally, the functional requirements to make the WiFi-based PBR properly working, are identified.

2.1 IEEE Standard

A number of IEEE 802.11 standards have been developed and further versions are being investigated ([5]). The three most commonly being deployed are 802.11a, 802.11b and 802.11g. 802.11a is

only adopted in the Regulation Domain of the United States while 802.11g represents the third generation of this wireless networking standards after 802.11 and 802.11b and maintains a full compatibility with the older standards. According to the European regulatory domain, IEEE Standards 802.11b and 802.11g operate in the 2.4 GHz band which is organized in 13 channels spaced 5 MHz apart (channel 1 at 2.412 GHz, channel 2 at 2.417 GHz, and so on, channel 13 at 2.447 GHz).

Moreover, the IEEE 802.11 standards allow different data rates and operate according to different frequency channels plans. The transmission is of a pulsed type with varying and unpredictable pulse durations depending on the PLCP Protocol Data Unit (PPDU) format and on the data frame size. The different data rates are achieved by exploiting different modulations and coding schemes according to the physical layer (PHY) specifications adopted by each standard (see Table 2.1).

Standard/PHY	Data Rate (Mbps)	Modulation	Base-band modulation and coding scheme
802.11 + 802.11b + 802.11g /DSSS	1	DSSS	DBPSK + Barker-11
	2	DSSS	DQPSK + Barker-11
802.11b + 802.11g /HR-DSSS	5.5	DSSS	CCK + 4 bit/symbol
	11	DSSS	CCK + 8 bit/symbol
802.11a + 802.11g / OFDM + ER-PHY	6	OFDM	BPSK + coding rate 1/2
	9	OFDM	BPSK + coding rate 3/4
	12	OFDM	BPSK + coding rate 1/2
	18	OFDM	BPSK + coding rate 1/2
	24	OFDM	BPSK + coding rate 1/2
	36	OFDM	BPSK + coding rate 1/2
	48	OFDM	BPSK + coding rate 1/2
	54	OFDM	BPSK + coding rate 1/2

Table 2.1: 802.11 Standards: modulations and coding schemes.

Specifically, the Direct Sequence Spread Spectrum (DSSS) PHY provides a wireless LAN with 1 Mbit/s and 2 Mbit/s data payload communication capability while data payload communication capability equal or higher than 5.5 Mbit/s is provided by exploiting the High Rate DSSS (HR-DSSS) PHY and the Orthogonal Frequency

Division Multiplexing (OFDM) PHY. As it is apparent, in practical situations the IEEE 802.11 transmitter may be broadcasting a mix of signals with data rates dependent primarily on user range/signal strength. Moreover, an IEEE 802.11 AP periodically transmits a regular Beacon signal broadcasting its presence and channel information. To allow the coexistence of stations capable of different modulation schemes in a wireless LAN, the AP usually uses the DSSS PHY for the Beacon frames.

The above characteristics obviously affect the performance of a passive radar exploiting wireless network transmissions. In fact target detection in a PBR system is mainly based on the evaluation of a 2D Matched Filter output yielding the typical Range-Velocity map. This is obtained by cross-correlating the surveillance signal $s_{\text{surv}}(t)$ with Doppler shifted replicas of the reference signal $s_{\text{ref}}(t)$. Assuming that the received signals are sampled with sampling frequency $f_s = 1/T_s$, the discrete implementation of the 2D Cross-Correlation Function (2D-CCF) is given by:

$$C[l,p] = \left| \sum_{i=0}^{N_{int}-1} s_{\text{surv}}[i] \cdot s^*_{\text{ref}}[i-l] \cdot \mathrm{e}^{-\iota 2\pi \frac{pi}{N_{int}}} \right|^2 \tag{2.1}$$

where:

- l is the time bin representing the time delay $\tau[l] = lT_s$; the time delay can be converted in a bistatic range difference by defining the corresponding range bin as $\Delta R[l] = c\tau[l]]$;

- p is the Doppler bin representing the Doppler frequency $f_D[p] = p/(N_{int}T_s)$, being N_{int} the number of integrated samples and $N_{int}T_s$ the coherent processing interval (CPI); the Doppler frequency can be converted in a bistatic velocity by defining the corresponding velocity bin as $\Delta v[l] = \lambda f_D[p]$.

Based on the pulsed nature of WiFi transmissions and observing that the pulse duration is significantly smaller that the CPI required to

achieve the desired signal-to-noise ratio (SNR) and Doppler resolution for the considered applications, Equation 2.1 can be approximated as follows:

$$C[l,p] \approx \left| \sum_{m=0}^{M-1} \mathrm{e}^{-\iota 2\pi \frac{pi_m}{N_{int}}} \sum_{n=0}^{N_m-1} s_{\mathrm{surv}}[i_m+n] \cdot s^*_{\mathrm{ref}}[i_m+n-l] \right|^2 = \\ = \left| \sum_{m=0}^{M-1} \mathrm{e}^{-\iota 2\pi \frac{pi_m}{N_{int}}} \chi^{(m)}[l] \right|^2 \quad (2.2)$$

where M is the number of pulses transmitted during the CPI, N_m is the number of samples in the mth pulse, i_m is the time index corresponding to the first sample of the mth pulse, and $\chi^{(m)}[l]$ is the lth sample of the temporal CCF among the surveillance and the reference signal evaluated over the mth pulse. As is apparent, Equation 2.2 can be practically evaluated by cross-correlating the surveillance signal with the reference signal on a pulse basis and coherently integrating the obtained results over consecutive pulses.

As well known, a target at given delay and Doppler would appear as a peak at the corresponding location in the Range-Velocity map. However, it should compete with the disturbance contributions which mainly consist of the sidelobes arising from other strong peaks in the map, due to both stationary scatterers and other strong targets returns. Therefore, it is apparent that the detection performance of a WiFi-based PBR might be strongly limited by the strong sidelobe structures appearing in the exploited signal Ambiguity Function (AF) which might be responsible for significant masking effects even in the presence of a significant range-Doppler separation.

A detailed analysis of the WiFi signal AF has been presented in [7] distinguishing between different signal types based on different modulations and coding schemes. In the following, those results are briefly summarized since they represent an input for the work reported in this document. Particularly, the analysis is organized in AF characteristics along the time delay (range) dimension and AF

characteristics along the Doppler frequency (velocity) dimension.

2.2 AF characteristics

The study reported in [7] demonstrated that both DSSS and OFDM transmissions are characterized by quite nice AF properties in the Doppler dimension. Specifically, the AF sidelobes in the Doppler dimension are mainly related to the temporal windowing and can be reasonably controlled by exploiting standard weighting networks. The Doppler resolution is limited by the integration time thus it can be increased by using a long train of consecutive pulses. However, it should be noted that this could yield Doppler ambiguities depending on the temporal separation between the integrated pulses; this parameter corresponds to the passive radar PRT (Pulse Repetition Time) which, in this case, is strongly time-varying and unpredictable. Such an effect will be evaluated against simulated data in Section 3.2.

A different behaviour is observed for the AF in the Delay dimension when different modulations are considered.

In particular, by exploiting a Complementary Code Keying (CCK) baseband modulation scheme, HR-DSSS signals yield very low AF sidelobes level. This is clearly shown in Figure 2.1(a) which reports the temporal Auto-Correlation Function (ACF) for a simulated HR-DSSS PHY-based signal of duration 0.25 s. A delay extent of 5 μs has been considered which corresponds to a monostatic range extent of 750 m. As it is apparent, a Peak-to-Sidelobe Ratio (PSR) greater than 50 dB is obtained.

Figure 2.1(b) reports the temporal ACF obtained for a simulated OFDM PHY-based signal of duration 0.25 s (blue curve with the circle markers). In this case, due to the rectangular shape of the corresponding spectrum, a PSR of about 13 dB is obtained which can be significantly improved by using standard weighting networks in the frequency domain. Moreover a range ambiguity appears at $\tau = T_{FFT} = 3.2$ μs, being T_{FFT} the useful symbol duration, due

to the insertion of a guard interval of duration $T_{GI} = 0.8$ μs that cyclically extends the OFDM symbol. Such range ambiguity shows a quite high level corresponding to the ratio $T_{FFT}/T_{GI} = 4$ ($PSR = 20\log(4) = 12$ dB). However, this strong peak can be easily removed by exploiting the guard interval blanking approach proposed in [8]. As an example Figure 2.1(b) reports the results obtained after the application of a Hamming weighing network and a guard interval blanking (black curve with the triangular markers). As is apparent, the range ambiguity has been effectively removed with only a limited loss in SNR. Moreover we notice that the Hamming window does not allow to obtain the theoretical PSR of 43 dB; this is mainly due to the discontinuities of the OFDM signal spectrum since the central sub-carrier is not exploited by the modulation scheme ([5]). However, a PSR approximately equal to 27 dB is obtained.

When exploiting DSSS transmissions (Figure 2.1(c)) a PSR lower than 21 dB is obtained. In this case, according to the DSSS PHY specifications, the baseband signal is chipped at 11 MHz with an 11-chip PN code. The following 11-chip Barker sequence is used: c=[+1, -1, +1, +1, -1, +1, +1, +1, -1, -1, -1], where the leftmost chip is output first in time. The first chip is aligned at the start of a transmitted symbol so that each symbol duration T_{SYM} is exactly 11 chips long ($T_{SYM} = 1$ μs).

Figure 2.1(c) reports the temporal ACF obtained for a simulated DSSS PHY-based signal of duration equal to 0.25 s. As demonstrated in [7], it is dominated by the ACF of the 11-chip Barker code which yields five identical lobes on both sides of the main-lobe with a temporal separation equal to $2T_C$, being $T_C = T_{SYM}/11$ μs the chip duration, and a PSR equal to $20\log(11) = 20.8$ dB. Moreover, additional strong sidelobes appear at delays multiple of T_{SYM} ($k \cdot 150$m). These sidelobe structures are due to the cyclical repetition of the Barker code and their level equals the average correlation among consecutive symbols of the simulated data frame of finite duration. Thus, assuming a random transmission and reasonably large integration times, the corresponding PSR may be significantly greater than that due to the Barker code sidelobes. However such

additional sidelobes structures should not be a-priori neglected since their level is highly time-varying and strongly depends on the signal content. As an example, the PSR could be seriously degraded if identical pulses of limited duration are periodically transmitted, as in the case of the Beacon frame. In fact, even increasing the integration time, the actual cross-correlation among consecutive symbols is lower bounded by the cross-correlation evaluated over the single pulse which consists of a limited number of symbols.

Notice that both the range sidelobes related to the Barker code adopted by the DSSS modulation and those depending on the average cross-correlation among consecutive transmitted symbols cannot be counteracted by using standard weighting networks.

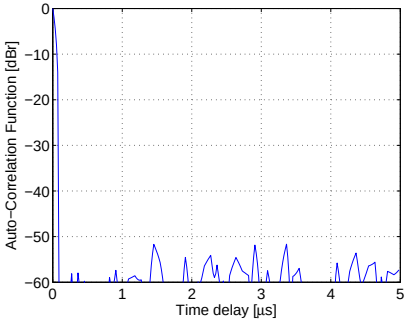

(a)

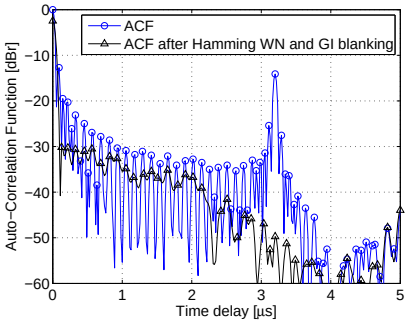

(b)

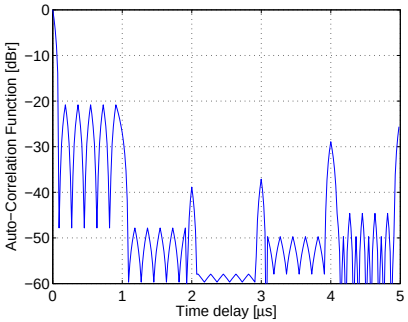

(c)

Figure 2.1: Auto-Correlation Function for simulated signals of duration 0.25 s based on (a) HR-DSSS PHY; (b) OFDM PHY; (c) DSSS PHY.

2.3 Conclusions and requirements for passive radar

As is apparent, if the considered waveform is exploited for PBR surveillance, the target returns are likely to be masked by the high level sidelobes resulting from the disturbance contributions (direct signal breakthrough and multipath reflections), even in the presence of a significant range-Doppler separation.

This also applies to the case of mixed transmissions including HR-DSSS and OFDM pulses. In fact it has to be noticed that DSSS pulses are usually present in any arbitrary signal fragment transmitted by a IEEE 802.11 AP since such modulation is the most commonly adopted (at least, it is exploited for the regularly emitted Beacon pulse interspersed with data signals). Obviously the resulting AF for a mixed train of pulses shows average properties between the different pulses types; therefore, depending on the mixing percentage, it might be dominated by the AF of the DSSS PHY-based pulses. Moreover, the useful dynamic range guaranteed by standard weighting network for both HR-DSSS and OFDM signals may still be insufficient in high clutter/multipath environment.

The undesired masking effect may be counteracted based on two different approaches:

1. designing proper filters for the control of the sidelobes level of the DSSS signal ACF;

2. defining effective algorithms for the removal of the undesired contributions in the received signal.

Notice that the above approaches may be jointly applied to improve the performance of the resulting system by maximizing the useful dynamic range for target detection.

Chapter 3

Control of the WiFi transmissions AF for passive radar

In this Chapter proper techniques are introduced to guarantee an acceptable useful dynamic range of the WiFi signal AF. The treatment is organized in PSR control along the range and the Doppler frequency dimensions of the signal AF. The effectiveness of the proposed techniques is then demonstrated against simulated data by means of a software tool developed by the author according to the IEEE Standars [5].

Finally, the WiFi-based passive radar processing scheme for AF control is presented.

3.1 PSR control along the Range dimension

In this section, proper techniques are introduced to reduce the sidelobes of the DSSS signal ACF in the range dimension. Specifically, two different filters are presented for range sidelobes reduction by addressing separately those related to the Barker code adopted by the DSSS modulation and those depending on the average cross-correlation among consecutive transmitted symbols.

3.1.1 Weighting Network for Barker Sidelobes Reduction

The range sidelobes in the WiFi DSSS signal ACF due to the Barker code chipping show a deterministic structure; it is then likely that a simple time-invariant and non-adaptive filter could be sufficient for reducing their level. To this purpose, the use of a weighting network as devised in the past for active radar transmitting Barker coded waveforms can be exploited, as for example in [9]. Obviously the considered weighting network must be optimized for the particular Barker code length exploited by the DSSS-based WiFi transmission as described in the following.

The design of the weighting network for sidelobe reduction of the Barker code (Barker weighting network, BWN) exploits the a-priori knowledge of its ACF. Specifically, for a rectangular chip pulse shape, the 11-chip Barker ACF can be written as:

$$\alpha_B(\tau) = \sum_{k=-5}^{5} a_k \big| T_C - |\tau - k2T_C| \big| \mathrm{rect}_{2T_C}(\tau - k2T_C) \qquad (3.1)$$

where $a_k = -1$ for $k \neq 0$, and $a_0 = 11$. Its samples at time instants

$t_k = nT_C$ can be written as:

$$\alpha_B[n] = \alpha_B(nT_C) = T_C \sum_{k=-5}^{5} a_k \delta(n-2k) = \begin{cases} 0 & n \text{ odd} \\ 11T_C & n = 0 \\ -T_C & n \text{ even} \end{cases} \tag{3.2}$$

Aiming at implementing the BWN as a transversal lattice filter, its impulse response can be written as:

$$h_{BWN}[n] = \sum_{k=-M}^{M} h_k \delta[n-k] \tag{3.3}$$

with total filter length $2M+1$. Thus the output of this weighting network applied to the 11-chip Barker code ACF is given by:

$$\alpha_{BWN}[n] = \alpha_B[n] * h_{BWN}[n] = T_C \sum_{k=-5}^{5} \sum_{m=-M}^{M} \alpha_k h_m \delta[n-(2k+m)] \tag{3.4}$$

The peak value is obtained at index $n = 0$ while the sidelobes region occupies indices $\pm n$ with $n = 1, 2, \ldots, M+10$. Thus the statements of the optimization problem are:

$$\begin{cases} \alpha_{BWN}[0] = T_C \sum_{k=-5}^{5} a_k h_{-2k} = \max \\ \left|\alpha_{BWN}[n]\right| = \left| \sum_{k=-5}^{5} a_k h_{n-2k} \right| \leq T_C \end{cases} \tag{3.5}$$

Each modulus inequality of the system in 3.5 is replaced by two linear inequalities, and the problem is solved using well-known linear programming algorithms. To this purpose, the CVX Matlab-based modeling system for convex optimization ([10]) was exploited.

As an example, Figure 3.1 shows the BWN coefficients obtained for $M = 50$ (filter length $2M+1 = 101$). As is apparent, the filter is symmetrical and has non-zero values only at even indices. It is easy to show that this is a general result whatever is the filter length. As expected, the achieved PSR shows a fairly monotonic decreasing relationship with the filter length. Different values of PSR that can

be achieved using assigned filter lengths are reported in Table 3.1.1. This gives the feeling for the number of filter taps to be selected when trying to optimize for a desired PSR value.

M	Filter Length	PSR (dB)
12	25	26.5
25	51	34
50	101	50
75	151	63

Table 3.1: Peak to Sidelobes Ratio for different BWN lengths.

Notice that there are multiple options for the application of the BWN to the data:

(i) the BWN is applied to each CCF $\chi^{(m)}[l]$ among the surveillance and the reference signal evaluated on a pulse basis, before coherent integration over the train of consecutive pulses;

(ii) the cross-correlation is evaluated between the surveillance signal and a BWN pre-filtered version of the reference signal, before coherent integration over the train of consecutive pulses;

(iii) by operating in the frequency domain, instead of time domain, approaches (i) and (ii) collapse into a scheme where the FFT is evaluated for the BWN (evaluated only once), as well as for the batch corresponding to each single (mth) pulse of both reference and surveillance signals. The three transforms are multiplied together before evaluating the Inverse FFT for the single (mth) pulse. Thereafter, the coherent integration is carried out over the train of consecutive pulses;

(iv) after evaluating the 2D-CCF, the cross-correlation with the BWN is evaluated for each Doppler bin.

Typically, approach (iii) requires a lower computational burden than both (i) and (ii). Approach (iv) can be convenient when the number of Doppler bins is reasonably small. Moreover, it would allow to apply slightly different BWN at the different Doppler frequency, so as

to compensate for the limited degradation induced by the Doppler (easily achievable by modifying the derivation above for the zero Doppler case). This might only be necessary for high Doppler frequencies that are not involved in the typical short range application considered here.

The result of the application of the BWN with total length $2M+1 = 101$ is reported in Figure 3.2 compared to the original ACF for a simulated signal of duration 0.25 s. As expected applying the BWN dramatically decreases the ACF sidelobes due to the Barker code so that a PSR equal to about 50 dB is obtained within time delays of 0.8 μs. Notice that the filter weights evaluation has to be performed only once, following the evaluation of the filter length required by the specific surveillance application. However, the conceived weighting network is ineffective against the periodic sidelobe structure due to the non-zero correlation among consecutive symbols of the Beacon frame. A proper strategy to counteract this effect is presented in the next sub-section.

3.1.2 Additional Side-lobes Reduction Filter (ASRF)

Aiming at the detection of targets at delays higher than 0.8 μs (ranges higher than 120 m), the temporal ACF sidelobes at multiples of 1 μs should be reduced to avoid masking effects on targets appearing at those delays. Notice that, while the positions of these additional peaks in the ACF are a-priori known, their value is data dependent and has to be estimated from the collected data. To this purpose the reference signal can be used to evaluate the actual signal ACF at delays $t_k = kT_{SYM}$ ($\hat{\alpha}(t_k)$); these estimates can be then exploited to design an effective sidelobe reduction filter. Specifically, the required reduction of these sidelobes can be obtained by subtracting from the original CCF $\chi^{(m)}(\tau)$ for the mth pulse, properly

scaled and delayed replicas, namely:

$$\chi^{(m)}_{ASRF} = \chi^{(m)}(\tau) - \sum_{k=-K}^{K} \sum_{k\neq 0} \gamma^{(m)}_k \chi^{(m)}(\tau - kT_{SYM}) \tag{3.6}$$

where K is the number of range sidelobes to be removed on both sides of the ACF main peak and $\gamma^{(m)}_k$ is the scaling factor for the kth sidelobe at the mth pulse and is given by:

$$\gamma^{(m)}_k = \frac{\hat{\alpha}^{(m)}(kT_{SYM})}{\hat{\alpha}^{(m)}(0)} \tag{3.7}$$

Thus the transfer function of this additional sidelobes reduction filter (ASRF) is given by:

$$H^{(m)}_{ASRF}(f) = 1 - \sum_{k=-K}^{K} \sum_{k\neq 0} \gamma^{(m)}_k \mathrm{e}^{-\iota 2\pi f k T_{SYM}} \tag{3.8}$$

The number K of sidelobes to be reduced can be arbitrarily selected aiming at removing periodical sidelobes contribution over a given range extent corresponding to the surveillance area. Notice that the ASRF can be applied after the BWN by properly modifying the scaling factors, namely the samples of the BWN-filtered reference signal ACF should be used. As an example the ACF resulting from the cascade of the two different sidelobe reduction filters is shown in Figure 3.2 when the ASRF operates with $K = 3$. Notice that the joint application of the two considered approaches in the range dimension provides a significant improvement of the PSR (a PSR of about 50 dB is obtained for ranges smaller than 630 m) and the effective removal of the isolated peaks with only a very limited loss in SNR which is mainly due to the BWN.

As a final remark, it is to be noticed that the proposed techniques have been designed to cope with the limiting range sidelobes level of the DSSS pulses AF; however they can be effectively applied

even when mixed transmissions are exploited containing also HR-DSSS and OFDM pulses. In fact, as previously described, both the BWN and the ASRF can be applied on a pulse basis. Moreover, the particular modulation adopted for each pulse within a given signal fragment can be easily identified through a rough demodulation. Thus, pulses exploiting the DSSS PHY can be separately processed using the proposed techniques for sidelobes reduction while standard weighting networks can be applied to HR-DSSS or OFDM modulated pulses. In addition a guard interval blanking might be applied in the latter case.

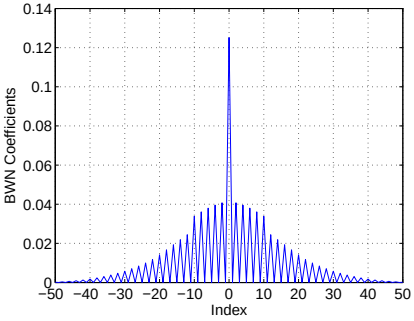

Figure 3.1: Barker Weighting Network coefficients for $M = 50$.

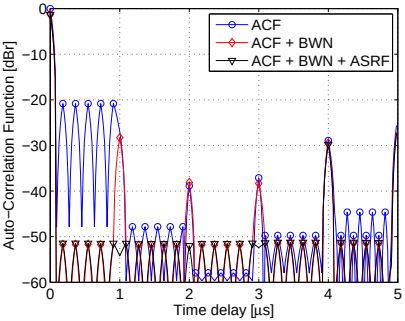

Figure 3.2: Auto-Correlation Function with sidelobes control filters for a DSSS signal of duration 0.25 s.

3.2 PRS control along the Doppler frequency dimension

The Doppler response $C_0^{(w)}[p]$ of a WiFi signal matched filter coincides with the zero delay cut of the AF in Equation 2.2:

$$C_0^{(w)}[p] = C^{(w)}[0,p] = \left| \sum_{m=0}^{M-1} \mathrm{e}^{-\iota 2\pi \frac{pi_m}{N_{int}}} \chi^{(m)}[0] w[i_m] \right|^2 \tag{3.9}$$

where $w[i_m]$ is the i_mth weight of the adopted Doppler sidelobes control network properly resampled at given time instant indices i_m corresponding to the transmission of consecutive WiFi pulses and $\chi^{(m)}[0]$ is the energy of the mth pulse.

Notice that Equation 3.9 yields the typical digital 'sinc' shape for constant energy pulses transmitted at equally spaced time instants when a uniform tapering function is adopted. However, when a WiFi signal is exploited these conditions are not met since, as previously mentioned, a WiFi-based PBR operates with randomly-varying PRT and variable energy per pulse depending on its duration. Thus, the Doppler response in Equation 3.9 is usually characterized by high sidelobes structures which might strongly limit the detection capability of the resulting PBR.

This is shown in the following with reference to typical WiFi transmissions simulated according to the IEEE 802.11g Standard. The signal simulator developed in MATLAB®allows different data rates and packet sizes and accounts for silent periods according to the CSMA approach. In the following a simulated WiFi signal fragment of 0.5 s consisting of consecutive DSSS or OFDM pulses with a minimum nominal separation equal to 2 ms (equivalent PRT) is considered. This would allow a maximum observable non-ambiguous Doppler extent of 500 Hz. At the typical WiFi wavelength of about 12 cm, such a value corresponds to about 216 km/h of bistatic velocity, which might be sufficient for a short range surveillance application (e.g. when interested in monitoring vehicular or human targets).

However, the actual PRT measured over the train of generated pulses is highly variable. This is shown in Figure 3.3 which reports the temporal separations between consecutive pulses contained in the 0.5 sec fragment of the simulated WiFi signal. As is apparent, the temporal separation between consecutive pulses is always higher than 2 ms and reaches 5.5 ms in the worst case. The mean value of the obtained PRT is 2.56 ms with a standard deviation of 0.59 ms.

The zero-delay cut ($l = 0$) of the obtained AF is reported in Figure 3.4 for a uniform tapering window. Notice that the non-weighted Doppler response is well far from the theoretical digital 'sinc' shape obtained in [7] showing sidelobes which do not decay as 6 dB/octave. Moreover, strong ambiguities appear at bistatic Doppler frequencies corresponding to ± 140 Hz, ± 160 Hz and ± 210 Hz. Similarly, after the application of the Hamming weighting network (see Figure 3.5), the obtained PSR is well below the 43 dB guaranteed in the theoretical case. In fact a conventional amplitude weighting network, such as the Hamming one, is designed to reduce the sidelobes arising from the sharp onset and cut-off of the signal temporal windowing. Thus it is ineffective against the severe Doppler ambiguities due to long silence periods of the AP.

Such sidelobes structure might be responsible of useful dynamic range reduction or masking effects over weak targets, thus limiting the WiFi-based PBR detection capabilities. A proper strategy to counteract this effect is presented here.

The proposed technique for the design of an effective weighting network exploits the actual shape of the Doppler response in Equation 3.9 which can be directly evaluated based on the knowledge of the temporal durations and separations of consecutive pulses in the CIT. Thus the set of tapering window weights is optimized aiming at controlling the Doppler response at least within the useful Doppler frequency extent.

Specifically, the proposed method starts from the selection of a conventional network $w_r[i_m]$ which is used as a reference in the constrained optimization problem. Let Δp_r be the Doppler frequency interval containing the main lobe of the Doppler response there in-

cluding the resolution degradation δr due to the application of the reference tapering window:

$$\Delta p_r := [-0.5\delta r, \quad +0.5\delta r] \tag{3.10}$$

Moreover let Δp_u be the desired useful Doppler area (e.g. that given by the theoretical expected ambiguities). The weights $w_{\text{ODWN}}[i_m]$ of the optimized Doppler weighting network (ODWN) are computed by solving a constrained optimization problem which is based on two main statements:

- The Doppler response in the Δp_r interval is constrained to match the Doppler response that would be obtained after the application of the reference tapering window for constant energy, equally spaced transmitted pulses:

$$\left| \sum_{m=0}^{M-1} \mathrm{e}^{-\iota 2\pi \frac{p i_m}{N_{int}}} \chi^{(m)}[0] w_{\text{ODWN}}[i_m] \right|^2 = C_{0,\text{theo}}^{(w_r)}[p] \quad \text{for } p \in \Delta p_r \tag{3.11}$$

- The Doppler response in the remaining Doppler extent (the sidelobes area) should be as low as possible:

$$\left| \sum_{m=0}^{M-1} \mathrm{e}^{-\iota 2\pi \frac{p i_m}{N_{int}}} \chi^{(m)}[0] w_{\text{ODWN}}[i_m] \right|^2 = \min \quad \text{for} \begin{cases} p \notin \Delta p_r \\ p \in \Delta p_u \end{cases} \tag{3.12}$$

The optimization problem is solved using well-known linear programming algorithms (e.g. CVX for MatLab [10]).

Figure 3.5 reports the zero-delay cut of the AF obtained using the resulting ODWN (black-dotted curve) for the same simulated signal considered in Figure 3.4. The result obtained with a conventional Hamming window (which was used as reference window, with $\delta r = 1.5$) is also reported for comparison (red-dashed curve). As expected, the AF shape within the main Doppler lobe is identical in the two

cases. In contrast, the proposed weighting network allows to strongly reduce the severe Doppler ambiguities at bistatic velocities of ±140 Hz, ±160 Hz and ±210 Hz yielding a quite flat sidelobes level with a PSR better than 30 dB. Notice that, due to the long silence periods present in the considered data (see Figure 3.3), the obtained PSR is not extremely high; however it is significantly higher (about 10 dB) than that obtained with the conventional Hamming window.

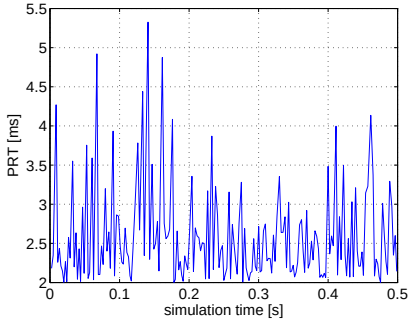

Figure 3.3: Temporal separation between consecutive pulses in a 0.5 s. simulated signal fragment.

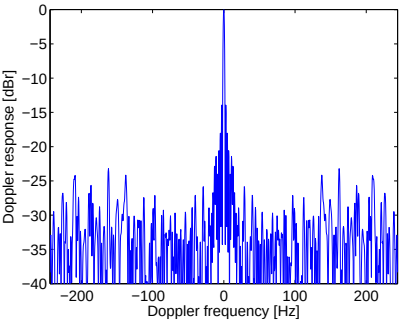

Figure 3.4: Original Doppler response.

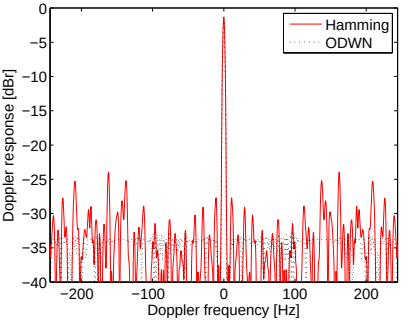

Figure 3.5: Doppler response with tapering functions.

3.3 Overall processing scheme

Figure 3.6 reports the resulting processing scheme for PSR control in WiFi-based PBR. In particular, the approximation of Equation 2.2 is exploited to simply and effectively process WiFi transmissions. Specifically, with reference to the range sidelobes control techniques, it has been shown that they can be applied on a pulse basis by properly filtering the reference signal. Moreover, the particular modulation adopted for each pulse within a given signal fragment can be easily identified through a rough demodulation. Thus, pulses exploiting different modulations can be separately processed using the appropriate technique for sidelobes reduction (weighing networks presented in Section 3.1 for DSSS pulses, standard Hamming network + guard interval blanking for OFDM pulses). Moreover, after pulse detection, a timestamp is stored to evaluate the optimized Doppler weighting network over the considered CPI. Finally, the two-dimensional range/velocity map is evaluated through a Fourier Transform operation.

The effectiveness of the proposed processing scheme is demonstrated against real data in Chapter 4.

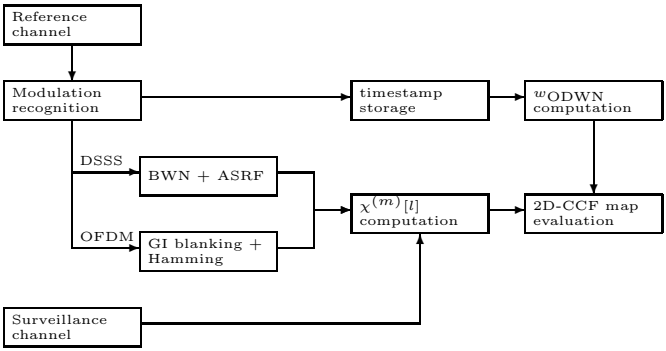

Figure 3.6: Scheme of processing for WiFi signals AF control.

Chapter 4

Acquisition campaign of year 2009

This Capther reports experimental results obtained against real data collected during the first acquisition campaign (year 2009). Particularly, Section 4.1 discusses the experimental setup built up at DIET Dept - University of Rome "La Sapienza", Section 4.2 reports the results of the application of the WiFi-based passive radar processing for AF control to real data and, finally, Section 4.3 reports the results of different target detection experiments performed with both vehicular and human targets.

4.1 Experimental setup

The adopted experimental setup is sketched in Figure 4.1. A portable wireless AP (D-Link DAP 1160) is connected to the transmitting (Tx) antenna while a -20 dB fraction of the transmitted signal is gathered by a dedicated receiving channel (reference channel) by using a directional coupler which yields a 0.5 dB insertion loss and isolation greater than 20 dB. The second channel of a dual-

channel receiving system is directly connected to a separate receiving (Rx) antenna which was used to collect the surveillance signal back-scattered by targets and obstacles. The antennas are characterized by a beamwidth of about 15° and a front to back ratio greater than 30 dB. The wireless AP was configured to transmit in channel 7 of the WiFi band (centre frequency of 2.442 GHz).

The receiving system uses a single fully coherent down conversion stage (a set of two National Instrument NI-5600 devices) for the two channels, so as to move the central frequency of the selected WiFi channel to an intermediate frequency of 15 MHz. After adequate filtering and amplification, the signal is sampled at 55 MHz using a high quality dual channel A/D converter (National Instrument NI-5122 device) with a wide dynamic range (software selectable), controlled by an external stable and tunable oscillator. The acquired IF data was stored and processed off-line using digital filters for transmitted pulses automatic detection, digital down-conversion (DDC), and pulse modulation identification through rough demodulation.

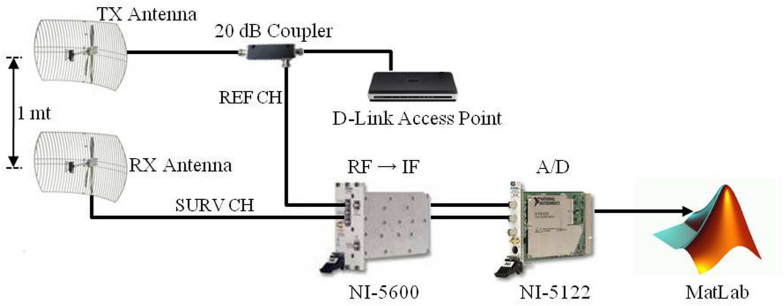

Figure 4.1: Sketch of the experimental setup

4.2 AF analysis for real WiFi transmissions

Firstly, the signal collected at the reference channel has been used to evaluate the AF of the considered signal of opportunity and to test the proposed sidelobes reducing techniques.

4.2.1 Time delay dimension

Figure 4.2(a) shows the reference signal ACF with and without the sidelobes control filters. In particular, a 0.5 s signal fragment has been considered containing only DSSS PHY-based pulses. The sidelobes reducing networks operate with the same parameters considered in the simulated analysis of Figure 2.1(c). As expected, the original ACF shows the typical structure of the Barker sidelobes with only small deviations with respect to its theoretical version. These are due to the AP and the receiving channel filters that reduce the actual signal bandwidth with respect to its nominal value. As a direct consequence of these deviations, the BWN is not able to obtain the theoretical peak to sidelobes ratio of 50 dB. However, notice that a PSR greater than 35 dB is obtained which results in a significant increase of the useful dynamic range. Finally, notice that the ASRF operating with $K = 3$ is able to strongly reduce the first 3 lobes due to the correlation among the symbols of the DSSS frame.

Similarly Figure 4.2(b) reports the reference signal ACF for a 0.5 s signal fragment corresponding to a typical mixed transmission consisting of 358 frames which were recognized to be either DSSS or OFDM pulses. Specifically, 208 DSSS pulses have been identified with durations between 199 μs and 830 μs; the remaining 150 OFDM pulses are characterized by smaller durations (between 24 μs and 344 μs). This is a quite common situation since the DSSS modulation is the most commonly used; moreover, based on the higher data payload capability of the OFDM PHY, usually shorter pulses are

transmitted.

As it is apparent, the ACF corresponding to the considered mixed transmission is dominated by the AF of the DSSS PHY-based pulses, resulting in a PSR slightly higher than 20 dB. Nevertheless, an additional peak appears at 3.2 μs due to the guard interval insertion in the OFDM symbols. In this case, pulses exploiting different modulations are separately processed by applying the required range sidelobes control strategies (BWN+ASRF for DSSS pulses, standard Hamming network+guard interval blanking for OFDM pulses) according to the processing scheme of Figure 3.6. The corresponding result is reported in Figure 4.2(b) for comparison (black curve). As is apparent, a PSR higher than 35 dB is obtained by both reducing the sidelobes level of the DSSS pulses and the undesired structures in the OFDM signals AF.

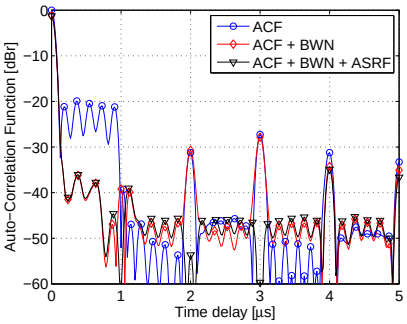

(a)

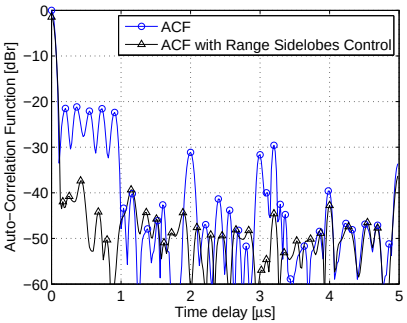

(b)

Figure 4.2: Reference signal ACF with and without sidelobes control filters: (a) for a DSSS PHY-based transmission; (b) for a mixed transmission.

4.2.2 Doppler frequency dimension

Figure 4.3 reports the temporal separations of the transmitted pulses contained in 0.5 s of the acquired data. As is apparent, the actual PRT measured over the train of consecutive pulses is highly variable. In particular, the temporal separation between consecutive pulses is usually higher than 1 ms (the nominal Beacon repetition interval) and reaches 13 ms in the worst case. The mean value of the obtained PRT is 2.31 ms with a standard deviation of 1.77 ms.

The obtained Doppler response (Equation 3.9) is reported in 4.4. As is apparent, the randomly varying PRT reported in Figure 4.3 gives rise to a strong ambiguity corresponding to a Doppler frequency of ± 137 Hz with a PSR of 12 dB. As discussed in Section 3.2 against simulated date, such strong ambiguities cannot be counteracted by resorting to conventional weighting networks, since those are designed to reduce the sidelobes arising from the sharp onset and cut-off of the signal temporal windowing. As an example, the Doppler response after the application of a conventional Hamming window (see the red-dashed line in Figure 4.5) still shows the undesired ambiguities sturcture.

On the brightside, after solving the optimization problem proposed in Section 3.2, the computed weights of the ODWN can be applied in Equation 3.9 thus obtaining the black-dotted curve reported in the same Figure 4.5. The resulting PSR is still well far from the theoretical 43 dB that would be obtained with the reference Hamming window. However the strong ambiguities at ± 137 Hz have been strongly reduced and a significant PSR improvement of 12 dB is obtained with respect to the standard Hamming window.

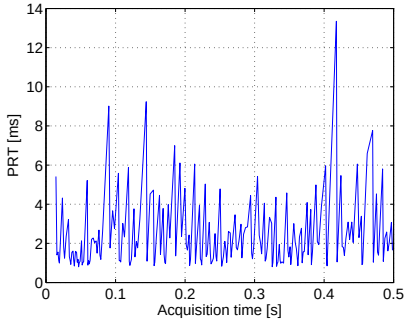

Figure 4.3: Temporal separation between consecutive pulses in a 0.5 s. collected signal fragment.

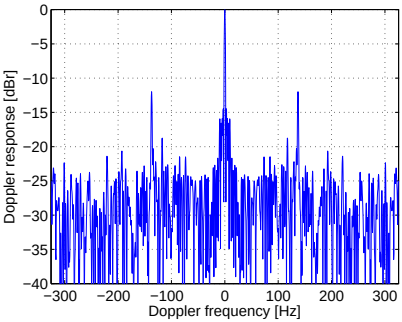

Figure 4.4: Original Doppler response.

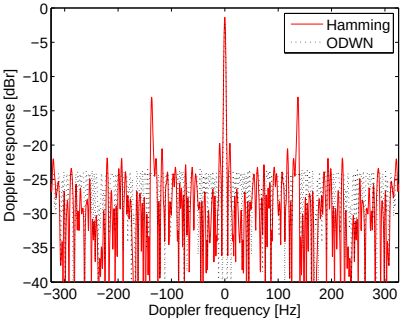

Figure 4.5: Doppler response with tapering functions.

The reported results clearly show the effectiveness of the proposed techniques against real data. In the following sub-section their benefits will be demonstrated with reference to the target detection issue.

4.3 Targets detection experiments

The target detection performance of the WiFi-based PBR system has been evaluated with reference to the test configurations sketched in Figure 4.6. These tests were performed in an outdoor environment (a parking area in Cisterna di Latina, Italy) using vehicular and human targets.

The AP was set up to roam for connected devices emitting the beacon signal at 1 ms intervals. A quasi-monostatic configuration was adopted for the two antennas which were mounted one on top of the other (1 m apart as sketched in Figure 4.1, being the Rx antenna at about 3 m above the ground).

In experiment A, a single target was present consisting of a car moving toward the antenna with about 21 km/h of velocity, as sketched in Figure 4.6(a). Experiment B was performed again with a single vehicular target but in a different cluttered scenario. In fact, as depicted in Figure 4.6(b), the antennas are now steered toward the metallic wire fence delimiting the parking area, thus a stronger reflection is expected at about 144 m of range with respect to the previous case. Finally, in experiment C, two targets were present (a car and a running man) moving forward the antenna location at approximately 25 km/h and 20 km/h, respectively, as sketched in Figure 4.6(c).

In all the cases the antennas were pointed so that the considered targets were included in the main beam.

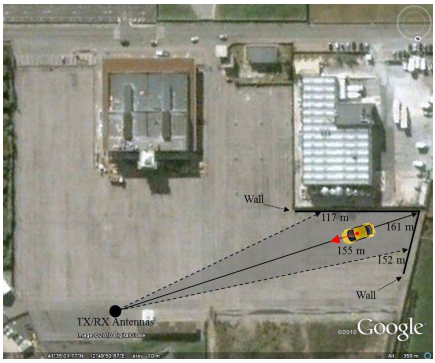

(a) Experiment A

(b) Experiment B

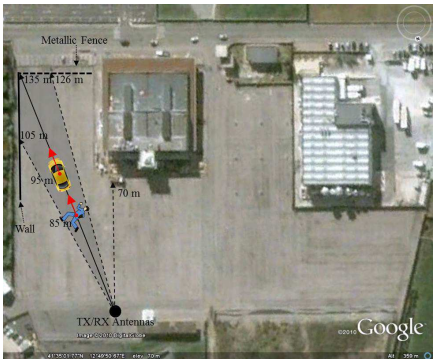

(c) Experiment C

Figure 4.6: WiFi-based PBR experiments in Cisterna di Latina (Rome).

4.3.1 Experiment A

The results obtained for experiment A are reported in Figures 4.7. Figure 4.7(a) shows the 2D-CCF evaluated without sidelobe control over an integration time of 1 s, which allows a velocity resolution equal to 0.22 km/h. The 2D-CCF has been normalized to the nominal thermal noise power level so that the value at each map location represents the estimated SNR. Moreover the reported map has been upper saturated to a value of 50 dB so that the same colour scale is used for all the reported results for a fair direct comparison.

As is apparent, a strong peak appears at zero range and zero velocity corresponding to the direct signal transmitted by the transmitting antenna and collected by the sidelobes of the receiving antenna. Moreover all the 2D-CCF cut at zero velocity is characterized by very high SNR values (well above the limiting color scale value of 50 dB) due both to the range sidelobes related to the direct signal contribution and to the reflections of the transmitted signal from stationary scatterers. Each peak at zero velocity comes with the corresponding Doppler sidelobe structure providing a high general sidelobe level all over the 2D-CCF that completely masks the target return.

Figure 4.7(b) shows the 2D-CCF evaluated using a mismatched reference signal (based on the sidelobes control techniques presented in Chapter 3) to achieve the desired PSR both along the range and the velocity dimensions. It has to be noted that in this specific case, the sidelobes control techniques are essential to detect the target, which appears at a range strongly affected by the sidelobe corresponding to the subsequent symbol correlation (about 150 m). This clearly shows the effectiveness of the schemes proposed in Section 3.6 to control the AF sidelobes.

It has also to be noted that, despite the direct signal and the stationary clutter contributions are clearly present in the Range-Velocity map, especially at zero Doppler, their presence does not affect the ability to detect the target.

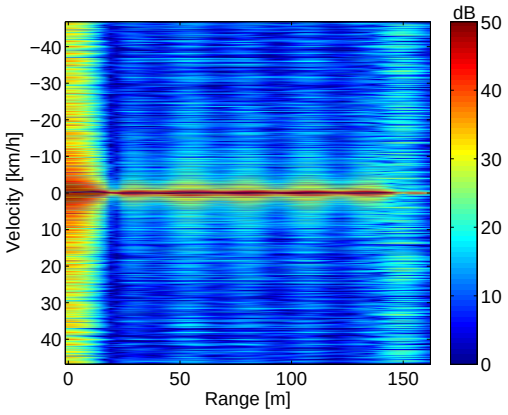

(a)

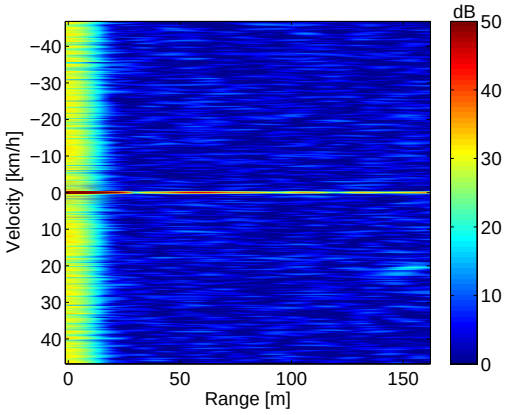

(b)

Figure 4.7: Range/velocity maps for Experiment A: (a) original 2D-CCF, (b) 2D-CCF with sidelobes control.

4.3.2 Experiment B

The range/velocity maps obtained for Experiment B without and with sidelobes control, are reported in Figures 4.8. In this case an integration time of 0.5 sec is used, which allows a velocity resolution equal to 0.44 km/h. All the reported maps have been normalized with the same criterion used for Figures 4.7.

The CPI exploited to evaluate the range/velocity maps for Experiment B is the same of that considered in Chapter 3 to validate the performance of both the range sidelobes techniques and the optimized Doppler weighting network against real data.

With reference to the original 2D-CCF reported in Figure 4.8(a), strong peaks appear at zero velocity which correspond to the direct signal from the transmitter received by the sidelobes of the surveillance antenna (peak at zero range) and to the echo from the metallic wire fence (peak at 145 m). Moreover an additional peak is also visible at a range-velocity location (30 m, -8 m/s) which is likely to correspond the vehicular target moving in the parking area.

The unremoved Doppler ambiguities observed in Doppler response of Figure 3.4 yield isolated peaks in the original range-velocity map (Figure 4.8(a)) corresponding to ambiguities of clutter returns (115 m and 145 m at $\pm$28.8 km/h) or ambiguities of the target (30 m at -61.2 km/h). Such isolated peaks might seriously affect the WiFi-based PBR detection performance by causing false alarms or masking weak targets.

When the proposed weighting networks are applied (see Figure 4.8(b)), all the peaks corresponding to the Doppler ambiguities are strongly reduced which results in a significant improvement in terms of useful dynamic range. At this stage, the target can be easily detected after the application of typical Constant False Alarm Rate (CFAR) autogate for radar detection. Is has to be noted that also in this case, target detection is possible despite the presence of stronger contributions at zero-velocity location (stationary scatters).

While often the target detection is easily achieved after only a sidelobe reduction application, there are situations where this is not

the case. This largely depends on:

i Target motion characteristics, that can place the target echo in a position of the Range-velocity map, where it is masked by the Doppler sidelobes of stationary returns,

ii Presence of strong obstacles at specific ranges that produce strong sidelobes in the frequency domain thus increasing the probability to mask targets.

This case will be discussed in the next sub-section with the results of Experiment C.

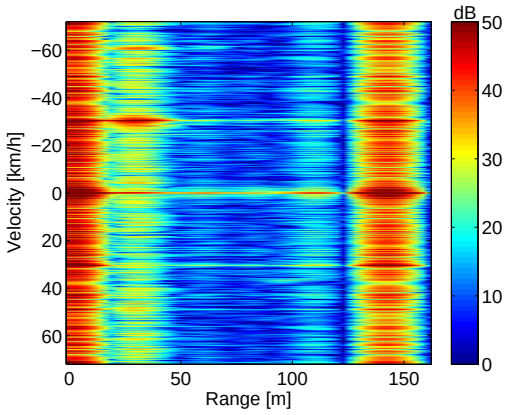

(a)

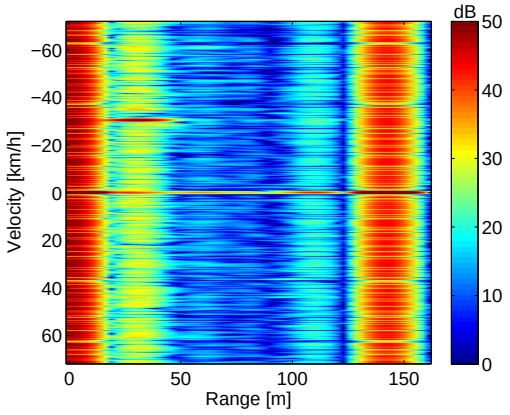

(b)

Figure 4.8: Range/velocity maps for Experiment B: (a) original 2D-CCF, (b) 2D-CCF with sidelobes control.

4.3.3 Experiment C

The results of experiment C are reported in Figures 4.9.

Figure 4.8(a) shows the 2D-CCF evaluated without sidelobe control. As is apparent, there are a large number of strong contributions at zero velocity that come with their severe sidelobe structure (spreading along the velocity axis) and clearly mask all target echoes.

Figure 4.8(b) shows the 2D-CCF evaluated using the proposed sidelobes reduction techniques in both the range and the Doppler frequency (velocity) dimensions. It has to be noted that in this specific case the application of the ASRF is not strictly necessary since the maximum range searched for detection is limited by the border network which acts as an electromagnetic shield.

Also in this case, both the range and the Doppler frequency sidelobes related due to the direct signal and other multipath contributions have been significantly reduced. As a consequence, isolated peaks now appear at zero velocity at ranges of about 70 m, 100 m and 135 m which are now clearly recognized to be the reflections of the transmitted signal over the walls, the buildings and the metallic wire fence delimiting the parking area (see Figure 4.6(c)). By measuring the corresponding peak level after integration and taking into account the gain of the receiving chain, it is possible to estimate the likely magnitude of these contributions at the antenna output. Specifically, a -59 dBm power level is obtained for the DSI contribution received by the sidelobes of the Rx antenna; the multipath contributions due to the reflections from obstacles at 70 m, 100 m and 135 m appear respectively at about -28 dB, -21 dB, and -10 dB with respect to the DSI power level. The two targets returns can be identified among the residual sidelobes structures and by applying a local threshold the two moving targets are certainly detected. This once again shows the effectiveness of the schemes proposed in Chapter 3 to control the AF sidelobes.

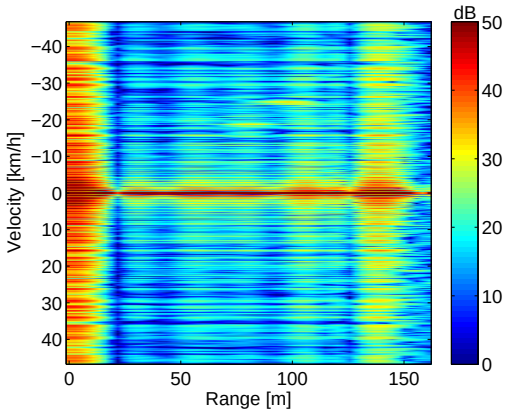

(a)

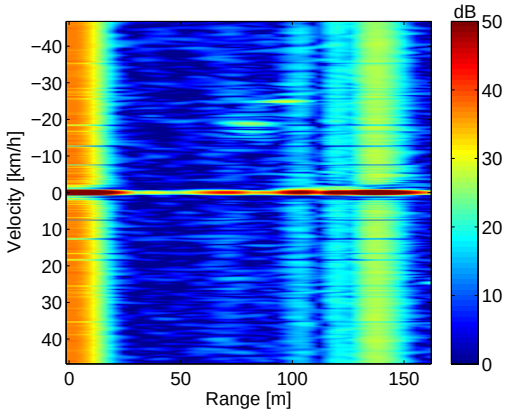

(b)

Figure 4.9: Range/velocity maps for Experiment C: (a) original 2D-CCF, (b) 2D-CCF with sidelobes control.

The experimental results previously discussed, preliminarily show the potentialities of the WiFi-based PBR for detection of both human and vehicular targets in outdoor environments. However, while the targets are detected, it is apparent that their detection is still limited by the small dynamic range available, since many returns, especially at zero Doppler frequency locations, are present in the map. To give the feel of the target detection capabilities at this stage, the estimated target power level at the antenna output for Experiment C is equal to -102 dBm for the vehicular target and -106 dBm for the human target which are well below the power levels of the DSI and multipath contributions.

This clearly shows that a further processing stage to remove the disturbance contribution, has to be investigated since it can provide an additional advantage at the cost of a higher computation load.

Chapter 5

Disturbance removal stage

The experimental results reported in Chapter 4 clearly show the potentialities of the WiFi-based PBR system in target detection. In particular, the effectiveness of the proposed AF control scheme has been demonstrated against real data in different target detection tests. However, aiming at increasing the useful dynamic range - limited by the strong stationary contributions - proper techniques should be implemented to remove the undesired returns in the surveillance signal (direct signal breakthrough and multipath reflections). To this purpose, a modified version of the adaptive cancellation approach presented in [11], the Extensive Cancellation Algorithm (ECA), is presented in Section 5.1 while the results of its application against the same experiments discussed in Chapter 4 are shown in Section 5.2. Moreover, in Section 5.3 the benefits of the proposed cancellation scheme are shown with reference to a human target detection experiment performed in an indoor scenario. Finally, Section 5.4 reports the overall WiFi-based PBR processing scheme for target detection which includes the stages of both sidelobes control and

cancellation.

5.1 The Extensive Cancellation Algorithm

The Extensive Cancellation Algorithm (ECA) operates by subtracting from the surveillance signal properly scaled and delayed replicas of the reference signal. Specifically assuming that the multipath and clutter echoes are potentially backscattered from the first K range bins, the output of the ECA is evaluated as:

$$\mathbf{s}_{\text{ECA}} = \mathbf{s}_{\text{surv}} - \mathbf{S}_{\text{ref}}\alpha \tag{5.1}$$

where

- $\mathbf{s}_{\text{surv}} = \left[s_{\text{surv}}[0], s_{\text{surv}}[1], s_{\text{surv}}[2], \ldots, s_{\text{surv}}[N-1]\right]^T$ is a $N \times 1$ vector containing the samples $s_{\text{surv}}[i]$ collected at the surveillance receiving channel at time instants $t_i = i/f_s$, $i = 0, \ldots, N-1$;
- $\mathbf{S}_{\text{ref}}$ is a $N \times K$ matrix whose columns are the delayed versions of the reference signal and define a basis for a K-dimensional disturbance subspace;
- α is a $K \times 1$ vector containing the adaptive filter weights which are evaluated by resorting to a Least Square (LS) approach which minimizes the power of the signal at the output of the filter:

$$\min_{\alpha} \left\{ \|\mathbf{s}_{\text{ECA}}\|^2 \right\} \Rightarrow \alpha = \left(\mathbf{S}_{\text{ref}}^H \mathbf{S}_{\text{ref}}\right)^{-1} \mathbf{S}_{\text{ref}}^H \mathbf{s}_{\text{surv}} \tag{5.2}$$

As is apparent, in its original version, the ECA requires the filter weights to be estimated by averaging over the whole temporal extension over which integration is performed ($T_{int} = N/f_s$).

For the considered application, the Batches version of the ECA (ECA-B) is adopted which requires the filter weights to be estimated over smaller portions of the integration time; specifically the output

of the ECA-B is given by the concatenation of the output vectors $\overline{\mathbf{s}}_{\mathrm{ECA,i}}$ $(i = 1, \ldots, b)$ obtained by applying the ECA over b consecutive input vectors of reduced dimension $N_B = N/b$:

$$\mathbf{s}_{\text{ECA-B}} = \begin{bmatrix} \overline{\mathbf{s}}^T_{\mathrm{ECA},0} & \overline{\mathbf{s}}^T_{\mathrm{ECA},1} & \cdots & \overline{\mathbf{s}}^T_{\mathrm{ECA,b\text{-}1}} \end{bmatrix}^T \tag{5.3}$$

where

$$\overline{\mathbf{s}}_{\mathrm{ECA,i}} = \overline{\mathbf{s}}_{\mathrm{surv,i}} - \overline{\mathbf{S}}_{\mathrm{ref,i}} \overline{\alpha}_{\mathrm{i}} \quad (N_B \times 1) \tag{5.4}$$

and the ith filter weights evaluation is repeated at each batch.

Reducing the temporal dimension of the single batch within certain limits does yield significant adaptivity loss when operating in a stationary environment. However, it was demonstrated in [11] to make the system more robust to the slowly varying characteristics of the environment which appears to be an appreciable advantage in the considered application, especially in outdoor scenarios.

Obviously, the batch duration affects the width of the filter cancellation notch in the Doppler dimension, so that it should be traded with the minimum target detectable velocity to be guaranteed. As an example Figure 5.1 reports the expected SNR gain as a function of the target bistatic velocity for different values of the batch duration ($T_B = N_B/f_s$). The SNR gain has been normalized to the maximum theoretical SNR gain resulting from the integration over the whole integration time.

Specifically, to obtain this figure, the data set acquired in the experimental tests discussed in Chapter 4 was exploited. This data set is representative for a typical cluttered outdoor scenario. A fictitious target echo has been injected into the available data, generated as a delayed and Doppler shifted replica of the reference signal with known input power. Then the ECA-B filter has been applied using different batch durations and the output target power has been evaluated by integrating over $T_{int} = 0.5$ s. Finally the ratio has been computed between the measured target output power and the expected maximum output power after integration. By varying the Doppler frequency of the injected target and averaging the results

over different data files, it has been possible to estimate the expected Doppler response of the proposed cancellation filter in a real scenario.

As it is expected, the application of the cancellation filter yields a corresponding SNR loss for slow moving targets. Specifically, the minimum target detectable velocity (i.e. the velocity yielding a SNR loss of 3 dB) decreases as the batch duration T_B increases.

The performed analysis allows to select batch durations between 30 and 60 ms which were theoretically and experimentally verified to yield a good trade-off between cancellation performance and slow target detection capability. This certainly applies to outdoor applications, involving slow moving vehicles (cars and motorbikes), as well as running or fast moving people, that show bistatic velocities typically outside the notch of the cancellation filter based on these batch sizes.

Slightly longer batch durations might be exploited when interested at the detection of slowly moving people in indoor scenarios; in particular, the performed analysis showed that batch durations between 60 and 120 ms yield remarkable cancellation performance against the very slowly varying characteristics of the environment while significantly reducing the minimum detectable velocity.

The results obtained with the proposed processing schemes against the same experiments discussed in Chapter 4 are reported in the following section.

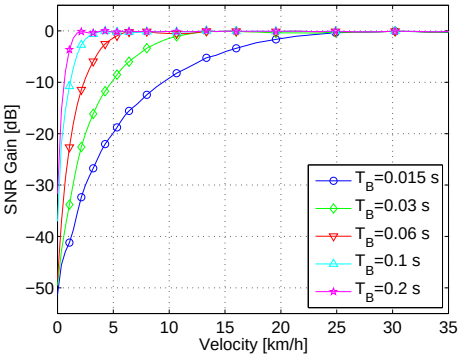

Figure 5.1: SNR gain vs. target bistatic velocity for different values of the cancellation filter batch duration.

5.2 Experimental results

Figures 5.2 reports the range/velocity maps evaluated after sidelobes control and disturbance cancellation fro Experiments A, B and C discussed in Chapter 4.

In all the cases, the cancellation filter (ECA-B) operates over consecutive batches of duration 50 ms. Moreover, the filter length was set to remove reference signal replicas with delays corresponding to ranges between 0 and 330 m (K=121). As is apparent from Figures 5.2, the direct signal and all the disturbance contributions at zero Doppler are effectively removed thus providing a cleaner overall map.

However, in the cases of Experiments A and B (Figures 5.2(a) and 5.2(b), respectively), the additional use of the cancellation technique does not further improve the target detection capability, since in both the cases the target could be detected even after only the application of the sidelobes control stage (Section 4.3).

In contrast, in the case of experiment C (Figures 5.2(c)), the effective removal of the direct signal and all the disturbance contributions at zero Doppler significantly increases the useful dynamic range for target detection. Both the car (range: 95 m, velocity: at -25 km/h) and the human target (range: 85 m, velocity: -20 km/h) now appear as strong peaks in the map, so that they can be easily detected without ambiguities. This clearly shows the significant benefit deriving from the joint application of disturbance cancellation techniques and AF control filters despite the small SNR loss to be accepted.

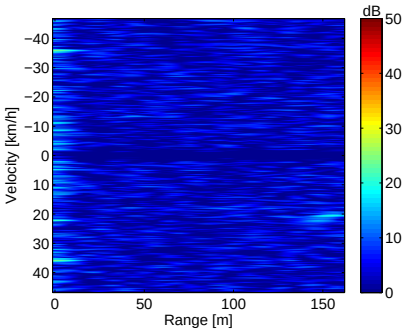

(a) Experiment A

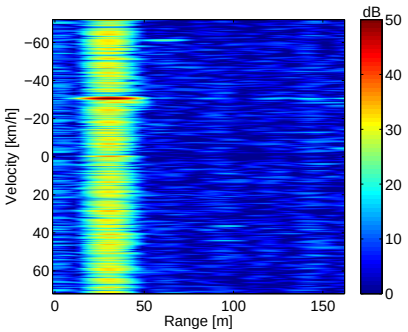

(b) Experiment B

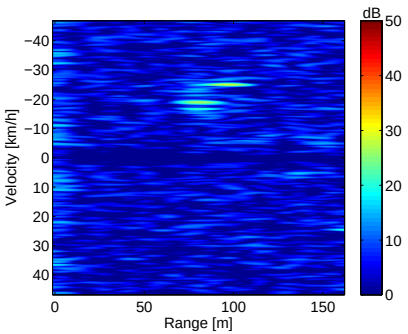

(c) Experiment C

Figure 5.2: Rnage/velocity maps obtained after sidelobes control and disturbance cancellation

5.3 Experimental results for indoor scenario

To further demonstrate the benefits of the cancellation technique, the results obtained for a highly cluttered indoor environment (depicted in Figure 5.3(a)) are reported in Figures 5.3(b) and 5.3(c) for an integration time equal to 0.15 s.

As is apparent, after the application of the sidelobes control techniques (see Figure 5.3(b)), the target (a person walking toward the Tx/Rx antennas) cannot be detected against the high DSI and multipath contributions. In fact, in this case, an even more severe scenario is experienced in terms of disturbance power level. Specifically, since the same antennas configuration was adopted, the power level of the DSI contribution is similar to that measured in the outdoor scenario. However, in this case, the signal reflections on the rooms walls, possibly received by the Rx antenna main beam, give rise to significantly higher multipath contributions (even higher than the DSI component). Notice that the highest peak at zero Doppler appears at a range comparable to the rooms dimensions and the corresponding estimated power level is 2 dB higher than the DSI contribution (approximately -57 dBm at the antenna output).

Moreover, additional peaks are present at further ranges due to the multiple signal bounces against the rooms walls (the first additional peak being at -7 dB with respect to the highest peak at zero Doppler frequency). Nevertheless, such disturbance contributions are effectively removed after the application of the ECA-B cancellation filter operating with a batch duration equal to 0.1 s. This is clearly apparent from the map reported in Figure 5.3 where all the contributions at zero Doppler frequency locations have been cancelled together with their sidelobe structures and the human target (with estimated power level 28 dB below the strongest multipath contribution) appears as an isolated peak (range: 15 m, velocity: 3 km/h), so that it can be easily identified and detected.

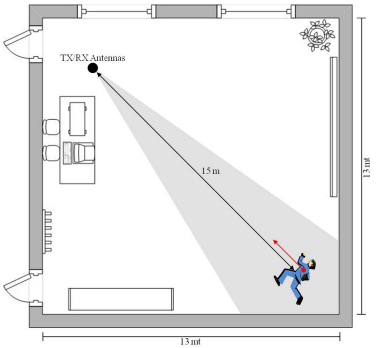

(a) Scenario

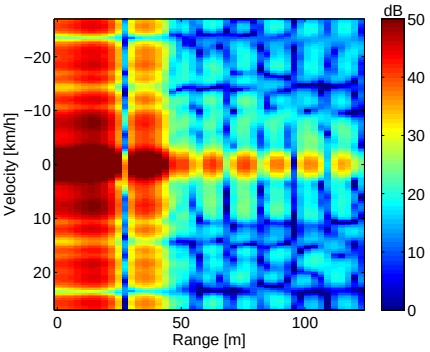

(b) 2D-CCF + AF control

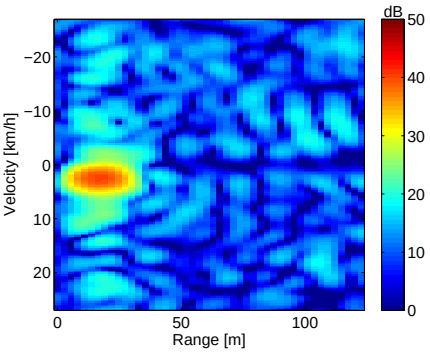

(c) 2D-CCF + AF control and cancellation

Figure 5.3: Target detection experiment in indoor environment

5.4 The overall WiFi-based PBR processing scheme

The WiFi-based PBR processing scheme is sketched in Figure 5.4 which includes the main stages of AF control and cancellation.

Specifically, it can be considered as an extension of the scheme discussed in Section 3.3 with the introduction of the disturbance removal stage. In particular, the approximation of Equation 2.2 suggests a simple and effective way to estimate the cancellation filter weights by averaging over different pulses; thus, when exploiting mixed transmissions, the cancellation filter weights can be separately estimated for DSSS and OFDM pulses by averaging over pulses exploiting the same modulation. Two different sets of filter weights are then retained to be effectively used against DSSS and OFDM pulses.

The process starts after the pulse detection and the modulation recognition that are performed by the proper block.

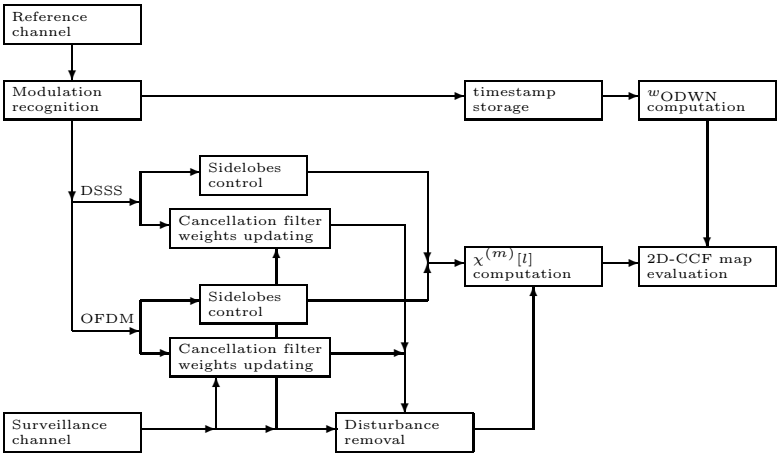

Figure 5.4: WiFi-based PBR processing scheme with AF control and disturbance removal

Chapter 6

Toward the real-time implementation of the WiFi-based passive radar processing scheme

As of today, the exponential growth in digital technology, together with the corresponding decrease in its cost, has had a profound impact on the way radar systems are designed. Specifically, more and more functions that historically were implemented in analog hardware, are now being performed digitally, resulting in increased performance and flexibility and reduced size and cost. Moreover, advances in analog-to-digital converter (ADC) and digital-to-analog converter (DAC) technologies are pushing the border between analog and digital processing closer and closer to the antenna.

Aiming at moving the WiFi-based passive radar toward the real-

time working, in this Chapter the possibility of performing some stages of the processing scheme depicted in Figure 5.4 on FPGA (Field-Programmable Gate Array) devices in investigated. In particular, a way to implement the processing scheme for the evaluation of the auto/cross-correlation between the reference and the surveillance signals, is presented.

The analysis reported in the following, has been performed with reference to a specific device, the Spartan 3E Starter Kit board, which is briefly presented in Section 6.1. With reference to the FPGA's specific properties, the processing scheme has been designed by exploiting the MathWorks Simulink® software and is discussed in Section 6.2.

6.1 Spartan 3E Starter Kit board

The Spartan 3E Starter Kit board is depicted in Figure 6.1. For the purpose of the analysis reported in the following, just a few features of the board will be here discussed. Much more details can be found in the open documentation available on the Internet (see, as an example, [12]).

The core of the board consists of the Xilinx XC3S500E FPGA, which is characterized by 232 Input/Output pins and 20 dedicated 18×18 multipliers. An on-board USB interface - together with the board's control software - allows to download the VHDL code to program the FPGA.

Two input ADCs with programmable gain amplifiers are available to convert input signals into a 12-bit digital data stream which directly runs into the FPGA. On the other side, four output DAC can be used if the FPGA is conceived to generate specif waveforms.

Finally, a 50 MHz internal clock oscillator provides timing for the entire board.

Different softwares are provided to enable the possibility of both designing proper processing algorithms and downloading the corresponding VHDL codes onto the FPGA. Specifically, the System

Generator tool comes with a dedicated Simulink® Xilinx plugin which provide system modeling and automatic code generation for the specific FPGA target. The Xilinx blocks, used to fit the specific features of the FPGA target, will be blu-highlighted in the designed Simulink® model.

The generated code can be then downloaded onto the FPGA via the USB interface by using the ISE control software.

Hardware/Software co-simulation is also possible to verify that the developed code really fits the FPGA being used.

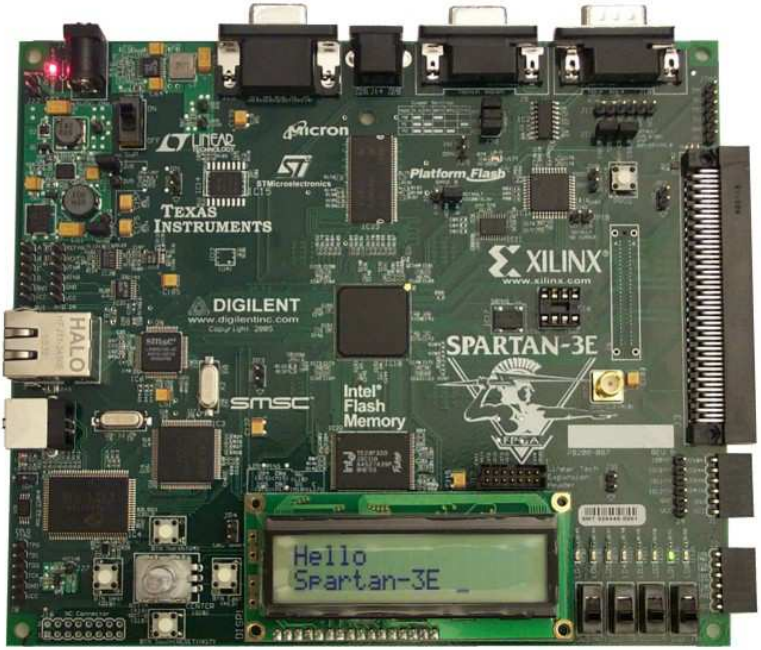

Figure 6.1: The Spartan3E Starter Kit board.

6.2 Simulink® models for WiFi-based passive radar

The Simulink® model for the evaluation of the auto/cross-correlation among the reference and the surveillance signals, is reported in Figure 6.2.

The baseband input signals (i.e. the reference and the surveillance signals) are provided directly from the Matlab® workspace with a sampling frequency of 11 MHz (DSSS transmissions case), thus allowing to emulate the behavior of the cascade of both a down-conversion and an ADC (see the four blocks with the "From Workspace" label in Figure 6.2) stages. Specifically, 18 bits are used for each sample of the real/imaginary part of each signal (which results in a total utilization of 72 FPGA Input pins). Under the assumption of pulse durations of about 0.5 ms with an equivalent pulse repetition time of 1 ms, the input data rate will be approximately 396 Mbps.

The output of the Simulink® model consists of the 36 bit-samples of the auto/cross-correlation among the reference and the surveillance signals evaluated for the first 12 time bins (see the four blocks with the "To Workspace" label in Figure 6.2). Each output signal will be provided to the Matlab® workspace for the subsequent processing stages (i.e., cancellation) with a total utilization of 144 FPGA Output pins. Notice that, the time delay corresponding to 12 bins results in a bistatic range of about 330 meters which is a reasonable value for the considered short range application. Under these assumptions, the output data rate will be approximately 864 bps, with a significant reduction with respect to the input data rate without any loss of information.

The following Subsection describes with detail the main processing stages of the sketch in Figure 6.2.

6.2.1 Simulink® processing stages

The main issue of the real-time work-flow design - with respect to conventional off-line processing - is the efficient utilization of the available hardware resources. For the particular case of the Xilinx XC3S500E FPGA, this limit is fixed by the 20 dedicated multipliers. In a first rough approximation, by considering that a complex multiplier requires four dedicated multipliers, the Xilinx XC3S500E FPGA would be able to perform five complex multiplications per time beat which would be not sufficient to perform the evaluation of the auto/cross-correlation for the WiFi-based passive radar.

To cope with this limit, a couple of considerations might be done.

i First of all, it should be noted that a complex multiplication might be performed by using three dedicated multipliers instead of four. Infact, if $s_{\rm tx} = a + \iota b$ and $s_{\rm ref} = c + \iota d$, the multiplication between a samples of $s_{\rm tx}$ and a sample of $s^*_{\rm ref}$ (useful to evaluate the auto-correlation function) might be performed as follows:

$$\begin{aligned} s_{\rm tx} \cdot s^*_{\rm ref} &= [(a+b)c - b(c-d)] + \iota[b(c-d) - d(a-b)] \\ &= ac + bd + \iota(bc - ad) \end{aligned} \tag{6.1}$$

which means that both the real and the imaginary parts of the complex product might be evaluated by using a total number of three dedicated multipliers. Similarly, it could be possible to evaluate the cross-correlation function by defining $s_{\rm surv} = a_{\rm surv} + \iota b_{\rm surv}$ (the complex multiplier implemented in Simulink® is shown in Figure 6.4).

ii Secondly, as previously mentioned, the FPGA timing is provided by an internal 50 MHz clock while the sampling frequency of the input signals has been set to 11 MHz. By up-rating the input data with an oversampling factor of 4, it will be possible to use a single dedicated multiplier up to four times in a time beat.

The above considerations have been taken into account in the design of the FPGA processing scheme sketched in Figure 6.2.

In fact, the first stage "Preparation of the input signals for processing" has been considered to perform the additions/subtractions required to implement the complex multiplier (see Equation 6.1). Notice again that the samples of the reference signal have been denoted with c and d, for the real and the imaginary part, respectively, while the samples of the transmitted/surveillance signals have been denoted with a/a_{surv} and b/b_{surv} for the real and the imaginary parts, respectively.

Three main blocks ("ACF e CCF tau 0 1 2 3", "ACF e CCF tau 4 5 6 7" and "ACF e CCF tau 8 9 10 11") are used to evaluate the samples of both the real and the imaginary parts of the auto/cross-correlation functions. Each block performs the evaluation of four range bins by exploiting the up-rating operation discussed above (over-sampling factor equal to 4). In particular, as shown in Figure 6.3, the evaluation of the auto/cross-correlation is performed by resorting to a multiply-and-accumulate approach. Notice that, a control circuit (shown in the left-bottom part of Figure 6.2) is required to provide synchronization to the accumulators and correctly enable them.

A time delay line (three steps of 0, 4 and 8 total time delay bins, as shown in Figure 6.2)) is used to provide to each "ACF e CCF" block a version of the reference signal properly delayed to evaluate the corresponding auto/cross-correlation bins.

Each output of each "ACF e CCF" block is provided at the input of a corresponding multiplexer which is then used to correctly provide the output stream of the system. In particular, four multiplexer are used which correspond to the real/imaginary part of the auto/cross-correlation functions. A proper control circuit (see the upper-right zone of Figure 6.2) is used to properly enable the input of each multiplexer so as to provide to the Matlab® workspace the 12 range bins-samples of the auto/cross-correlation functions.

The proposed scheme has been tested on the Xilinix XC3S500E FPGA by means of the software/hardware co-simulation tool thus demonstrating its effectiveness.

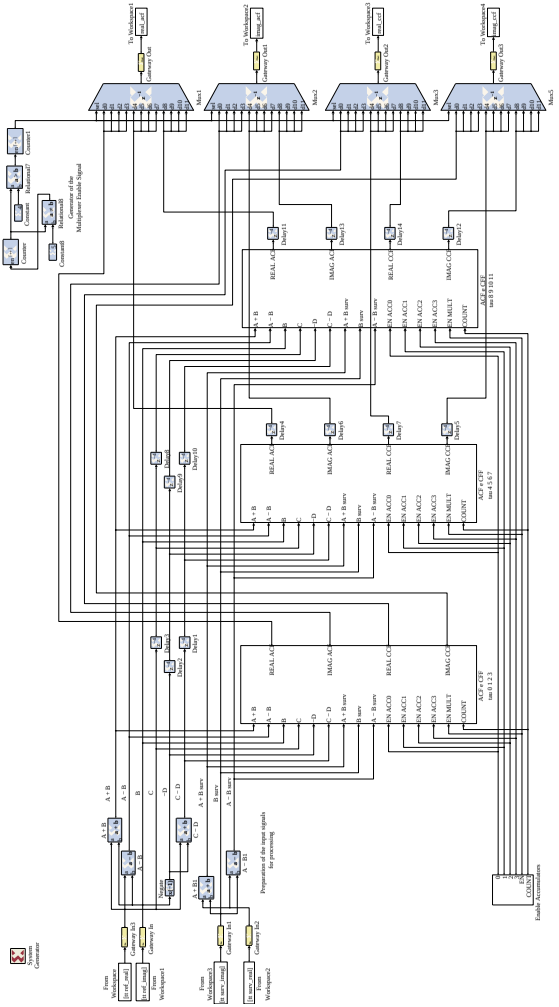

Figure 6.2: Simulink® model for auto/cross-correlation evaluation.

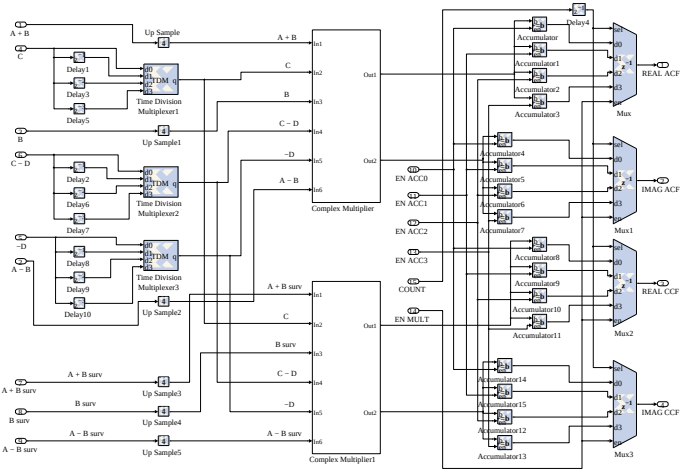

Figure 6.3: Auto/cross-correlation evaluation block (4 taps delay).

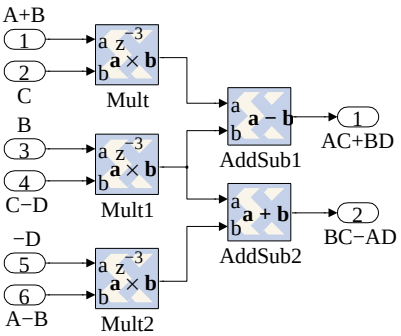

Figure 6.4: Simulink® complex multiplier.

Notice that, further real-time processing strategies could be considered with the aim of performing more and more operations per second.

As an example, the complex multiplier in Figure 6.4 has been implemented with three 18×18 dedicated multipliers and provides 36-bits output words. Actually, its performance in terms of complex multiplications per second, might be doubled easily if 6-bits samples are used as input words as described in following.

Assume that a single multiplier would be used to perform two multiplications:

$$\begin{aligned} a \cdot b &= x \\ c \cdot d &= y \end{aligned} \tag{6.2}$$

where a, b, c and d are 6-bits words and x and y are 12-bits words.

The inputs a and c might be sent at the first 18-bits input of a dedicated multiplier by forming its first input word α:

$$\alpha = a + c \times 2^{12} \tag{6.3}$$

Similarly, b and d will form the latter input word of the dedicated multiplier:

$$\beta = b + d \times 2^{12} \tag{6.4}$$

The output of the dedicated multiplier will be:

$$\begin{aligned} \zeta = \alpha \times \beta &= a \cdot b + a \cdot d \times 2^{12} + b \cdot c \times 2^{12} + c \cdot d \times 2^{24} \\ &= x + (a \cdot d + b \cdot c) \times 2^{12} + y \times 2^{24} \end{aligned} \tag{6.5}$$

meaning that the desired output x can be taken from the first 12 bits of the output word ζ, while the desired output y can be taken as the higher order 12 bits of the same output word ζ.

Obviously, while doubling the number of multiplications per second, such an approach is paid in terms of dynamic range (6 bits input word must be used instead of 18 bits word). However, for the case of real WiFi-based passive radar, such an approach has been

verified to provide comparable performance with respect to the case of 18 bits input words (this is typically due to the low power collected at the surveillance channel).

Chapter 7

Extraction of the reference signal from the surveillance channel

The results reported in the previous Chapters are based on the exploitation of a quite pure reference signal directly collected at the output of the AP. This was reasonably appropriate for the purpose of the reported analysis aimed at preliminary testing the data processing techniques and the experimental setup. However this approach corresponds to a particular PBR case where the transmitter is assumed to be partially cooperative (its signal is accessible directly using a directional coupler, without the degradation caused by a wireless propagation channel). In typical PBR applications, a dedicated receiving antenna is used to collect the transmitted signal to be used as a reference for the following processing. This usually prevents the availability of a very clean reference signal which is instead affected by multipath contributions. Moreover, this approach still requires an additional receiving channel to collect the reference signal which is paid in terms of system complexity.

Based on the digital nature of the exploited signals of opportunity, in this Chapter, the attractive possibility of avoiding the use of the additional receiving channel to collect the transmitted signal (reference signal) is investigated. In particular, in Section 7.1 it is shown that the reference signal can be properly extracted from the data collected at the surveillance receiving channel by exploiting the knowledge of the IEEE 802.11 Standards. The effectiveness of the proposed approach will be shown against the target detection Experiment C in Section 7.2.

7.1 Operational principle

The proposed approach starts by noticing that the samples collected at the surveillance channel contain, together with the echoes from the targets and the stationary obstacles, also a scaled (attenuated) version of the transmitted signal that typically is received by the surveillance antenna sidelobes. Despite the attenuation can be rather strong for directional surveillance antennas, its one-way path typically provides lower propagation loss than for target and clutter/multipath echoes, so that it represents very often the main contribution in the received surveillance signal.

In particular, when DSSS signals are exploited, if a matched filter for the 11-chip Barker code (namely we apply the 11-chip Barker code de-spreading) is applied to the surveillance signal, the result is very similar to the de-spreading of the original transmitted signal (as collected at the output of the AP by using the directional coupler and the dedicated receiving channel). This is clearly apparent from Figure 7.1, that compares the de-spreading outputs. Specifically the high values (peaks) of the two sequences show very similar values, while the differences (due to the presence of the target and clutter echoes in the surveillance channel) are apparent mainly in the low level values.

Since the digital waveform demodulation is essentially based on the decision applied to the complex values at the peaks, the recon-

struction of the symbols sequence potentially yields only few errors even for not very high SNR values.

Notice that a similar approach can be used when HR-DSSS and OFDM transmissions are exploited, by properly modifying the demodulation scheme according to the physical layer specifications. A lower symbol error rate can be expected for the DSSS signals thanks to the processing gain accomplished by chipping the baseband signal with an 11-chip Barker code. However, in all cases, proper equalization techniques and optimized demodulation and decoding schemes might be exploited for error correction and better recovery of the transmitted signal, as those typically implemented in standard WiFi receivers.

This approach in principle eliminates the effects of other signal contributions such as multipath and target echoes.

A quite pure reference signal may be obtained by modulating again the extracted symbol sequence according to the 802.11 Standard physical layer specifications. This allows to obtain a clean copy of the reference signal directly from the surveillance signal without requiring a dedicated receiving channel. As apparent, this is an alternative and highly attractive approach to collect the reference signal samples that is based on the digital nature of the transmitted signals used by the WiFi-based PBR.

The scheme of principle for the reconstruction can be obtained by demodulating the signal collected at the surveillance channel to extract the sequence of transmitted symbols and by applying the modulation process, as sketched in Figure 7.2 for the DSSS case.

While the structure of the scheme is basically coincident with the cascade of standard WiFi demodulation and modulation schemes, a few points require specific attention for the WiFi-based PBR case:

i a carrier shift compensation stage is required to estimate the deviation of the transmitter carrier frequency from the nominal channel frequency; this not only provides correct demodulation, but also the reconstruction of a synchronous reference waveform, that can be used for the following PBR processing stages. A

residual carrier frequency deviation would significantly degrade the performance of the sidelobe reduction techniques, that can be affected by deviations from the theoretical autocorrelation function. Unlike in the wireless communication case, a fast PLL is not required, because the data are processed after a complete batch is collected. In contrast the whole collected batch can be exploited to accurately estimate the phase slope by averaging over the whole batch of data.

ii other than the average carrier drift, the phase noise or short term carrier drift must be maintained (or better re-introduced) inside the reconstructed reference signal, so as to avoid a degradation of the cancellation performance, and the reduction of the quality of the long coherent integration. This phase error term is estimated by averaging, on a pulse basis, the difference between the original phase values and the post-decision phase values at each symbol. The estimated phase error is then re-applied to the sequence of symbols after the hard decision stage.

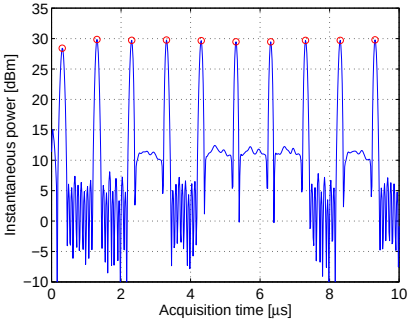

(a)

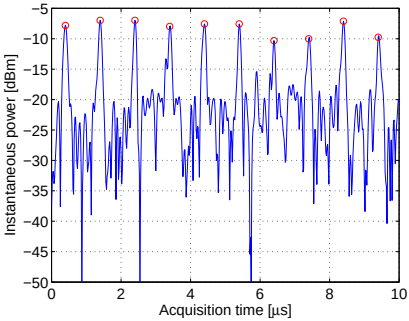

(b)

Figure 7.1: De-spreading outputs for: (a) the original transmitted signal (collected at the output of the AP); (b) the signal collected at the surveillance channel.

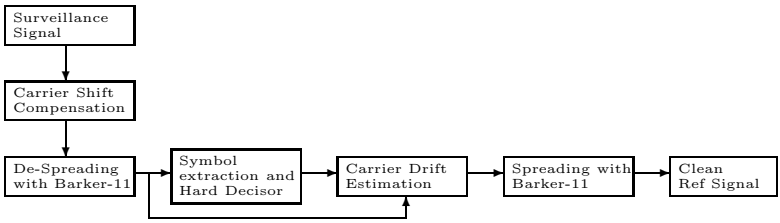

Figure 7.2: Scheme of principle for the reference signal reconstruction from the surveillance signal (DSSS case).

7.2 Experimental results

The results obtained with this approach are reported in Figure 7.3 for Experiment C using the same scaling factors and thresholds of Figure 4.9. The results obtained with the recovered version of the reference signal are largely comparable with those obtained with the reference signal directly collected at the output of the AP. The numerous tests performed showed that, after disturbance removal and sidelobes control, the detection capability of the considered system remains almost unchanged. The slight differences are due to the impossibility to simulate the exact behaviour of the transmitter and the receiver, there including their filter transfer functions and their instantaneous carrier frequency and phase noise characteristics.

Notice that the proposed approach has a great interest in a wider range of PBR systems exploiting digital waveforms (e.g. DVB-T, DAB, GSM signals). Specifically, as far as the reference signal can be directly recovered from the signal collected at the surveillance antenna, it allows to remove the need for a dedicated receiving channel thus significantly reducing the system complexity. Nevertheless, when the transmitted signal has to be collected by a directive antenna or a dedicated beam synthesized from an electronically steerable array of antennas to guarantee an acceptable SNR, the proposed approach is still able to yield a significant performance improvement since it might yield a cleaner version of the reference signal with reduced multipath or other disturbance contributions.

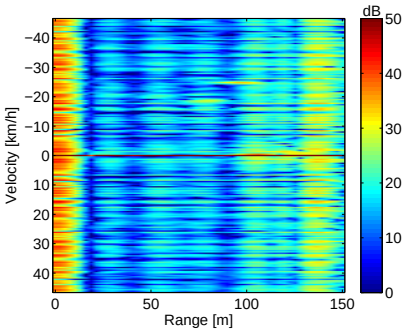

(a) Range/velocity map

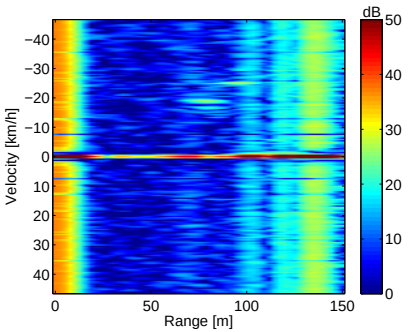

(b) Range/velocity map + AF control

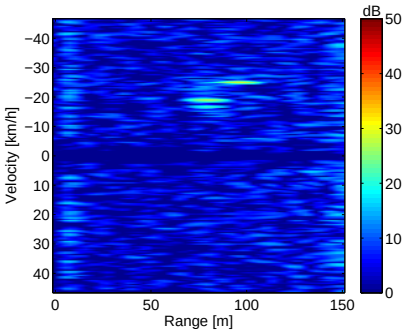

(c) Range/velocity map + AF control and cancellation

Figure 7.3: Range/velocity maps for Experiment C evaluated with the recovered version of the reference signal.

Chapter 8

Vehicular target localization and tracking

According to the results reported in the previous Chapters, the availability of a single passive radar sensor allows target detection and localization over the range/Doppler plane only. However when target localization is required in an assigned area, its x-y coordinates should be estimated. To this purpose, multiple passive radar sensors can be exploited which allow to collect a set of range/Doppler measures for the same target which is observed at different bistatic geometries. Moreover, assuming that each sensor uses a couple of surveillance antennas, an interferometric approach can be exploited to estimate the Direction of Arrival (DoA) of the target echo. This obviously increases the set of available measures thus potentially improving the localization capability of the conceived system. However, since different measures (range/Doppler/DoA) might be characterized by different accuracies, proper localization strategies should be designed to jointly exploit them.

Aiming at widening the range of possible application of the WiFi-based passive radar, in this Chapter different localization algorithms are presented and the corresponding experimental results are shown. Such results have been obtained by exploiting different subsets of the available measures collected by means of a WiFi-based passive radar prototype developed and fielded at the DIET Dept. - University of Rome "La Sapienza" in real experiments performed using vehicular targets in a wide outdoor area.

In particular, this Chapter is organized as follows. Section 8.1 describes the experimental setup and the acquisitions scenario while the processing stages required to extract the range/Doppler frequency/DoA measures from the collected data are discussed in Section 8.2. The localization algorithms are described in Section 8.3 together with the experimental results. Specifically, the different algorithms are based on the following measures sets: (i) range measures, (ii) Doppler-prefiltered range measures, (iii) a single range measure and the target's echo DoA, and (iv) two range measures and the target's echo DoA (distinguishing between the least square solution and the solution based on the maximum likelihood estimator). Finally, the possibility of estimating the target's velocity is investigated in Section 8.4 by also exploiting the Doppler-frequency measurements.

8.1 Acquisition campaign of year 2012

To investigate the potentialities of the WiFi-based PBR in target localization, a dedicated acquisition campaign was performed in February 2012.

8.1.1 Experimental setup and Scenario

The passive radar prototype used to perform the experiments is sketched in Figure 8.1.

A commercial WiFi access point was used as transmitter of opportunity. Its antenna output was connected to the transmitting antenna while a directional coupler was used to send a -20 dB copy of the transmitted signal to the first receiving channel of a four-channel receiving system. This allowed to collect the reference signal. At the same time, three surveillance antennas were directly connected to three separate channels of the four-channel receiving system with the aim of collecting the surveillance signals. After a fully coherent base-band down-conversion stage, the signals are sampled at 22 MHz and stored for off-line processing. The WiFi access point used as transmitter of opportunity is a DLINK DAP 1160 with the following main characteristics:

- selectable WiFi channel;
- selectable output power; and
- selectable data-rate.

The -20 dB directional coupler (T AC02520) provides isolation greater than 30 dB.

The antennas used to perform the experiments are commercial WiFi antennas for indoor applications (DLINK ANT24-1200 - sizes $33 \times 9.3 \times 2.07$ cm). They are characterized by:

- 80 degrees beam-width over the horizontal plane;
- 23 degrees of beam-width over the vertical plane;
- 12 dBi of gain; and
- 15 dB of front-to-back ratio.

Once the surveillance signals are collected, the WiFi-based passive radar processing scheme reported in Figure 5.4 is applied against the collected signals separately at each receiving channel.

Figure 8.2 depicts the outdoor scenario where the experimental test was performed. It consists of a wide parking area located in

Cisterna di Latina, a small town near Rome. As depicted in Figure 8.2, a single transmitter of opportunity (TX) and 3 receiving sensors (RX) were used to perform the experiments. In particular, as depicted in Figure 8.3, the TX was located at the point represented with the coordinates (0,0) m while the first receiver (RX 1) was located in (25,0) m in a bistatic configuration with respect to the transmitter of opportunity. RX 2 and RX 3 were placed a few tens of centimeters below the TX, both in a quasi monostatic configuration with the transmitter of opportunity. Moreover, their relative distance was set in order to enable targets Direction of Arrival (DoA) estimation by exploiting an interferometric approach.

Finally, Figure 8.4 depicts the GPS receiver used to collect the ground truth and the car used as target. While the car moved to perform the localization test, the GPS received collected the ground truth depicted in Figure 8.2 with the blue curve.

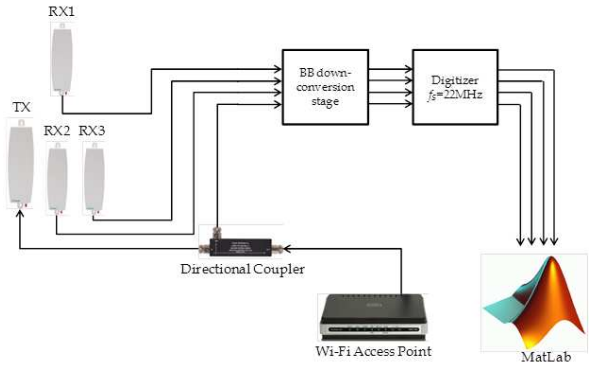

Figure 8.1: Sketch of the WiFi-based PBR prototype.

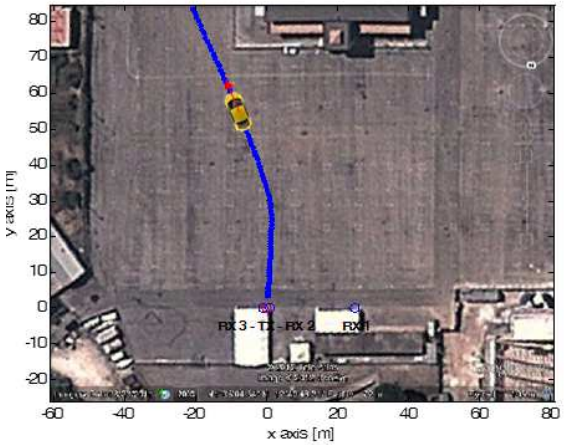

Figure 8.2: Acquisition scenario and test's ground truth.

Figure 8.3: Antennas dislocation.

Figure 8.4: GPS receiver and vehicular target.

8.1.2 Data collection

As previously mentioned, signals from three different surveillance antennas are collected by means of the experimental setup sketched in Figure 8.1. Then, the WiFi-based passive radar processing scheme depicted in Figure 5.4 is applied against the collected surveillance signals separately at each receiving channel. In particular:

i the proposed sidelobes reduction techniques are applied in order to guarantee an acceptable useful dynamic range;

ii the disturbance removal step is performed by adopting the Extensive Cancellation Algorithm (ECA) described in [11] with a batch duration equal to 100 ms over a range of 300 m;

iii a coherent integration time of 0.5 s is used to evaluate the 2D-CCF over consecutive portions of the acquired signals (frames) with a fixed displacement of 0.1 s (10 frames per second are thus obtained); and

iv target detection is performed by resorting to a simple adaptive detector based on the cell-average CFAR (a cross-shape for the distribution of the reference cells was chosen with a total number of reference cells per frame set to 45,080 and the probability of false alarm was set to 10^{-4}).

Since the particular antennas geometry, the detections performed over the first receiving channel (the bistatic receiver, RX 1) allow to collect a set of bistatic range and Doppler frequency measurements (namely, R_{B1} and f_{D1}) for the considered target. On the other side, a two-out-of-two detection criterion can be adopted for the second and the third receiving channels (RX 2 and RX 3, both in a quasi monostatic configuration with respect to TX) which allows to collect a second set of range and Doppler frequency measurements (namely, R_{B2} and f_{D2}) while reducing the probability of false alarm. Moreover, the phase difference between RX 2 and RX 3 measured at the target detection point is exploited to obtain the target DoA

estimation. Notice that the DoA estimation will be provided with reference to the TX antenna boresight which is steered along the y axes.

As an example, with reference to the experiment whose ground truth is shown in Figure 8.2, Figure 8.5 shows all the performed detection over the range/Doppler frequency plane (for the bistatic receiver RX 1 and the quasi-monostatic receiver RX2-3 in Figure 8.5(a) and 8.5(b), respectively).

From Figure 8.5, it clearly appears that different kinds of detections are performed that might be mainly organized as follows:

- false alarms - False alarms might be easily discarded by a tracking algorithm. Moreover, from a direct visual comparison between the range/Doppler frequency planes shown in Figure 8.5, it clearly appears that the number of false alarms is significantly reduced by the adoption of the two-out-of-two detection criterion performed for the receiving channels RX 2 and RX 3;

- detections which are likely to correspond to target returns - Such detections appear at negative Doppler frequency locations and increasing bistatic range (that is in line with the test geometry, since the target moves forward the antennas location); and

- multipath effects - For the considered experiment, multipath effects might be caused by the double-bounce reflection of the target echo over the building in the upper zone of Figure 8.2 (see the sequence of detections at positive Doppler frequency and decreasing bistatic range between 250 and 150 m in both Figures 8.5(a) and 8.5(b)).

The following Section focuses on the processing stages required to select the detections corresponding to the targets echo. The measurements related to such kind of detections will be then used to localize and track the target.

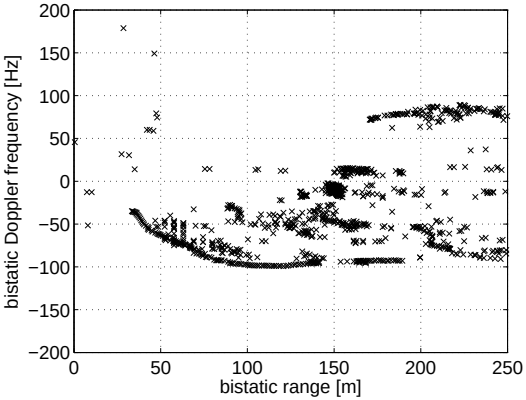

(a) Bistatic couple TX/RX1

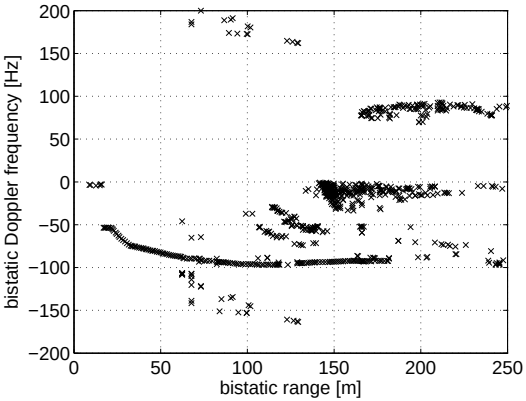

(b) Quasi-monostatic couple TX/RX2-3

Figure 8.5: Collected detections for both the bistatic couples.

8.2 Data processing and plots selection

As previously discussed, a number of different kinds of detection are performed within the experiment depicted in Figure 8.2 distinguishing above all between false alarms, true target's returns and double bounce multipath effects. Aiming at investigating the potentialities of the WiFi-based PBR system in target localization, the detections corresponding to the true target's returns have to be identified and used to take the measurements of interest (bistatic range, bistatic Doppler frequency and phase difference between RX2 and RX3 at the target detection point).

To this purpose, a simple linear filtering strategy (based on the Kalmans algorithm) has been considered together with the knowledge of the Scenario's geometry.

In particular, the adopted selection strategy includes the following main stages:

- the plots (range/Doppler frequency/DoA measures) collected at the generic time-step are used to predict the subsequent system state;
- at the next time-step, among all the available plots suitable for association, the closest one to the prediction is selected and the algorithm is reiterated.

This really allows to discard the false alarms but not the false tracks formation. In particular, for the considered experiment, it is likely that a false track would form from the sequence of detections due to the double bounce multipath of the target echo over the building in the upper zone of Figure 8.2. However, since in this case the area to be surveyed is characterized by a maximum dimension $y = 80$ m, a track whose initialization bistatic range is greater than 250 m, is automatically discarded.

As an example for the considered experiment, Figure 8.6 shows with the green circle markers the plots selected for the subsequent localization algorithms.

The selected plots provide the target bistatic range for RX1 and RX2-3 reported, respectively, in Figure 8.7(a) and Figure 8.7(b). As is apparent, the collected measures are well in line with the test geometry (see Figure 8.2). In fact, while the target moves, both the bistatic ranges increase with the bistatic range of RX 1 increasing slower. Similarly, when the target is far from the antennas location, the measured range are almost the same, since both the observation angle become quite similar and almost monostaic.

Moreover, the phase-difference between RX 2 and RX 3 at the target detection point can be used to estimate the targets echo DoA. The result is shown in Figure 8.7(c). As is apparent, also the estimated DoA is well in line with the test geometry, in fact, while the target moves toward negative values of x, also the DoA become negative.

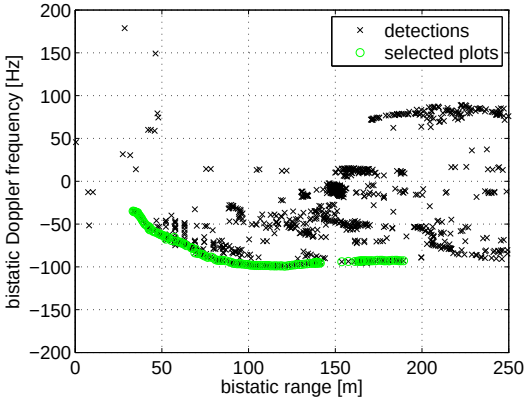

(a) Bistatic couple TX/RX1

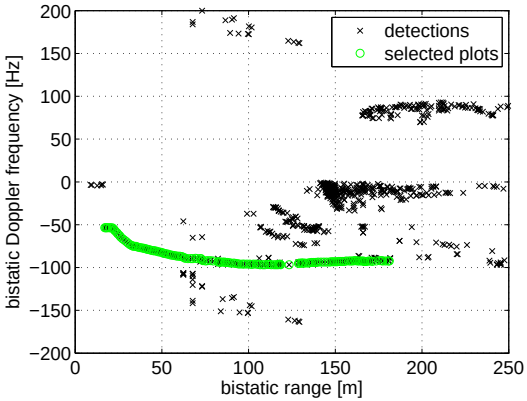

(b) Quasi-monostatic couple TX/RX2-3

Figure 8.6: Selected plots for both the bistatic couples.

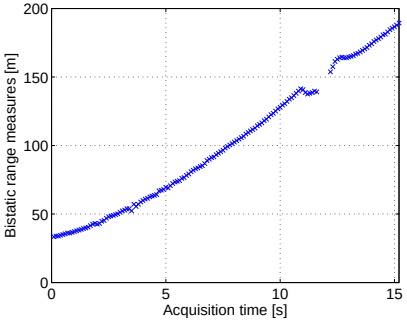

(a) Bistatic range TX/RX1

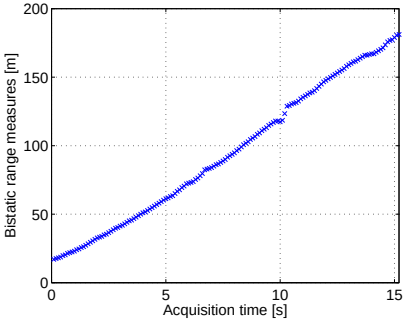

(b) Bistatic range TX/RX2-3

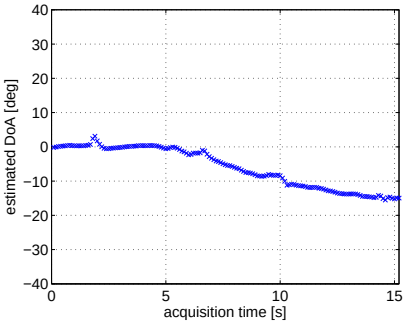

(c) Direction of Arrival

Figure 8.7: Measures taken from the selected plots of Figure 8.6.

8.3 Localization algorithms and performance

Once the range/Doppler frequency/DoA measures have been taken from the selected data, different localization algorithms can be investigated and their performance can be compared. In the following, the treatment is organized in different localization algorithms based on different subsets of the available measures.

8.3.1 Use of range measures

Firstly, target localization is performed based on the exploitation of the range measures only. A bistatic ellipse is drawn for each bistatic couple. The intersection points of two bistatic ellipses give an estimation of the target position over the x-y plane (the ambiguous solution is discarded by forcing the target to be within the antennas main lobe). As a result, the sequence of red 'x' markers in Figure 8.8 represents the estimated target positions.

As is apparent, localization errors in the order of meters are experienced along the x dimension while the track follows the actual motion of the target along the y dimension. In particular, the worst localization performance is experienced when the target is far from the surveillance antennas. In fact, in such locations the bistatic ellipses become quite similar and almost tangent, thus increasing the Dilution of Precision (DOP) factor along the x dimension.

Table 8.1 summarizes the performance of the proposed localization strategy.

	Raw range-based Localization
Max error	32.65 m
Mean error	4.81 m
Error standard dev.	5.78 m

Table 8.1: Performance of localization based on range measures only.

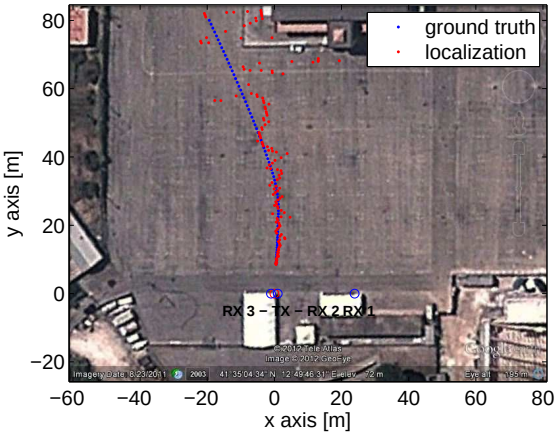

Figure 8.8: Localization based on two range measures.

8.3.2 Use of Doppler-prefiltered range measures

The target localization performance might be improved if more accurate target range estimates are available from each surveillance channel (each bistatic couple). These can be obtained by applying a conventional tracking algorithm (like the Kalmans one) over the range/Doppler frequency plane, separately for the two surveillance channels. The result is reported in Figures 8.9(a) and 8.9(b) for RX1 and RX2-3, respectively. As is apparent, the exploitation of the Doppler frequency measures allows to obtain more accurate range measures with respect to the raw case.

The filtered range measures might be then exploited as discussed in the previous step (intersection of the bistatic ellipses) to obtain a more stable estimation of the target position over the x-y plane. This result is shown with the sequence of the red 'x' markers in Figure 8.9(c). As is apparent, the localization accuracy is significantly improved and the resulting track is almost identical to the actual path of the car. The slight differences are due to clutter residuals which might affect the estimation of the target range and Doppler frequency.

Table 8.2 summarizes the performance of the proposed localization strategy. As is apparent, a significant improvement is obtained with respect to the previous case.

	Filtered range-based Localization	Improvement
Max error	6.64 m	26 m
Mean error	2.47 m	2.4 m
Error standard dev.	1.53 m	4.25 m

Table 8.2: Performance of localization based on filtered range measures only.

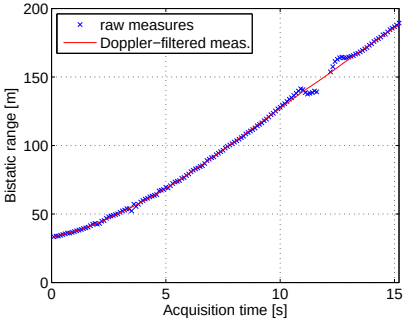

(a) Doppler-filtered bistatic range for RX1

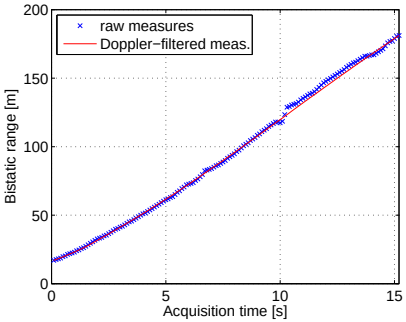

(b) Doppler-filtered bistatic range for RX2-3

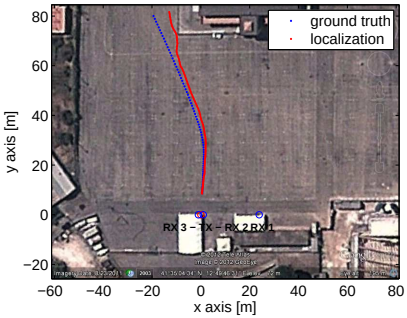

(c) Localization

Figure 8.9: Localization based on two Doppler-filtered range measures.

8.3.3 DoA estimation and localization

A typical way to localize targets with a passive radar system, consists in the exploitation of the range and DoA measures provided by a single couple of receivers displaced very close each other (as in the case of RX2 and RX3 of the configuration discussed in Section 8.1). To this purpose, it could be possible to use the Doppler-filtered version of the bistatic range RX2-3 and the estimation of the Direction of Arrival ϑ reported, respectively, in Figure 8.9(b) and Figure 8.7(c).

Specifically, since the DoA is provided with respect to the antennas boresight, the target's coordinates (x_t,y_t) might be estimated as follows:

$$\begin{aligned} x_t &= \frac{R_{B2}}{2} \sin\vartheta \\ y_t &= \frac{R_{B2}}{2} \cos\vartheta \end{aligned} \tag{8.1}$$

The localization results for the considered approach are shown in Figure 8.10 while Table 8.3 summarized the obtained performance. As is apparent, the exploitation of the quite accurate phase difference measure, allows to significantly improve the localization performance.

	Single range and DoA-based Localization	Improvement
Max error	2.56 m	4.1 m
Mean error	1.79 m	0.7 m
Error standard dev.	0.54 m	1 m

Table 8.3: Performance of localization based on a single filtered range measure and the DoA.

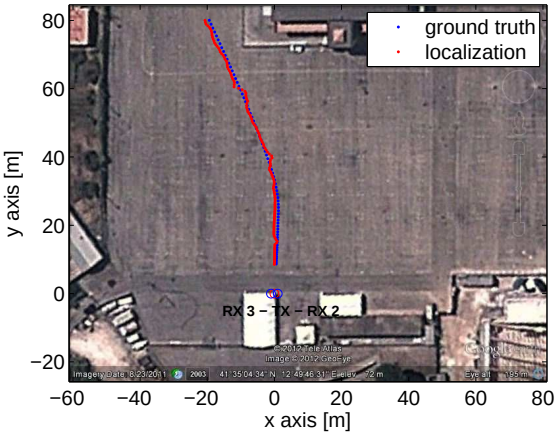

Figure 8.10: Localization based on a single Doppler-filtered range measure and the DoA.

8.3.4 Localization with two range measures + DoA

The results previously reported, are based on the exploitation of just two measures among the set of the collected data (two range measures, two pre-filtered range measures and a single range measures together with the DoA). In this section, the subset of the measures exploited to perform target localization is widen by considering both the range measures and the DoA.

Aiming at still estimating two unknowns (the targets' x-y coordinates), two possible approaches will be discussed both based on the solution of a non-linear system equation. Finally, the performance obtained against the experimental test depicted in Figure 8.2, will be evaluated and compared.

LS solution

First of all, the available measures can be written as function of the instantaneous target position as follows:

$$\begin{aligned} R_{B1} &= f_1(x_t, y_t) = \sqrt{(x_{TX} - x_t)^2 + (y_{TX} - y_t)^2} + \\ &\quad + \sqrt{(x_1 - x_t)^2 + (y_1 - y_t)^2} \\ R_{B2} &= f_2(x_t, y_t) = 2\sqrt{(x_{TX} - x_t)^2 + (y_{TX} - y_t)^2} \\ \vartheta &= f_\vartheta(x_t, y_t) = \arctan(x_t / y_t) \end{aligned} \tag{8.2}$$

where:

i R_{B1} has been written as the sum of the paths transmitter-target and target-receiver;

ii R_{B2} has been written as twice the transmitter-target distance (it has been reasonably assumed that the antennas RX 2 and RX 3 are in a quasi monostatic configuration with respect to the transmitter of opportunity); and

iii the angle of arrival ϑ has been written as the inverse tangent of the target's abscissa divided by the target's ordinate.

Notice that, as is well known, the collected measures are non-linear functions of the target position.

Aiming at estimating the target position (x_t-y_t), firstly the system of Equations 8.2 has to be linearized. To do this, each equation in the System 8.2 might be expanded about the target approximate point ($\mathbf{P}_0 = [x_{t0}\ y_{t0}]^T$) using a Taylor series truncated after the first order partial derivatives to eliminate nonlinear terms.

It is obtained:

$$\begin{aligned} R_{B1} &= R_{B1,0} + a_{1,x}(x_t - x_{t0}) + a_{1,y}(y_t - y_{t0}) \\ R_{B2} &= R_{B2,0} + a_{2,x}(x_t - x_{t0}) + a_{2,y}(y_t - y_{t0}) \\ \vartheta &= \vartheta_0 + a_{\vartheta,x}(x_t - x_{t0}) + a_{\vartheta,y}(y_t - y_{t0}) \end{aligned} \tag{8.3}$$

where $R_{B1,0}$, $R_{B2,0}$ and ϑ_0 represent, respectively, the functions f_1, f_2 and f_ϑ evaluated at the target approximate point ($\mathbf{P}_0 = [x_{t0}\ y_{t0}]^T$):

$$\begin{aligned} R_{B1,0} &= f_1(x_{t0}, y_{t0}) \\ R_{B2,0} &= f_2(x_{t0}, y_{t0}) \\ \vartheta_0 &= f_\vartheta(x_{t0}, y_{t0}) \end{aligned} \tag{8.4}$$

and the coefficients $a_{n,x}$ and $a_{n,y}$ represent the partial derivatives of $f_n(x_t, y_t)$ with respect to x_t and y_t, respectively.

By defining the following matrix structures:

$$\begin{aligned} \mathbf{\Delta M} = \mathbf{M} - \mathbf{M_0} &= \begin{bmatrix} R_{B1} \\ R_{B2} \\ \vartheta \end{bmatrix} - \begin{bmatrix} R_{B1,0} \\ R_{B2,0} \\ \vartheta_0 \end{bmatrix} \\ \mathbf{H} &= \begin{bmatrix} a_{1,x} & a_{1,y} \\ a_{2,x} & a_{2,y} \\ a_{\vartheta,x} & a_{\vartheta,y} \end{bmatrix} \\ \mathbf{\Delta P} &= \begin{bmatrix} x_t \\ y_t \end{bmatrix} - \mathbf{P}_0 \end{aligned} \tag{8.5}$$

the system of Equations in 8.3 can be written in matrix form as:

$$\mathbf{\Delta M} = \mathbf{M} \cdot \mathbf{\Delta P} \tag{8.6}$$

where:

i the elements of the vector $\mathbf{M}$ depend on the collected range/DoA measures by representing the difference between the actual values of R_{B1}, R_{B2} and ϑ and their predictions;

ii the elements of the matrix $\mathbf{H}$ depend on the relative geometry between the target and the sensors; and

iii the elements of the vector $\mathbf{P}$ represent the difference between the target position and the approximate point $\mathbf{P}_0$.

Finally, the least square (LS) solution of the system in Equation 8.6 is given by:

$$\mathbf{\Delta P} = (\mathbf{H}^{-1}\mathbf{H})^{-1}\mathbf{H}^{-1}\mathbf{\Delta M} \tag{8.7}$$

Which gives the target position updating with respect to the approximate point $\mathbf{P}_0$.

Once $\mathbf{P}$ is computed, the target position $[x_t \ y_t]^T$ is updated according to the definition of $\mathbf{\Delta P}$. This linearization scheme will work well as long as the displacement $\mathbf{\Delta P}$ is within close proximity of the linearization point. The acceptable displacement is dictated by the positioning accuracy requirements. If the displacement exceeds the acceptable value, this process is reiterated with the current $\mathbf{M}_0$ until the maximum admitted number of iterations is reached.

Once target localization has been performed for each frame of the available data, the result can be drawn over the x-y plane obtaining the track reported in Figure 8.11 with the red sequence of the 'x' markers. The ground truth collected by means of the GPS receiver, is reported again with the blue-dotted curve for a fair direct comparison.

Table 8.2 summarizes the performance of the proposed localization strategy. As is apparent, the exploitation of both the available range measures causes a degradation of the localization performance with respect to the previous case (exploitation a single range measure and the DoA).

	Filtered range and DoA-based Localization	Improvement
Max error	6.6 m	-4 m
Mean error	2.03 m	-0.2 m
Error standard dev.	1.61 m	-1.1 m

Table 8.4: Performance of localization based on filtered range measures and the DoA.

However, it should be remarked that the adopted estimation procedure corresponds to the maximum likelihood (ML) estimator of the target position whenever the joint probability density function of the available measurements is Gaussian distributed with identical variances. However, this is not the case of the data collected to perform the localization experiment depicted in Figure 8.2 being each measure characterized by its own accuracy. In fact, the DoA estimation is certainly characterized by a different accuracy with respect to the range measures. Moreover, range measures collected by different sensors are characterized by different accuracies whenever the target signal to noise ratio (SNR) at the detection point is different at each receiving channel.

The above considerations should be taken into account in order to better exploit the collected measure thus making it possible to improve the obtainable localization performance. To accomplish such result, in the next Section an alternative target localization procedure is described based on a ML estimator that takes into account that different measures are characterized by different accuracies.

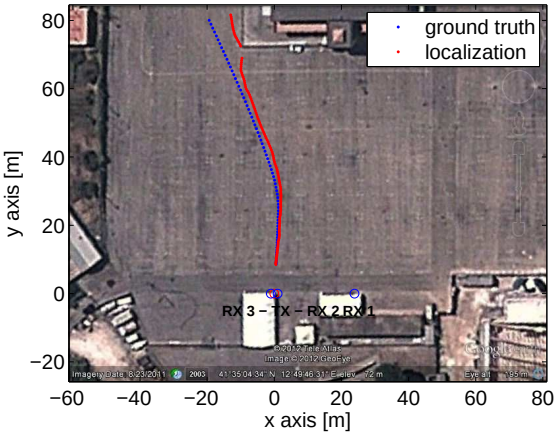

Figure 8.11: Localization based on two Doppler-filtered range measure and the DoA.

ML estimator

The localization procedure discussed in the following has been conceived with the aim of improving the performance shown in the previous sub-section while still exploiting the same measurements set. In particular, a ML estimator is derived with the aim of also exploiting the knowledge of the accuracy of the collected measures.

To accomplish this result, it is firstly assumed that the joint probability density function of the observed data is normally distributed. From Equation 8.6, it can be written as:

$$\wp_{\mathbf{\Delta M}} = \mathcal{N}(\mathbf{H} \cdot \mathbf{\Delta P}, \mathbf{\Sigma_M}) \tag{8.8}$$

where $\mathbf{H} \cdot \mathbf{\Delta P}$ represents the mean value of the collected measures while their covariance matrix $\mathbf{\Sigma_M}$ is given by:

$$\mathbf{\Sigma_M} = \begin{bmatrix} \sigma_{R1}^2 & 0 & 0 \\ 0 & \sigma_{R2}^2 & 0 \\ 0 & 0 & \sigma_{\vartheta}^2 \end{bmatrix} \tag{8.9}$$

where σ_{R1}^2, σ_{R2}^2 and σ_{ϑ}^2 are the variance of R_{B1}, R_{B2} and ϑ, respectively. Moreover, it has been reasonably assumed that the cross-covariance between the collected measures is equal to zero.

Thus, under these assumptions, the ML estimator for the target position updating vector $\mathbf{\Delta P}$ might be derived by solving the following minimization problem:

$$\min_{\mathbf{\Delta P}} = \left\{ (\mathbf{\Delta M} - \mathbf{H\Delta P})^T {\mathbf{\Sigma_M}}^{-1} (\mathbf{\Delta M} - \mathbf{H\Delta P}) \right\} \tag{8.10}$$

which has the solution:

$$\mathbf{\Delta P} = (\mathbf{H}^T {\mathbf{\Sigma_M}}^{-1} \mathbf{H})^{-1} \mathbf{H}^T {\mathbf{\Sigma_M}}^{-1} \mathbf{\Delta M} \tag{8.11}$$

As is apparent, the target position updating vector obtained by resorting to the ML estimation approach, depends not only on the collected measures and the target-sensors geometry (as in the case

discussed in the previous sub-section, Equation 8.7), but also it depends on the accuracy of the available measures. Obviously, this result would correspond to the result of Equation 8.7 whenever the observed data are characterized by the same variance (i.e. the case in which $\mathbf{\Sigma_M} = \sigma^2\mathbf{I}_3$).

If target localization is now performed - per each frame - through the iterative procedure described in the previous sub-section and accordingly to the target position updating vector of Equation 8.11, a new sequence of localizations is obtained which is depicted in Figure 8.12 with the red-dotted sequence of markers. The ground truth collected by means of the GPS receiver is reported again with the blue-dotted sequence of markers for a direct fair comparison.

As is apparent, in this case the target positioning gives a better result with respect to the case previously discussed. In particular, the estimation procedure discussed above allows to significantly reduce the deviations of the target track from the ground truth clearly visible in Figure 8.11. This obviously is due to a better exploitation of the DoA measure while solving the system of Equations 8.6. This is allowed by a weighted use of the single measurements according to their own accuracies. The performance of the ML estimator with respect to the case discussed in the previous sub-section are summarized in Table 8.5.

	ML Estimator	Improvement
Max error	1.79 m	4.8 m
Mean error	0.8 m	1.2 m
Error standard dev.	0.38 m	1.2 m

Table 8.5: Performance of localization based on filtered range measures and the DoA with the ML Estimator.

To give the feel of the improvement of the localization performance, it has to be noted that the maximum deviation between the ground truth and the estimated target position reduces to approximately 1.8 m (the improvement with respect to the previous case is about 5 m) while the improvement in both the mean error and the

error standard deviation is about 1.2 m.

Finally, it has to be noticed that the estimator of Equation 8.11 would be derived even by considering a LS estimator - as in the case discussed the previous sub-section - in which the functional to be minimized is weighted accordingly to the accuracies of the single measurements:

$$\min_{\mathbf{\Delta P}} = \left\{ \left| \mathbf{\Sigma_M}^{-1/2} (\mathbf{H\Delta P} - \mathbf{\Delta M}) \right|^2 \right\} \tag{8.12}$$

By solving the minimization problem reported in Equation 8.12, the result of Equation 8.11 is obtained.

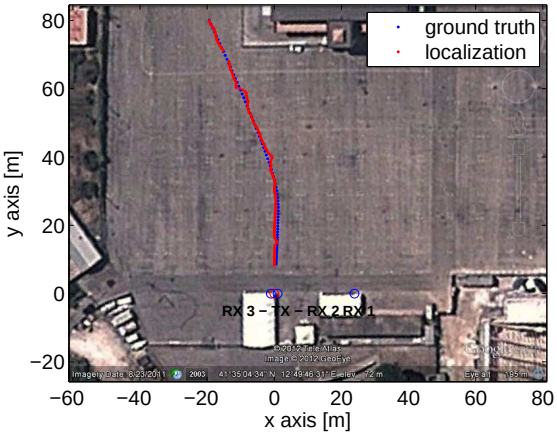

Figure 8.12: Localization based on two Doppler-filtered range measure and the DoA (ML Estimator).

8.3.5 Overall localization performance

In this Section different localization strategies have been investigated for the case of the WiFi-based PBR with reference to an experiment performed with a vehicular target. By collecting signals up to three surveillance channels simultaneously, it was possible to build up a set of two bistatic range and two bistatic Doppler frequency measurements for the target which is observed at different bistatic geometries. Moreover, by exploiting the phase difference at the target detection point between two properly displaced surveillance antennas and by resorting to an interferometric approach, it has been shown that it is possible to estimate the targets echo angle of arrival.

The evaluation of the performance of different localization algorithms, allows to highlight some specific points for the case of the WiFi-based passive radar:

i the exploitation of the bistatic range measures should follow a preliminary filtering stage over the range)Doppler frequency plane (e.g., as that based on the Kalman's algorithm) to improve the accuracy of the range measures by exploiting the more accurate Doppler frequency measures;

ii the availability of the target's echo DoA allows to strongly improve the localization performance, since it follows the estimation of the quite accurate phase-difference between two receiving channels at the target detection point; and

iii whether localization is performed through the solution of a non-linear system of more-than-two equations into two unknowns, the knowledge of the single measure's accuracy should be taken into account to properly exploit the available data.

In particular, the localization approach proposed in sub-section 8.3.4 (based on the ML solution of a non linear system of more-than-two equations in two unknowns) suggests the possibility of widening the

measurements set (i.e., increase the number of equations) to estimate also the target's velocity (or, better, its x-y components).

This attractive possibility is investigated in the next Section.

8.4 Target's velocity estimation

As previously mentioned, it could be possible, in principle, to estimate the target's velocity components by resorting to a similar approach as that discussed in sub-section 8.3.4.

First of all, the system of Equations 8.2 can be rewritten by also including the bistatic Doppler frequency measures for both the receivers:

$$
\begin{aligned}
R_{B1} &= \sqrt{(x_{TX}-x_t)^2+(y_{TX}-y_t)^2}+\sqrt{(x_1-x_t)^2+(y_1-y_t)^2} \\
R_{B2} &= 2\sqrt{(x_{TX}-x_t)^2+(y_{TX}-y_t)^2} \\
f_{D1} &= \frac{1}{\lambda}\left[\frac{(x_{TX}-x_t)v_x}{\sqrt{(x_{TX}-x_t)^2+(y_{TX}-y_t)^2}}+\right. \\
&\quad +\frac{(y_{TX}-y_t)v_y}{\sqrt{(x_{TX}-x_t)^2+(y_{TX}-y_t)^2}}+ \\
&\quad \left.+\frac{(x_1-x_t)v_x}{\sqrt{(x_1-x_t)^2+(y_1-y_t)^2}}+\frac{(y_1-y_t)v_y}{\sqrt{(x_1-x_t)^2+(y_1-y_t)^2}}\right] \\
f_{D2} &= \frac{1}{\lambda}\left[\frac{(x_{TX}-x_t)v_x}{\sqrt{(x_{TX}-x_t)^2+(y_{TX}-y_t)^2}}+\right. \\
&\quad +\frac{(y_{TX}-y_t)v_y}{\sqrt{(x_{TX}-x_t)^2+(y_{TX}-y_t)^2}}+ \\
&\quad \left.+\frac{(x_2-x_t)v_x}{\sqrt{(x_2-x_t)^2+(y_2-y_t)^2}}+\frac{(y_2-y_t)v_y}{\sqrt{(x_2-x_t)^2+(y_2-y_t)^2}}\right] \\
\vartheta &= \arctan(x_t/y_t)
\end{aligned}
\tag{8.13}
$$

As is apparent, the Doppler frequency depends not only on the rel-

ative position between the target and the sensors, but also on the target's velocity components v_x-v_y.

Following the procedure described in sub-section 8.3.4, the system of Equations 8.13 can be linearized and written in a matrix form:

$$\underbrace{\begin{bmatrix} R_{B1} \\ R_{B2} \\ f_{D1} \\ f_{D2} \\ \vartheta \end{bmatrix}}_{\mathbf{M}} = \underbrace{\begin{bmatrix} \frac{\partial R_{B1}}{\partial x} & \frac{\partial R_{B1}}{\partial y} & \frac{\partial R_{B1}}{\partial v_x} & \frac{\partial R_{B1}}{\partial v_y} \\ \frac{\partial R_{B2}}{\partial x} & \frac{\partial R_{B2}}{\partial y} & \frac{\partial R_{B2}}{\partial v_x} & \frac{\partial R_{B2}}{\partial v_y} \\ \frac{\partial f_{D1}}{\partial x} & \frac{\partial f_{D1}}{\partial y} & \frac{\partial f_{D1}}{\partial v_x} & \frac{\partial f_{D1}}{\partial v_y} \\ \frac{\partial f_{D2}}{\partial x} & \frac{\partial f_{D2}}{\partial y} & \frac{\partial f_{D2}}{\partial v_x} & \frac{\partial f_{D2}}{\partial v_y} \\ \frac{\partial \vartheta}{\partial x} & \frac{\partial \vartheta}{\partial y} & \frac{\partial \vartheta}{\partial v_x} & \frac{\partial \vartheta}{\partial v_y} \end{bmatrix}}_{\mathbf{H}} \underbrace{\begin{bmatrix} x_t \\ y_t \\ v_x \\ v_y \end{bmatrix}}_{\mathbf{x}} \tag{8.14}$$

where the partial derivatives are evaluated at the target approximate point ($\mathbf{P}_0 = [x_{t0}\ y_{t0}\ v_{x,t0}\ v_{y,t0}]^T$). Finally, following the approach presented in sub-section 8.3.4, the target position/velocity updating will be given by:

$$\mathbf{\Delta P} = (\mathbf{H}^T {\mathbf{\Sigma_M}}^{-1} \mathbf{H})^{-1} \mathbf{H}^T {\mathbf{\Sigma_M}}^{-1} \mathbf{\Delta M} \tag{8.15}$$

where the elements of the covariance matrix now also include the variance of the Doppler frequency measurements:

$$\mathbf{\Sigma_M} = \begin{bmatrix} \sigma^2_{R1} & 0 & 0 & 0 & 0 \\ 0 & \sigma^2_{R2} & 0 & 0 & 0 \\ 0 & 0 & \sigma^2_{fD1} & 0 & 0 \\ 0 & 0 & 0 & \sigma^2_{fD2} & 0 \\ 0 & 0 & 0 & 0 & \sigma^2_{\vartheta} \end{bmatrix} \tag{8.16}$$

If target localization and velocity estimation is now performed - per each frame - through the iterative procedure described in sub-section 8.3.4 and accordingly to the target position updating vector of Equation 8.15, the obtained target's velocity x-y components are reported in Figures 8.13(a)-8.13(b), respectively, compared with the ground truth and the velocity components obtained as time derivatives of the estimated position components.

As is apparent, the ML solution provides the estimation of the target's velocity components with improved accuracy with respect to the case of time derivatives of the position components. This is obviously due to the exploitation of both the Doppler frequency measurements and the knowledge of the measurements accuracy.

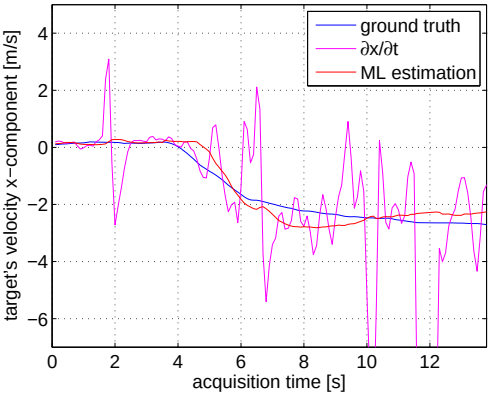

(a) v_x component.

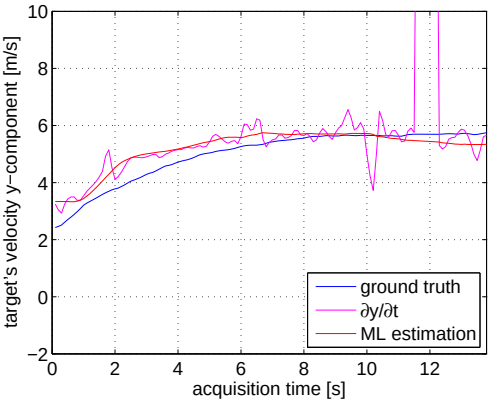

(b) v_y component.

Figure 8.13: Estimated target's velocity components.

Chapter 9

High resolution cross-range profiling of moving targets

The experimental results reported in the previous Chapters provide a demonstration of the potentialities of the WiFi-based PBR in detection, tracking and localization of moving targets. However, it should be noted that the proposed processing scheme is not able to distinguish between different types of targets, even if they could be properly detected and tracked. In particular, this is an important issue to be addressed in the design of a surveillance system for short range applications, since it is expected that a great variety of targets could be present in such kind of scenarios. As an example, when interested in the surveillance of a wide parking area like in the examples previously discussed the most common kinds of potential targets span from motorized ones (cars, motorbike, trucks), to un-motorized ones (bicycles, trolleys), to humans and to animals.

Aiming at distinguishing between different kinds of targets, advanced processing strategies are introduced in following with the

aim of providing an image, or at least a cross-range profile, of the observed scene. To this purpose, in the following, the possibility of applying ISAR processing schemes to the WiFi-based passive radar, is investigated with the aim of obtaining high resolution cross-range profiles of the detected moving targets.

The reported results - obtained against both simulated and real data acquired in specif target profiling experimental tests - preliminarily show the potentialities of such kind of an approach for the considered application.

9.1 Geometrical considerations and ISAR constraints

Once a moving target has been detected, the range compressed data can be exploited to obtain a high resolution cross-range profile at the corresponding range bin via the ISAR processing. The ISAR step includes the estimation of the target motion parameters relevant to focusing and the cross-range profile formation and scaling. Specifically, for the short range surveillance application under consideration, both range and Doppler cell migration might be observed in the acquired passive bistatic ISAR range compressed data. This is due to the long CPI (Coherent Processing Interval) used, to the target velocity and its trajectory direction and to the relative position of both the TX and RX with respect to the target. Thus an effective processing scheme has to take into account both these effects.

To explain the ISAR processing, the geometry of Figure 9.1 is considered with target moving at a given velocity (v_x, v_y) and passing through the point ($x = 0$, $y = y_0 = R_0$) at time aperture centre t_0. The transmitter of opportunity is located in ($x = 0$, $y = 0$) and the surveillance antenna in ($x = x_{RX}$, $y = y_{RX}$) and steered to the point (0, R_0). When ($x_{RX} = 0$, $y_{RX} = 0$), i.e. receiver collocated with the transmitter, a quasi-monostatic acquisition is obtained, Figure 9.1(a), while when ($x_{RX} \neq 0$, $y_{RX} \neq 0$) a bistatic

acquisition with bistatic angle β is achieved, Figure 9.1(b). Obviously $\beta = 0$ in the quasi-monostatic acquisition. As typical in ISAR the two-way radar-target distance can be approximated around time t_0 as a polynomial law, namely as a Taylor series at order N:

$$\begin{aligned} R_t(t) &= \sqrt{x_t(t)^2 + y_t(t)^2} + \sqrt{(x_t(t) - x_{RX})^2 + (y_t(t) - y_{RX})^2} \approx \\ &= R_t(0) + 2\sum_{n=1}^{N} \alpha_n \frac{(t - t_0)^n}{n!} \end{aligned} \tag{9.1}$$

where $x_t(t) = v_x(t - t_0)$, $y_t(t) = R_0 + v_y(t - t_0)$. A compact explicit expression can be found for the coefficients up to the second order, namely for $R_t(0)$, α_1 and α_2:

$$\begin{aligned} R_t(0) &= R_0 + \sqrt{(x_{RX}^2 + R_0^2)} = 2\frac{R_0 \cos^2(\beta/2)}{\cos\beta} \\ \alpha_1 &= \cos(\beta/2)\big[\cos(\beta/2)v_y - \sin(\beta/2)v_x\big] \\ \alpha_2 &\approx \frac{4\cos^2(\beta/2)\big[\cos(\beta/2)v_x + \sin(\beta/2)v_x\big]^2}{R_t(0)} = \frac{4\cos^2(\beta/2)v_{cr}^2}{R_t(0)} \end{aligned} \tag{9.2}$$

where v_{cr} is the target speed in cross-range direction. The simple expression reported for α_2 is exact in the quasi-monostatic case and approximated in the bistatic case and applies for moderate values of the bistatic angle and when the target is moving with a dominant cross-range speed (this is the case we are interested in, otherwise the cross-range profile cannot be obtained). In the considered case, for the short range acquisition geometry (see Figure 9.1) and motion conditions it is sufficient to set $N = 3$.

As is apparent from the above equations, the echoes from the target can thus be interested by range cell migration (mainly range walk due to the radial velocity, namely α_1) and the corresponding phase history, $\varphi_t(t) = 2\pi R_t(t)/\lambda$, is therefore characterized by quadratic and cubic phase terms, that need to be compensated to perform coherent integration over the long CPI required to achieve the high cross-range resolution. Unfortunately, as typical in the ISAR case,

the target motion parameters are unknown and thus must be estimated from the received echoes via autofocus. To this purpose a range strip centered on the range of the detected target is selected from the range compressed data and given in input to the target motion estimation procedure. An effective approach to obtain the parameter estimation is to search for the set of values (α_1, α_2, α_3) that provides the best quality for the focused profile. Therefore, for any assigned set (α_1, α_2, α_3) the procedure applies as follows:

1. remove the range migration related to α_1 by transforming the data in the fast-frequency slow-time domain, by multiplying the transformed data by:

$$\Phi_1 = \mathrm{e}^{\iota 2\pi f \frac{2\alpha_1 t}{c}} \tag{9.3}$$

   being f the fast-frequency and by inverse Fourier transforming the data back in the range slow time domain;

2. remove the Doppler migration related to α_2 and α_3 by multiplying the compensated range bin by the reference signal:

$$\Phi_2 = \mathrm{e}^{\iota \frac{2\pi}{\lambda}\left(\alpha_2 t^2 + \alpha_3 \frac{t^3}{3}\right)} \tag{9.4}$$

   and go in the cross-range profile domain by Fourier transform.

The estimated ($\hat{\alpha}_1$, $\hat{\alpha}_2$, $\hat{\alpha}_3$) values can be chosen as those values which minimize the entropy, [13], evaluated over the cross-range profile at the output of step 2 above. As is apparent, this needs to be repeated for a high number of times, either by performing a full search in the 3D parameter space with an assigned spacing for the parameter values, or by following a path in the 3D parameter space accordingly to a specific optimization strategy. To limit the computational burden of this search, the minimization over the three parameters is split in two successive minimizations over two parameters. In the first one a quadratic phase model is used and ($\hat{\alpha}_1$, $\hat{\alpha}_2^{(in)}$) are obtained being $\hat{\alpha}_2^{(in)}$ a first raw estimate of the Doppler chirp

rate. Following this first estimation step, range migration is compensated accordingly to $\hat{\alpha}_1$ and from the compensated data the range bin interested by the target is selected. The selected bin, together with $\hat{\alpha}_2^{(in)}$, is then provided in input to the second estimation step where the cubic phase model is exploited and ($\hat{\alpha}_2$, $\hat{\alpha}_3$) are finally obtained.

Once the $R_t(0)$ value is known from the selected range bin, and the estimate of $\hat{\alpha}_2$ is obtained, also the target cross-range velocity can be obtained as $\hat{v}_{cr}$, which is directly used to scale the Doppler axis, thus mapping Doppler frequencies into cross-range distances. Moreover, this allows also to evaluate the global Doppler bandwidth B_D and the azimuth resolution r_a, given by:

$$B_D = \frac{2}{\lambda}\alpha_2 T \qquad r_a = \frac{v_{cr}}{B_D} = \frac{\alpha R_t(0)}{4\cos(\beta/2)^2 v_{cr} T} \tag{9.5}$$

For example, under the hypothesis of $R_0 = 50$ m, ($v_x = 4.5$ m/s, $v_y = 0$ m/s) and $T = 6$ s, the obtainable resolution in the azimuth dimension is in the order of tens of centimeters.

By exploiting the experimental setup described in Section 4.1, different tests were performed in a parking area in Cisterna di Latina (Italy) using different acquisition geometries as described in Table 9.1.

test ID	geometry	# of targets	y_0 [m]	v_x [m/s]	v_y [m/s]
M1	monostatic	1 car	50	$\pm$4.5	0
M2	monostatic	2 cars	50	$\pm$4.5	0
B1	bistatic	1 car	30	$\pm$4.5	0
B2	bistatic	2 cars	30	$\pm$4.5	0

Table 9.1: ISAR experimental tests description.

A quasi-monostatic configuration was adopted in tests M1 and M2 (see Figure 9.1(a)), being the surveillance antenna mounted just above the transmitting antenna. In both cases the targets move along the axis $y = y_0 = 50$ m (dashed line in Figure 9.1(a)) at about $v_x = 4.5$ m/s. In particular, in test M1, a single car was present

(a Fiat Punto Evo) with length of about 4 meters; different data files were recorded with the car moving in opposite directions (i.e. eastward, $v_x = 4.5$ m/s, or westward, $v_x = -4.5$ m/s) and approximately crossing the point $(x_0\ y_0) \equiv (0$ m 50 m$)$ at the middle of the acquisitions. For test M2 a second identical car was employed moving behind the first car with a separation of about 3/4 meters along the x-axis so that, at the middle of the acquisition, they were almost symmetrically displaced about the point (0 m 50 m). Similar tests were performed in cases B1 and B2 using a bistatic acquisition geometry with TX/RX baseline equal to 15 m along the x-axis (see Figure 9.1(b)). In the reported bistatic experiments, the targets move along the axis $y = y_0 = 30$ m at about $v_x = 4.5$ m/s, crossing the point $(x_0\ y_0) \equiv (0$ m 30 m$)$ at about the middle of the acquisition.

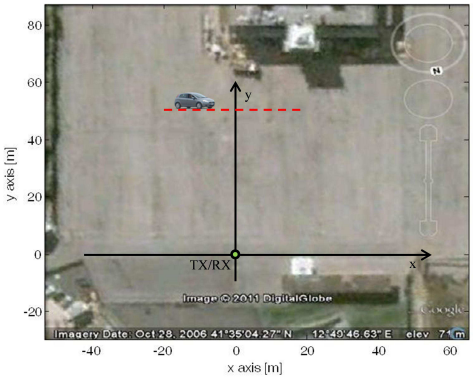

(a)

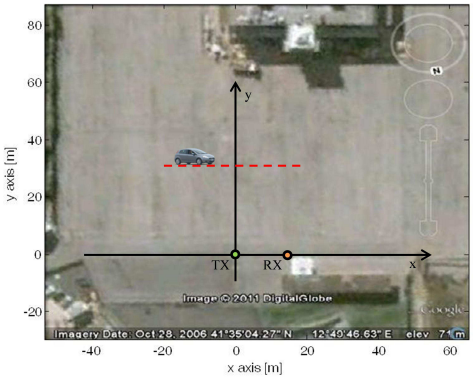

(b)

Figure 9.1: Sketch of the acquisition geometries adopted for the experimental tests: (a) monostatic geometry; (b) bistatic geometry.

9.2 The WiFi-based passive ISAR processing scheme

The overall WiFi-based passive ISAR processing scheme is sketched in Figure 9.2.

Notice that the first blocks in Figure 9.2 are in common with the PBR processing scheme for target detection so that the additional required processing steps can be nicely integrated in the basic scheme to provide the final system with advanced ISAR capability. Specifically, in the following it is shown that the range compressed data after disturbance cancellation have to be exploited to avoid strong contributions from stationary scatterers, i.e. disturbance cancellation is a required step also in the passive ISAR mode.

Such effect is here demonstrated using a real data set collected by means of the experimental setup described in Section 4.1 using the same acquisition geometry depicted in Figure 9.1(a)-9.1(b). Specifically a controlled test was performed by acquiring a 6 seconds data file in the absence of moving targets. The echo of a fictitious target is then injected in the collected data assuming that its motion resembles the real target in Test M1 (see Figure 9.1(a)). In particular it has been assumed that, during the CPI of 6 s, the fictitious target moves from point (x_A, y_A)=(-13.5 m, 50 m) to point (x_B, y_B)=(13.5 m, 50 m) with velocity v_x=4.5 m/s, distance of minimum approach R_0=50 m, and signal-to-noise ratio SNR=-20 dB.

Figure 9.3 shows the Doppler spectrum of the overall signal (target+clutter, black curve): for comparison the Doppler spectrum of the signal containing only the target is also reported (target only, blue curve). As is apparent a strong component appears at zero Doppler (due to the stationary scene) which is well above the contribution of the fictitious scatterer (the almost rectangular shape appearing from Doppler frequency -20 Hz to +20 Hz approximately). This is expected to strongly affect the autofocus and clearly shows the need for a disturbance cancellation stage that removes it.

However, being the cancellation algorithm ECA (presented in

Chapter 5) intrinsically adaptive, it might have a non negligible impact on the signals backscattered from the moving targets. Specifically, the ECA is expected to strongly attenuate the target signal components at low Doppler frequencies since they are recognized as stationary contributions and included in the adaptive estimation of the cancellation weights. Such an effect is clearly visible from the red curve in Figure 9.3 which reports the Doppler spectrum of the overall signal after the application of the conceived cancellation strategy. As is apparent, when the ECA is applied, the disturbance component is effectively removed. However, as expected, the cancellation filter has dramatically distorted the target spectrum shape at low Doppler frequencies. Such effect might significantly reduce the quality of the ISAR profiling thus, in the next Section, a 'target preserving cancellation strategy' is presented.

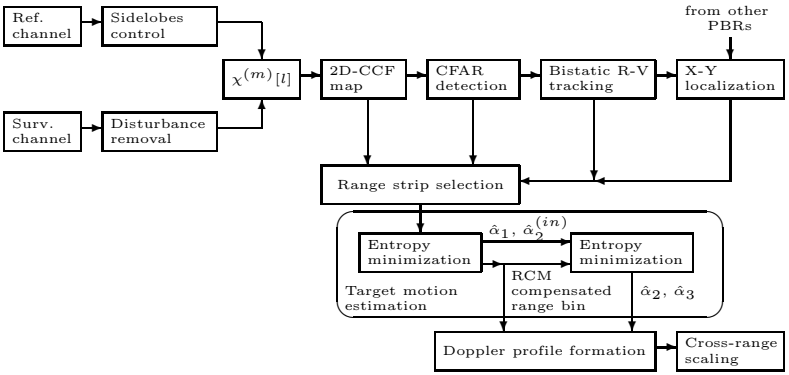

Figure 9.2: WiFi-based passive ISAR processing scheme.

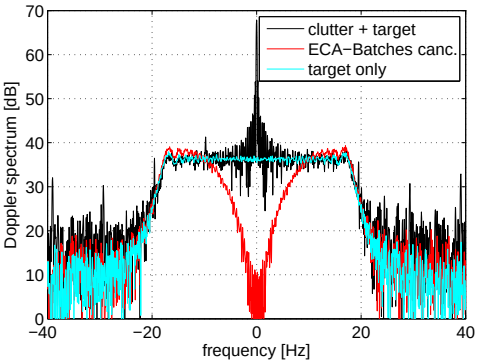

Figure 9.3: Signal Doppler spectrum.

9.3 ECA-based fixed-batch cancellation

From Figure 9.3, it can be easily noticed that the filter cancellation notch in the Doppler frequency dimension prevents the possibility of obtaining a quite complete Doppler spectrum of the fictitious target. In particular, this is the case of the tests considered in Table 9.1. In fact, while the car moves along the cross-range direction, a zero-Doppler crossing is performed over the bistatic range/Doppler plane. Such an effect might reduce the quality of the ISAR profiling, especially if CPI in which the target performs a zero-Doppler crossing are considered.

To cope with this potential limit, an ECA fixed batch cancellation strategy is proposed, aiming at removing (or, at least, reducing) the stationary back-ground (the disturbance component) while preserving the target signal. The proposed approach starts from the assumption that the strongest disturbance components in the observed scene are stationary during the ISAR CPI. Under this hypothesis, the disturbance contribution to the cross-correlation between the transmitted signal and the received (surveillance) signal is constant along the CPI. The ECA-based fixed batch cancellation strategy is obtained by estimating and updating the cancellation filter weights only at signal fragments that do not contain target contributions at low Doppler frequencies. These signal fragments can be easily identified when, as usual, the ISAR processing follows the target detection and tracking stages. In fact such stages usually require shorter CPIs with respect to the ISAR processing so that they yield a reasonable estimate of the target instantaneous Doppler frequency over consecutive sub-CPIs. Therefore the sub-CPIs yielding high Doppler values can be exploited to update the cancellation filter weights that will be then applied against the subsequent sub-CPIs until a favourable sub-CPI is encountered.

To show the effectiveness of the proposed approach, Figure 9.4 reports with the magenta line the obtained Doppler spectrum for the same case of Figure 9.3. As is apparent, when the proposed 'target preserving cancellation strategy' is considered, not only the

disturbance contribution has been quite removed, but also the target signal has been effectively preserved.

To understand the impact of the clutter cancellation issue on the following ISAR processing, Figure 9.5 reports a cut of the entropy cost function obtained for the considered experiment as a function of the normalized estimation error of the focus parameter α_2 (the Doppler chirp rate), namely $\delta\alpha_2/\alpha_2^0 = (\hat{\alpha}_2 - \alpha_2^0)/\alpha_2^0$ being α_2^0=0.39887 m/s^2 for the considered case study. As is apparent, in absence of the cancellation stage (black curve), the estimation of α_2 is unfeasible: the entropy curve does not show any minimum in correspondence to the true value of the focus parameter (namely at about $\delta\alpha_2/\alpha_2^0 = 0$). In contrast, when a cancellation strategy is applied, the entropy curve shows a marked minimum which allows a reasonable estimation of the target motion parameters thus allowing the correct formation of the cross-range profiles.

As is apparent, both the cancellation strategies (standard ECA Batches or ECA with Fixed Batch) provide good performance in the estimate of the target motion parameter; moreover the behavior of the entropy function obtained on the signal after clutter cancellation is very similar and close to the entropy behavior observable in presence of target only, which is here used as a benchmark.

In the next Section, the performance of the proposed processing scheme will be analyzed with reference to data sets concerning real vehicular targets.

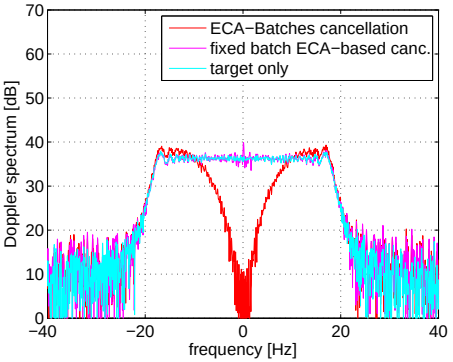

Figure 9.4: Signal Doppler spectrum after cancellation.

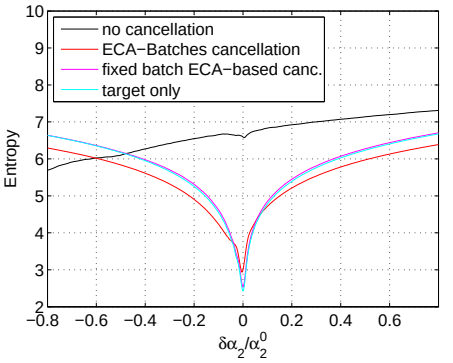

Figure 9.5: Entropy cost function versus α_2 values.

9.4 Acquisition campaign of year 2010 and experimental results

The results obtained by applying the WiFi-based passive ISAR processing described in Section 9.2 to the live passive data recorded during the experimental campaign described in Section 9.1 are here reported, to demonstrate the effectiveness of the proposed processing scheme.

As stated above the cancellation of the clutter background is mandatory for the successful formation of cross-range profiles, suitable for example for the ATR (Automatic Target Recognition) procedures which are usually fed with ISAR products. To further highlight and clearly demonstrate this point, Figure 9.6 shows the entropy as a function of the α_2 parameter for both the non-canceled and canceled signal for test M2, a quasi-monostatic acquisition with two identical vehicular targets moving with v_x about 4.5 m/s and maintaining a fixed displacement (about 2-3 m). Specifically Figure 9.6(a) refers to the first phase of the autofocus where $\hat{\alpha}_2^{(in)}$ is searched while Figure 9.6(b) refers to the second phase where the raw estimate is refined and the final estimated value $\hat{\alpha}_2$ is obtained jointly with the cubic coefficient. The used CPI is set to 6 sec. Similar results could be shown also for all the other experiments. As it is evident from Figure 9.6, the behavior observed in presence of a fictitious target injected in the real environment is confirmed also in presence of real targets. Specifically the reliable estimation of the Doppler chirp rate is unfeasible unless a cancellation stage is applied: the removal of the background contribution allows the ISAR processing to effectively work. In fact, it brings the useful signal (that originally was well below the disturbance level) in a medium/high signal to disturbance power ratio condition, which is the usual operative condition in ISAR imaging. If the processing is applied against the canceled signal, $\hat{\alpha}_2^{(in)} = 0.3770$ m/s^2 is obtained with the first estimate and finally $\hat{\alpha}_2 = 0.3926$ m/s^2 is obtained from the refining parameter estimation step. Notice that such value of α_2 is well in

line with the considered test geometry (nominal target velocity of 4.5 m/s and range of 50 m, yielding a nominal α_2 equal to 0.4). When the cancellation is not applied we get $\hat{\alpha}_2^{(in)} = 0.3366$ m/s^2 and as evident from Figure 9.6(b) the refinement does not produce any consistent estimated value.

The corresponding cross-range profiles are reported in Figure 9.7(a) showing the profile from canceled data (red plot), from not canceled data (black curve, the $\hat{\alpha}_2^{(in)}$ has been used for focusing) and from not canceled data using the motion parameters as estimated from canceled data (magenta curve). Figure 9.7(b) shows a zoom of the profile concerning the canceled signal. The cross-range axis has been scaled according to the procedure explained in Section 9.2.

As is apparent, by using a proper cancellation strategy (red curves) two similar patterns of scatters are clearly visible from the cross-range profiles, that correspond to the main scattering centers of the two identical cars used for the considered experiment. In contrast, when the ISAR processing is applied directly to the non-canceled surveillance signal (black and magenta curves) a large loss in signal to background power ratio is experienced. Notice that a significant degradation of the obtained profiles is observed even if the motion is estimated from the canceled signal (namely the magenta curve has been obtained by using the same target motion parameters of the red one). This is clearly due to the presence of the strong echoes from the stationary background. These are not added coherently as the echoes from the moving targets, but have still a very high value that masks the moving targets echoes. Looking in detail to the cross-range profile obtained after clutter cancellation, Figure 9.7(b), it can be observed that each of the two identical patterns in the reported cross-range profile is characterized by three main peaks (labeled with capital letters) which correspond to the main scattering centers of the two identical cars used for the considered experiment. Thus the proposed technique allows both to separate the two vehicles in the cross-range direction and to identify their main scattering points making it possible to measure their size and

displacement.

For example, by evaluating the distances between homologous points of the cars (profile peaks), it can be possible to estimate the cross-range displacement of the two targets. Notice that quite similar values are obtained for the three couples of peaks ($D_A = |A' - A| = 6.52$ m, $D_B = |B' - B| = 6.53$ m and $D_C = |C' - C| = 6.7$ m) which are well in line with the test geometry (it is here recalled that the length of each car is 4 meter and their separation along the path is about 2-3 m). This is a very good result especially considering that for the selected imaging time used for Figure 9.6 and Figure 9.7 the target Doppler spectrum was completely embedded in the clutter spectrum.

To highlight the reliability of the cross-range profiles obtained by applying the proposed ISAR technique, Figures 9.8, 9.9 and 9.10 show the sequence of nine profiles focused from subsequent (partially overlapped) frames extracted from the signal of test M2. A CPI of 6 seconds is used, sliding along the 10 seconds of the globally available acquisition time. The different frames refer to image time spanning from 3 seconds to 7 seconds with spacing 0.5 seconds. Initially, only a single car is present inside the antenna beam, which is clearly apparent from the profile. It can be easily observed, that as the second car enters in the antenna beam two almost identical cross-range profiles are obtained (see frames 1-3 in Figure 9.8). These profiles persist in all the considered frames occupying progressively increasing cross-range positions (according to test M2, the cars are moving along the x axis with positive velocity), as it clearly appear from frames 4-9 in Figures 9.9-9.10.

By measuring the cross-range distance traveled by scatter A between the first frame (image time 3 sec) and the last frame (image time 7 sec), a displacement of 17.81 m is obtained which is well in line with cross-range velocity of about 4.5 m/s and temporal separation between the first and the last frame of 4 seconds.

The high potential of the proposed WiFi-based passive ISAR for classification purposes is also confirmed by comparing results from test M2 to test M1 and B2 to B1. Specifically Figure 9.11 compares

the Doppler profiles obtained from experiment M1 (single vehicular target - red line) and M2 (two identical vehicular targets - black line). In the two experiments the targets were moving at almost the same speed and for profiles formation a CPI set to 6 sec was used properly selected from the overall available slow time interval to assure almost the same Doppler centroid for the first car. From the figure, it can be observes that red and black lines largely overlap, namely almost the same pattern of dominant scatterers is obtained even if different experiments are considered. The reliability of the obtained profiles is further confirmed also by the results in Figure 9.12 showing the same kind of comparison for the case of bistatic acquisitions.

The stability of the achieved profiles shows the effectiveness of the proposed experimental setup and processing scheme and supports the practical application of the WiFi-based passive ISAR for target discrimination and automatic recognition in short range surveillance applications.

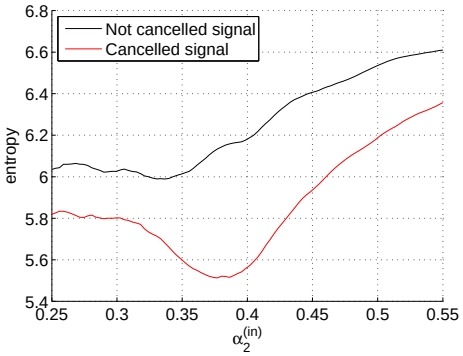

(a)

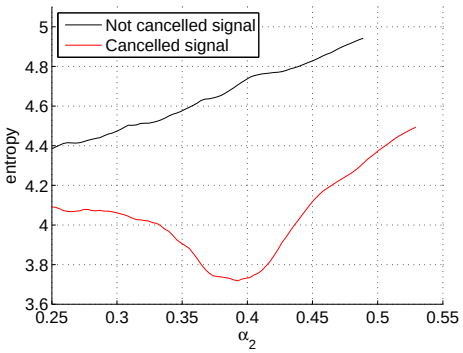

(b)

Figure 9.6: Entropy cost function versus α_2 parameter: comparison between not canceled and canceled signal: (a) first phase of estimation; (b) second phase of estimation.

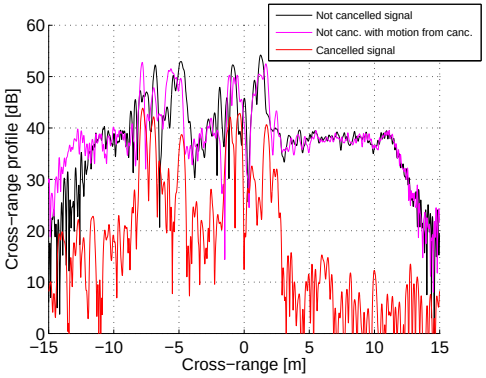

(a)

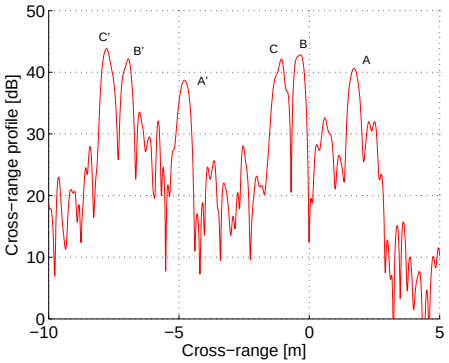

(b)

Figure 9.7: Cross-range profiles for the dataset of Figure 9.6: (a) comparison between canceled and not canceled signal; (b) zoom on canceled case.

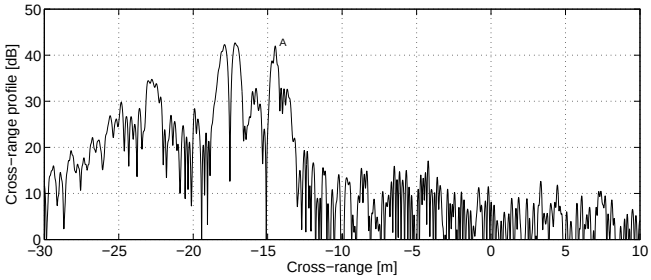

(a)

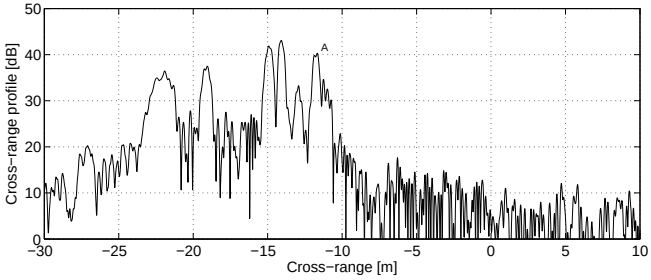

(b)

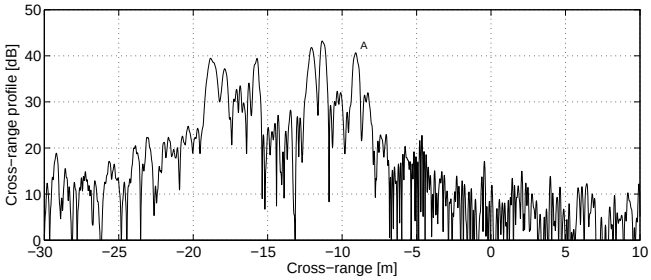

(c)

Figure 9.8: Sequence of frames from test M2 (1-3).

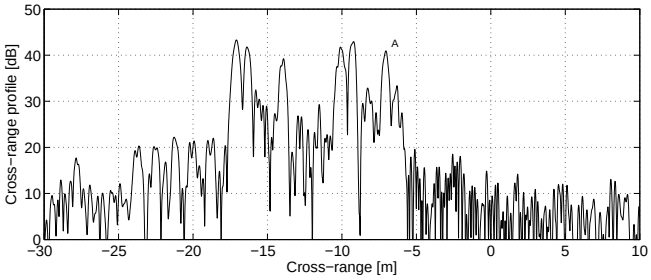

(a)

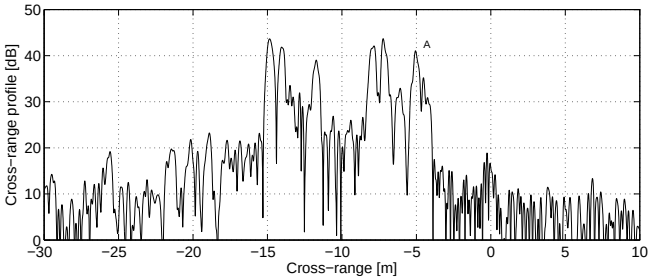

(b)

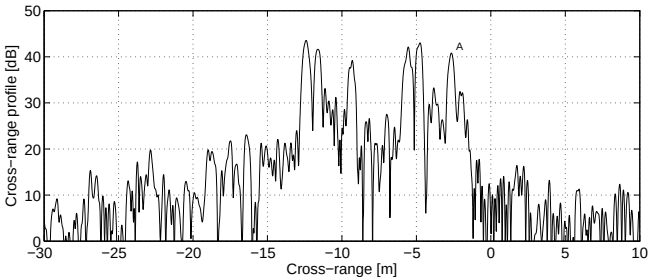

(c)

Figure 9.9: Sequence of frames from test M2 (4-6).

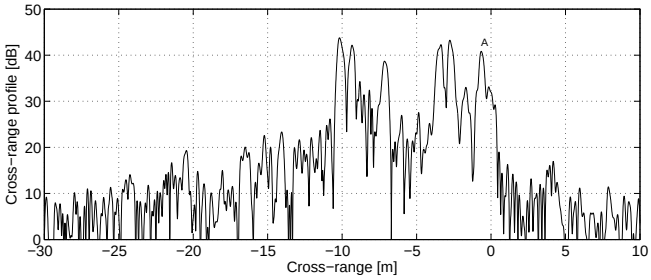

(a)

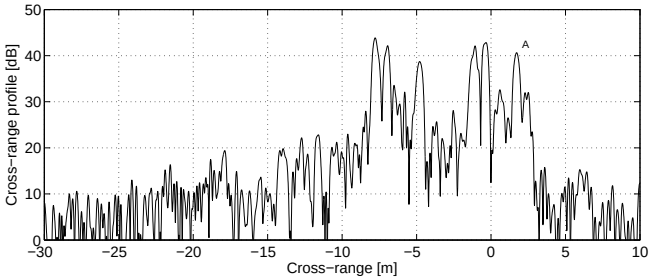

(b)

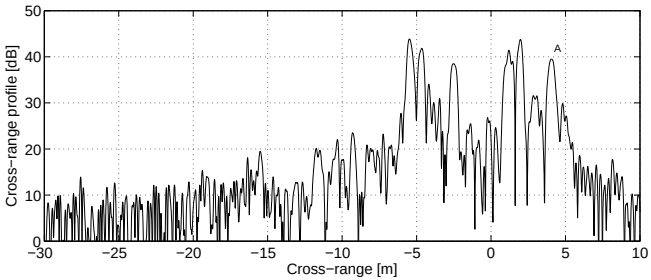

(c)

Figure 9.10: Sequence of frames from test M2 (7-9).

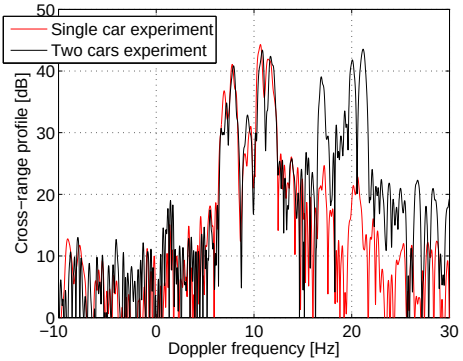

Figure 9.11: Profiles comparison between test M1 (single car) and test M2 (two cars).

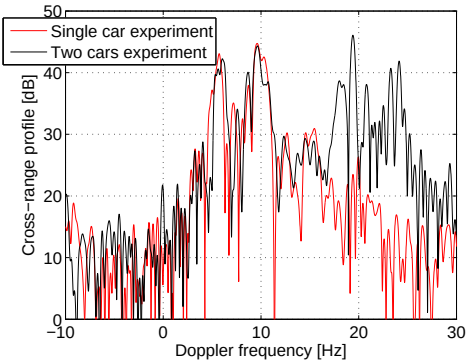

Figure 9.12: Profiles comparison between test B1 (single car) and test B2 (two cars).

Chapter 10

The ATOM project

The ATOM (Airport detection and Tracking Of dangerous Materials by passive and active sensors arrays) project has been funded by the European Commission under the Seventh Framework Programme[1].

The objective of the ATOM project is to study, design and develop the functional prototype of an innovative multi-sensor based system integrating active and passive radar sensors, improving the security level also in the Terminal area of the airport. ATOM system will be a non-intrusive but pervasive security system. It wont require ad-hoc check points for passengers implying two important consequences:

1. ATOM system will not interfere with normal passengers flow;

2. ATOM system will make more difficult for ill-intentioned people to identify where sensors are placed and to cheat controls. The pervasiveness of ATOM systems derives from the capability of ATOM sub-systems of monitoring wide airport areas and of detecting many kinds of hidden hazardous objects.

[1] Theme #7 Transport (including Aeronautics) - Grant agreement no.: 218041

The technical approach to be followed foresees two separate and integrated controls: one at the Terminal accesses equipped with innovative active devices, able to detect and identify dangerous concealed tools; the other in the airport halls before the gate area equipped with new passive RF sensors able to track suspicious people/containers. The integrated controls information will be managed in a secure way within the airport information networks allowing security operators to face threats in the most suitable way, minimizing the risk for other people inside the Terminal area.

The consortium of 11 European partners (including research centers and universities) consists of:

1. SESM (a Finmeccanica Company) - Italy;
2. Università degli Studi di Roma "La Sapienza" - DIET - Italy;
3. Thales Nederland B.V. - TNL - Netherlands;
4. Hellenic Aerospace Industry S.A. - HAI - Greece;
5. Fraunhofer - FHR and FKIE - Germany;
6. Technische Universiteit Delft TUD - Netherlands;
7. Slot Consulting Ltd - Hungary;
8. Ayco Internet S.L. - Spain;
9. Link srl - Italy;
10. Transylvania Tirgu-Mures Airport - Romania;
11. Schiphol Nederland B.V. - Netherlands.

This chapter is intended to give first a brief overview of the ATOM system concept (Section 10.1). Then, in Section 10.2, the results of the demonstration for the WiFi-based passive radar are discussed with reference to the conceived indoor application with human targets. Notice that, such results have been obtained as a direct outcome of the scientific achievements discussed in the previous Chapters.

10.1 Objectives of ATOM

The ATOM project presents an innovative approach to the challenging tasks required by the airport security system, that include: (i) increasing the screening quality; (ii) reducing the passengers screening time; (iii) providing privacy and security perception. The global system being investigated includes ([15]):

- Detection and identification of prohibited items (guns, knifes, weapons, explosives, etc.) concealed under clothes or inside bags, without interfering with the passengers flows;
- Tracking of the movements of the passengers carrying prohibited items; and
- Data management and distribution to handle the information flows and enable tracking of designated people, providing real time feedback to security personnel.

The approach foresees two sensors systems. The first sensors system is required to detect and identify prohibited items, reducing at the minimum the actions required to the passengers and the impact on their flow. It includes advanced mmW sensors and ultra-wideband sensors (whose feasibility has been investigated by FHR and TUD, respectively), and is located around each terminal entrance to detect potential terrorists. The second sensors system is required to localize suspicious people (namely people that have been detected to potentially carry an illicit item), without interfering with passengers transit and with other airport systems. In particular, the localization stage might be performed with active radar (developed by TNL) and passive radar (developed by DIET). A subsequent tracking stage (carried out at FKIE) is required to automatically track people while security personnel reach them.

A security distribution network, is required to integrate the data provided by the sensors systems, and present it to security operators. This approach removes the need of a unique point for the screening,

namely the checkpoint that separates the public area from the sterile area. This typically forces people to queue at the checkpoint to be screened and has a strong impact on the people flow. In addition, it provides no control of the public area that remains unprotected from potential terrorist attacks. The ATOM system starts the screening process much before the passengers enter the gate area, by means of a distributed detection sensors system. While impossible to have security personnel at each entrance, the tracking system allows to follow the movement of the suspicious passenger till the security people reaches him/her (see the pictorial view in Figure 10.1).

As apparent, the system requires the people tracking as an important element, which allows to distribute the detection sensors at each entrance without largely increasing the screening personnel. While also active mmW radar sensors can be used, the WiFi-based PBR is an important element of the tracking system. This exploits the many WiFi routers typically available in airport areas as the transmitters of opportunity, while requires the displacement of a set of receivers around the areas to be covered with the tracking service. Among the very nice feature of this approach is that no extra signal is transmitted, which makes the sensor totally free from any issue related to human health, plus it does operate in a totally covert mode, so that the potential terrorist has no possibility to detect that he/she is being tracked. The most important demonstration results of the WiFi-based PBR are reported in the next Section.

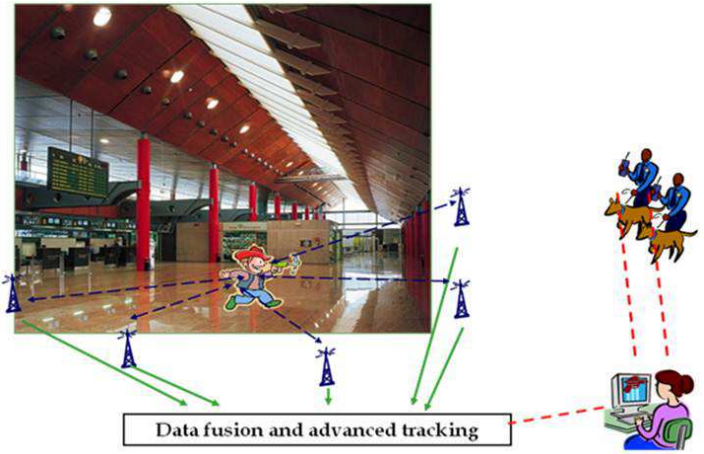

Figure 10.1: Sketch of the ATOM system concept.

10.2 Localization of human targets in indoor environments

The results of the demonstration for the passive radar system of ATOM, are reported in this Section. Specifically, sub-section 10.2.1 reports the description of the indoor Scenario used to perform the experiments, sub-section 10.2.2 describes the data processing stages require to take the radar measurements and perform localization for the specific case of human targets and, finally, sub-section 10.2.3 discusses the demonstration results.

10.2.1 Scenario

The indoor scenario chosen for the demonstration of the ATOM passive radar is shown in Figure 10.2. It consists of a wide exhibition hall - whose sizes are comparable with the ATOM scenario defined within WP2 - of the "Nuova Fiera di Roma" (Rome). Particularly, the sizes of the exhibition hall are approximately 77 meters of width and 120 meters of length. Figure 10.2(b) also shows the location selected for the transmitter of opportunity. It is assumed that the coordinates of such location are (0, 0) m.

The antennas dislocation is the same of the outdoor case discussed in Chapter 8. In particular, three receiving sensors (RX) were used to perform the experiments. Two receiving antennas, RX 2 and RX 3, were placed a few tens of centimeters below the TX, both in a quasi monostatic configuration with the transmitter of opportunity (see Figure 10.3(a)). Moreover, the relative distance between RX 2 and RX 3 was set in order to enable targets DoA estimation by exploiting an interferometric approach. Finally, receiver RX 1 was located in a bistatic configuration with respect to TX (see Figure 10.3(b)). The baseline was set to 25 m so that RX 1 is located at (25, 0) m.

Once the signals are collected, they have to be properly processed in order to make the passive radar prototype properly working. The

required data processing stages are described in the following subsection.

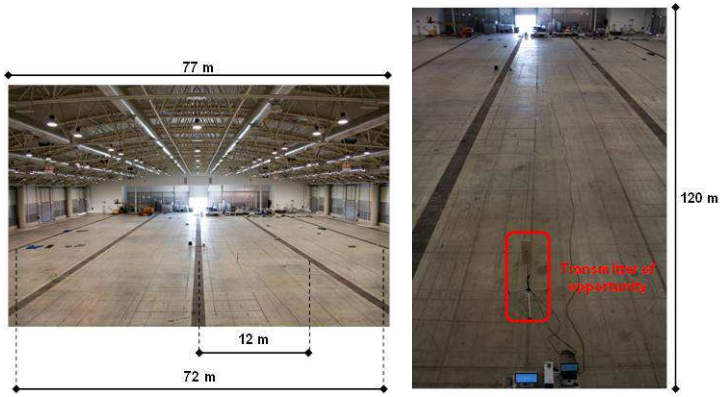

(a) (b)

Figure 10.2: Indoor scenario for the passive radar demonstration.

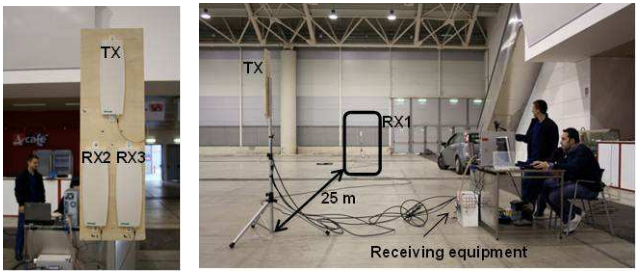

(a) (b)

Figure 10.3: Antennas configuration for the indoor passive radar demonstration.

10.2.2 Data processing stages

This subsection describes the data processing stages required to make the WiFi-based passive radar prototype properly working in the previously discussed Scenario. It is organized in: detections collection, detections selections and localization.

Detections collection

As previously mentioned, signals from three different surveillance antennas are collected by means of the experimental setup sketched in Figure 8.1. Then, the WiFi-based passive radar processing scheme depicted in Figure 5.4 is applied against the collected surveillance signal separately at each receiving channel. In particular:

i the proposed side-lobes reduction techniques are applied in order to guarantee an acceptable useful dynamic range;

ii the disturbance removal step is performed by adopting the Extensive Cancellation Algorithm (ECA) described in Chapter 5 with a batch duration equal to 100 ms over a range of 300 m;

iii a coherent integration time of 0.5 s is used to evaluate the two-dimensional range/Doppler frequency map over consecutive portions of the acquired signals (frames) with a fixed displacement of 0.1 s (10 frames per second are thus obtained); and

iv target detection is performed by resorting to a simple adaptive detector based on the cell-average CFAR (a cross-shape for the distribution of the reference cells was chosen with a total number of reference cells per frame set to 45,080 and the probability of false alarm was set to 10^{-4}).

Since the particular antennas geometry, the detections performed over the first receiving channel (the bistatic receiver, RX 1) allow to collect a set of bistatic range and Doppler frequency measurements (namely, R_{B1} and f_{D1}) for the considered target.

On the other side, a two-out-of-two detection criterion can be adopted for the second and the third receiving channels (RX 2 and RX 3, both in a quasi monostatic configuration with respect to TX) which allows to collect a second set of range and Doppler frequency measurements (namely, R_{B2} and f_{D2}) while reducing the probability of false alarm. Moreover, the phase difference between RX 2 and RX 3 measured at the target detection point is exploited to obtain the target DoA estimation. Notice that the DoA estimation will be provided with reference to the TX antenna boresight which is steered along the y axes.

As an example, the simple human target detection experiment sketched in Figure 10.4 is considered. In particular, the test was performed in the indoor scenario with a man moving toward the transmitter of opportunity location with constant velocity and angle of arrival approximately equal to zero degrees.

From Figure 10.5, it clearly appears that different kinds of detections are performed that might be mainly organized as follows:

- false alarms - False alarms might be easily discarded by a tracking algorithm. Moreover, from a direct visual comparison between the range/Doppler frequency planes shown in Figure 10.5, it is apparent that the number of false alarms is significantly reduced by the adoption of the two-out-of-two detection criterion performed for the receiving channels RX 2 and RX 3;

- Doppler ambiguities - Doppler frequency ambiguities are due to the WiFi pulses repetition period that is equivalent to radar pulse repetition time. Such detections might be easily discarded by a tracking algorithm;

- detections which are likely to correspond to target returns - Such detections (highlighted within the blue box in Figure 10.5) appear at positive Doppler frequency locations (that is in line with the test geometry, since the target moves toward the antennas location) and decreasing bistatic range. However, as it will be clarified in the following, it clearly appears that

the human target has a wide Doppler spectrum mainly due to different relative velocity of different parts of the human body (above all, torso, head, arms, upper and lower legs and feet); and

- multipath effects - Multipath effects might be caused by reflections of the target echo over either the walls or the top of the building.

The following subsection focuses on the processing stages required to select the detections corresponding to the target's torso. The measurements related to such kind of detections will be then used to localize and track the target.

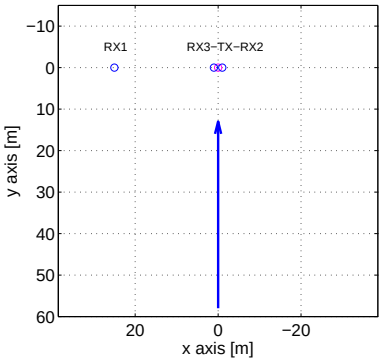

Figure 10.4: Target detection experiment.

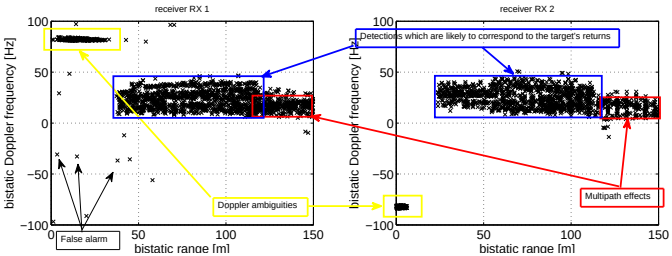

Figure 10.5: Detections over the range/Doppler frequency bistatic planes for a simple human target detection experiment.

Detection selection

It has been previously shown that a wide Doppler spectrum is experienced in the case of human targets detection experiments. In fact, different parts of the human body (above all, torso, head, arms, upper and lower legs and feet) move with different velocities which results in a row of Doppler side-peaks around the main target detection point. In particular, while the target moves, the echo from its torso should appear at a quite stable Doppler frequency location. In contrast, since arms, legs and feet move with variable velocity, the corresponding returns show a fast-varying Doppler effect.

It has to be noticed that the analysis of the complex human target's Doppler frequency structure, might be useful if target recognition procedures are enabled. In fact, the Doppler side-peaks arising from movement of arms, legs and feet represent the human target's signature.

However, for the purpose of the analysis here reported (target detection and localization), the Doppler frequency side-peaks might prevent the correctness of the detection algorithm and thus reduce the localization accuracy. In order to avoid such effects, the Doppler side-peaks have to be automatically identified and discarded. To accomplish with this result, a simple linear filtering strategy (based on the Kalman's algorithm) is considered as follows:

- the plots (range/Doppler/DoA measures) collected at the generic time-step are used to predict the subsequent system state;
- at the next time-step, among all the available plots suitable for association, the closest one to the prediction is selected and the algorithm is reiterated.

This really allows to discard the Doppler side-peaks which - being related to parts of human body whose velocity changes fast - are characterized by a fast-varying Doppler effect.

As an example, Figure 10.7 shows with the green circle markers the selected plots for the target detection experiment whose growth

truth is reported again in Figure 10.6. As is apparent, the selected plots show a quite stable Doppler frequency state without interfering with the Doppler side-peaks.

The selected plots provide the target bistatic range and Doppler frequency measurements reported, respectively, in Figure 10.8(a) and Figure 10.8(b) (blue curve for the bistatic receiver RX 1 and red curve for the quasi monostatic receiver RX 2).

As is apparent, the collected measures are well in line with the test geometry (see Figure 10.6). In fact, while the target moves, both the bistatic range measures decrease with the bistatic range of RX 1 decreasing faster. Similarly, when the target is far from the antennas location, the measured Doppler frequencies are almost the same. In contrast, when the target is going to approach the transmitter location, the Doppler frequency measured by RX 1 decreases faster.

Moreover, the phase-difference between RX 2 and RX 3 at the target detection point can be used to estimate the target's echo DoA. The result is shown in Figure 10.8(c).

As is apparent, the estimated DoA is approximately equal to zero, well in line with the test geometry (see Figure 10.6).

Once the range/Doppler frequency/DoA measures are collected, target localization might be performed along the line suggested in the following sub-section. Notice that, within the ATOM project, the collected measures for the experiments described in sub-section 10.2.3 are provided to the sub-sequent tracking system of ATOM (WP 7 by FKIE Institute of Bonn - Germany).

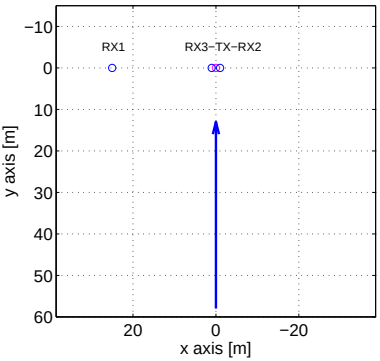

Figure 10.6: Target detection experiment.

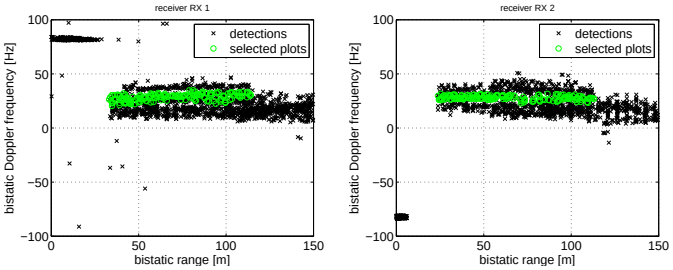

Figure 10.7: Selected plots over the range/Doppler frequency bistatic planes for a simple human target detection experiment.

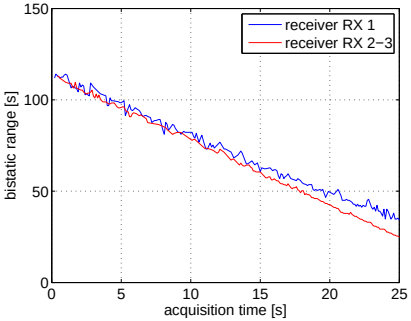

(a) Bistatic range measures

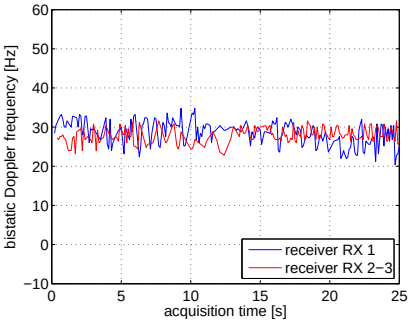

(b) Bistatic Doppler frequency measures

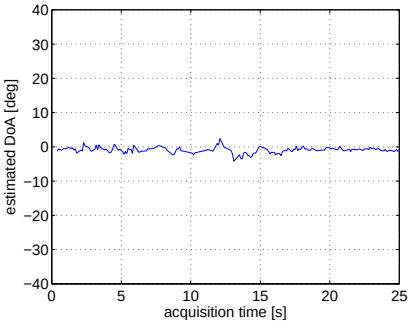

(c) Angle of arrival of the target's echo

Figure 10.8: Passive radar measurements for a simple human target detection experiment.

Target localization

The localization results for the human target detection experiment depicted in Figure 10.6 are reported in the following. In particular, a first localization (before the ATOM tracking sub-system) might be performed by using the range and DoA measures along the line suggested in Chapter 8. The localization result is reported in Figure 10.9 while the sketch of the experimental test is replied in Figure 10.9(a) for a direct fair comparison.

As is apparent from Figure 10.9, the obtained sequence of localizations nicely match with the test geometry with only small deviations which are mainly due to the range/DoA estimation accuracies. Notice that improved localization performance are expected after the exploitation of the sub-sequent tracking system of ATOM (WP 7 - FKIE).

However, the neat result obtained shows that indeed the approach is promising and can provide localization of human targets. In the following sub-section, aiming at demonstrating the capabilities of the WiFi-based passive radar for surveillance in wide indoor areas, as the airport's terminals, further results are presented related to experimental tests performed in the indoor scenario with one or two human targets simultaneously.

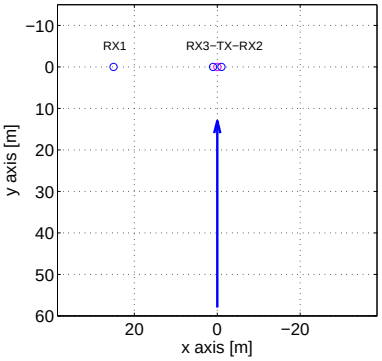

(a)

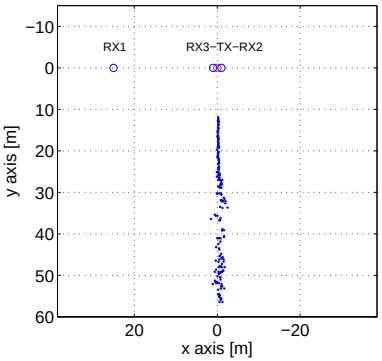

(b)

Figure 10.9: Example of localization of a single human target in indoor environments: (a) ground truth; (b) localization results.

Increased discrimination capability via Doppler processing

As it has been discussed Chapter 2, the resolution capabilities of the conceived WiFi-based passive radar along the range and Doppler frequency dimensions depend on, respectively, the bandwidth of the signal of opportunity and the coherent integration time. However, while in the first case the signal of opportunity's bandwidth is strictly non-adjustable, the Doppler frequency resolution can be increased by choosing a longer coherent integration time. This might allow to discriminate between targets at the same range location whether they relative velocity implies enough separation along the Doppler frequency dimension.

As an example, the experiment depicted in Figure 10.10 has been performed with two human targets moving along the blue and red paths. For this particular geometry, since they moved along different directions, their relative velocities are different. As a consequence, their Doppler frequency separation is wide enough to allow the WiFi-based passive radar to correctly distinguish among them.

This is clearly shown in Figure 10.11 that reports the overlap between the performed detections and the selected ones for the considered experiment. The target moving away from the antennas location (the blue one in Figure 10.10) obviously appears at negative Doppler frequency locations. On the contrary, the blue one - which is moving toward the antennas location - appears at positive Doppler frequency locations.

As is apparent, the relative Doppler frequency separation among the targets allow the WiFi-based passive radar to correctly resolve the targets and detect both of them. Once the targets are detected their range/Doppler/echo's angle of arrival can be correctly estimated and used to localize both of them. In the following, some experimental results will be shown with the aim of proving the benefits deriving from the exploitation of the Doppler frequency resolution capabilities of the conceived WiFi-based passive radar.

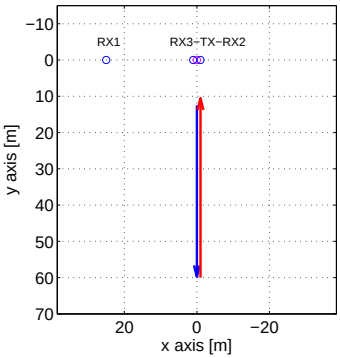

Figure 10.10: Experiment to demonstrate the Doppler frequency discrimination capabilities.

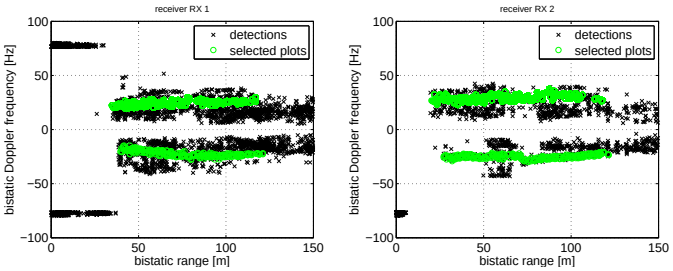

Figure 10.11: Example of target discrimination allowed by the Doppler resolution.

10.2.3 Experimental results

This sub-section reports the results for the passive radar demonstration of ATOM.

The results of a preliminary test are firstly discussed with the aim of validating the localization performance of the conceived WiFi-based passive radar. In particular, a direct comparison between the localization provided by the WiFi-based passive radar and the ground truth collected with a GPS receiver will be shown.

After that, different experimental results will be proposed which have been performed with human targets in the indoor Scenario previously described.

Validation of the WiFi-based passive radar localization performance

This sub-section reports the results of a preliminary experiment performed with the aim of validating the localization performance of the conceived WiFi-based passive radar.

The experimental test has been performed on the roof of the Faculty of Engineering - University of Rome "La Sapienza" (see Figure 10.12). A man moved on the roof bringing with him a GPS receiver which has been connected to the Internet in order to download real time Local Area Differential GPS (LADGPS) corrections to be exploited to improve the GPS positioning accuracy. Particularly, the data provided by the GPS permanent station M0SE - owned by University of Rome "La Sapienza" and located as shown in Figure 10.12 - have been exploited to collect the ground truth with approximately a few centimeters of accuracy. Once the GPS data are collected, the ground truth can be drawn over the picture representing the faculty's roof (see the sequence of the green markers in Figure 10.12). As is apparent, the man moved along a path of about 50 m making also different changes of walking direction.

The WiFi transmitter has been located at the point represented with the coordinates (0, 0) m. Moreover, two receiving antennas (RX

2 and RX 3) of the WiFi-based passive radar prototype have been located a few centimeters below the transmitter of opportunity, both in a quasi-mono-static configuration with the aim of collecting a set of range/Doppler/DoA measurements for the detected target. Once the measurements are collected, target localization can be performed along the way suggested in Chapter 8. The obtained result is thus reported in Figure 10.12 with the sequence of the blue markers.

As is apparent, the localization performed with the WiFi-based passive radar nicely meets the ground truth collected by means of the GPS receiver. This clearly appears along the linear paths as well as during the changes of the man's walking direction. The measured deviation between the ground truth and the radar localization is below 0.5 m thus validating the localization performance of the conceived WiFi-based passive radar.

Once assessed the performance of the WiFi-based passive radar in terms of localization, it does make sense to perform experiments with the aim of simulating the passengers behavior in the indoor scenario. The results of such experiments will be discussed in the following.

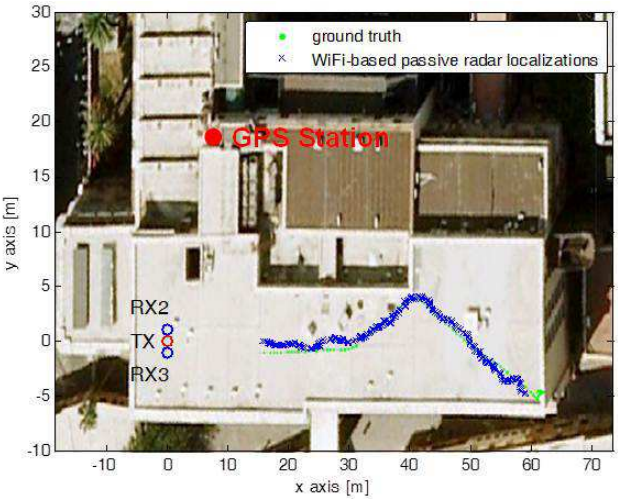

Figure 10.12: Localization performance assessment.

First indoor experiment

The first indoor experiment has been performed with a single human target. The aim of the test was to validate the possibility of estimating the target echo's angle of arrival in indoor environments.

The human target started moving forward the antennas location from point (0, 10) m. Once he arrived approximately at point (0, 30) m, he changed his walking direction by turning on his right (see Figure 10.13(a) and Figure 10.13(b) which reports a screenshot of the experiment's video).

The obtained sequence of localizations nicely match the test's ground truth (as it is reported in Figure 10.13(c)) showing that localization of a human target moving in indoor environments is possible with good accuracy. Moreover, Figure 10.14 reports the estimated target's echo DoA for the considered experiment. Notice that, since the target moves toward positive x coordinate locations, its echo's angle of arrival becomes positive.

The neat result reported in Figure 10.14 shows that the estimation of human target's echo DoA is possible in indoor environments with reasonably accuracy. Thus, in the following, experimental results related to tests performed with two targets will be shown.

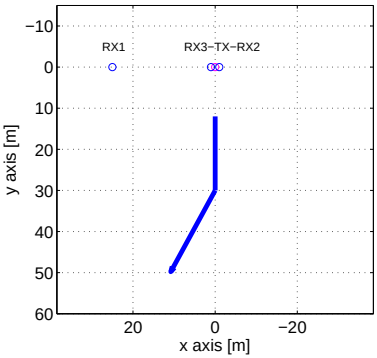

(a)

(b)

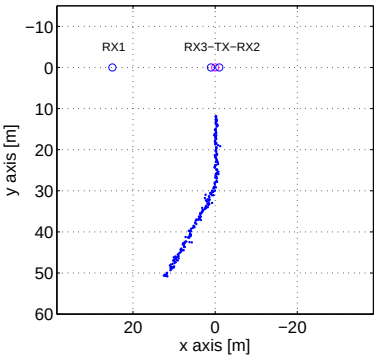

(c)

Figure 10.13: First indoor demonstration: (a) ground truth; (b) screenshot of the experiment's video; (c) sequence of localizations.

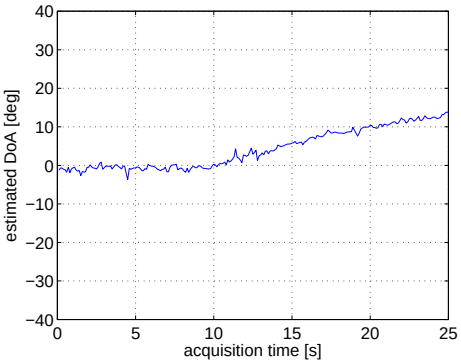

Figure 10.14: Estimated target echos angle of arrival for the first indoor test.

Second indoor experiment

The second indoor experiment has been performed with two human targets. In this case, the targets moved in front of the transmitter of opportunity approaching each other, as depicted in Figure 10.15(a). When they were very close each-other, they simulated a suspect behavior by passing a bag between them (see Figure 10.15(b) which reports a screenshot of the experiment's movie).

The sequence of localizations obtained by means of the passive radar prototype is reported in Figure 10.15(c). As is apparent, not only both the targets are correctly detected and localized, but also their suspect behavior could be taken by the obtained sequence of localizations. In fact, Figure 10.15(c) clearly shows that the targets' tracks became very close each other when they reach approximately the same location.

The result reported in Figure 10.15(c) shows that it possible to resolve and correctly localize targets by exploiting the Doppler frequency resolution capabilities of the conceived WiFi-based passive radar as previously discussed.

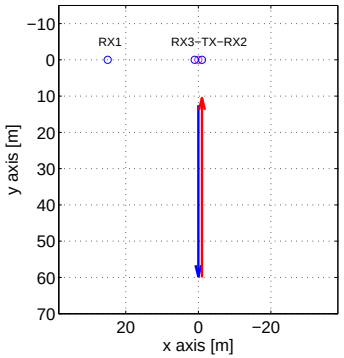

(a)

(b)

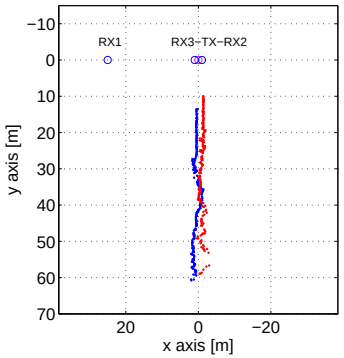

(c)

Figure 10.15: Second indoor demonstration: (a) ground truth; (b) screenshot of the experiment's video; (c) sequence of localizations.

Third indoor experiment

The third indoor experiment has been performed with two human targets. The first of them moved forwarding the antennas location in front of the transmitter of opportunity for a while till he changed his walking direction by turning on his right. The second target started moving approximately from point (0, 60) m approaching the transmitter of opportunity. The test is depicted in Figure 10.16(a) and in Figure 10.16(b) which reports a screenshot of the experiment's video.

Figure 10.16(c) shows the obtained sequence of localizations for the considered experiment. As is apparent, the obtained result is nicely in line with the test geometry. Moreover, the results reported in Figure 10.16(c) show that it is possible to localize targets moving along different paths in indoor environments even if they pass very close each other.

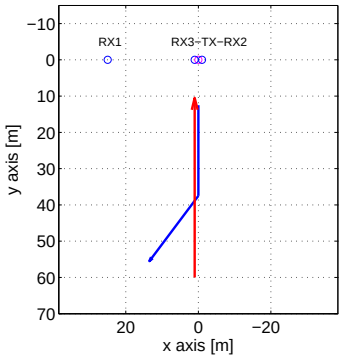

(a)

(b)

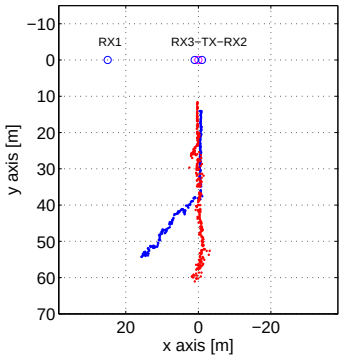

(c)

Figure 10.16: Third indoor demonstration: (a) ground truth; (b) screenshot of the experiment's video; (c) sequence of localizations.

Fourth indoor experiment

The fourth indoor experiment has been performed with two human targets moving along different paths and making changes of walking direction with different angles (see Figure 10.17(a)). In this case, the turning angle of the target moving away from the transmitter of opportunity is greater than that of the target moving toward the transmitter of opportunity.

Figure 10.17(d) reports the obtained sequence of localizations. As is apparent, the obtained targets' tracks very nicely meet the test's ground truth by remarking the different turning angles marked by the targets.

Notice that, the different turning angles of the targets are clearly apparent from Figure 10.17(b) and Figure 10.17(c). In particular, Figure 10.17(b) reports a screenshot of the experiment's video taken approximately when the targets started to turn on their own right. It clearly appears that for the target on the left of the figure, the turning angle is greater than that of the target on the right. Notice also that the target started to turn when they were approximately on the black line on the floor. Moreover, Figure 10.17(c) reports a screenshot of the experiment's video taken approximately at the end of the acquisition. As is apparent, the target on the left has reached the next black line on the floor (x displacement of about 12 m as shown in Figure 10.17(b)) while the target on the right is still in the middle of the two black lines.

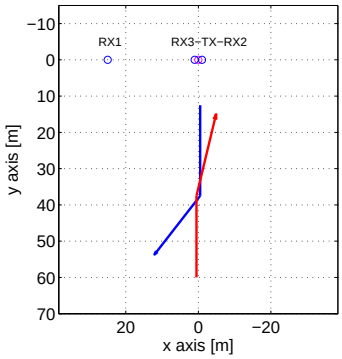

(a)

(b)

(c)

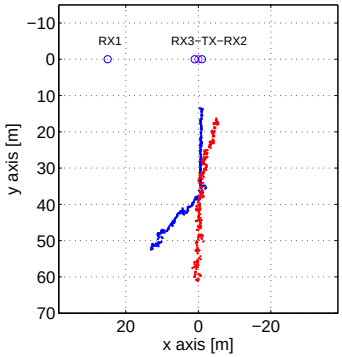

(d)

Figure 10.17: Fourth indoor demonstration: (a) ground truth; (b)-(c) screenshots of the experiment's video; (d) sequence of localizations.

Fifth indoor experiment

The fifth indoor experiment has been performed with two human targets. They started walking very close each other approximately from point (8, 60) m. When they reached point (0, 40) m, both of them changed their walking direction. In particular, as it is depicted in Figure 10.18(a), the first of them moved toward the transmitter of opportunity, while the latter moved along the opposite direction. This is also shown in Figure 10.18(b) that reports a screenshot of the experiment's video taken a few seconds after one of the targets changed his walking direction.

The sequence of the obtained localizations for the considered test is shown in Figure 10.18(c). As is apparent, till the targets moved very close each other, just a single target has been detected and localized. In fact, in such case both the targets appear at the same range/Doppler frequency location thus preventing the possibility of resolving them. On the brightside, when they moved along different paths, they appeared at different Doppler frequency locations on both the bistatic range/Doppler frequency planes thus making it possible to resolve and localize both of them.

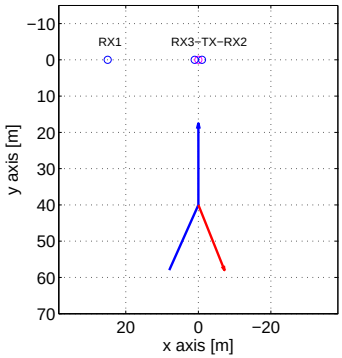

(a)

(b)

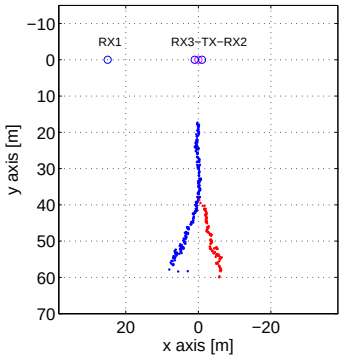

(c)

Figure 10.18: Fifth indoor demonstration: (a) ground truth; (b) screenshot of the experiment's video; (c) sequence of localizations.

Sixth indoor experiment

The sixth indoor experiment has been performed with two human targets. They started walking very close each other approximately from point (0, 15) m. When they reached approximately point (0, 38) m, one of them stopped his walking and then came back toward the transmitter of opportunity. This is depicted in Figure 10.19(a) and in the screenshot of the experiment's video shown in Figure 10.19(b).

The localization result for the considered test is shown in Figure 10.19(c). As is apparent, again, till the targets moved very close each other, it was not possible to resolve them. On the brightside, when the second target stopped and then came back, a new sequence of detections was selected on both the bistatic range/Doppler frequency planes thus making it possible to resolve the targets and localize both of them.

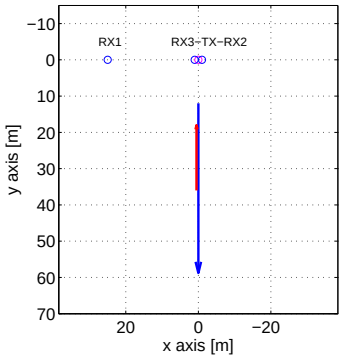

(a)

(b)

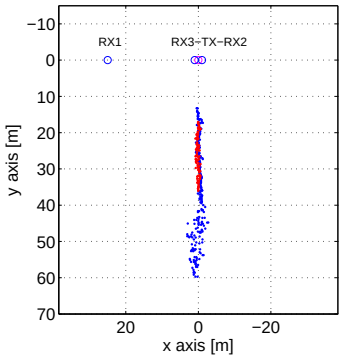

(c)

Figure 10.19: Sixth indoor demonstration: (a) ground truth; (b) screenshot of the experiment's video; (c) sequence of localizations.

Conclusions

The results reported in this work provide a demonstration of the wide potentialities of a WiFi-based passive radar. Despite further processing strategies are being designed to improve its performance and make it really operational, it is possible to identify a wide range of applications.

The possibility to provide passive radar surveillance by exploiting such a ubiquitous and easily accessible source of opportunity, offers major opportunities to improve interior and exterior security for all types of buildings and to identify and track goods and people. This type of passive sensing can be used in public areas such as railway station, airport terminals, and private commercial premises such as buildings office, warehouses, malls. This technique does not require co-operative targets as other wireless or RFID based detections system and it is less subject to the privacy issue of the video-cameras surveillance.

The outdoor applications are quite straightforward, especially for detecting and localizing vehicles and people getting close to specific (possibly critical) infrastructures to be protected. Approaching objects are clearly detected up to a few hundreds of meters and tracked in their movement using the techniques previously described. Moreover, Automatic Target Recognition procedures might be enabled considering that it is possible to realize high-resolution cross-range profiles of moving targets.

This can exploit WiFi routers already existing inside/outside the

infrastructures to be protected or routers added ad-hoc at limited costs.

Shorter range applications are typically considered for the indoor surveillance case. As a specific example of this type of application, the effectiveness of the WiFi-based passive radar sensor has been investigated as a part of the ATOM (Airport detection and Tracking Of dangerous Materials by passive and active sensors arrays) project funded by the European Commission under the 7th Framework Program for Aeronautics.

Publications, speeches and dissertations

International Journals Publications

3 Fabiola Colone, Debora Pastina, Paolo Falcone and Pierfrancesco Lombardo,
"WiFi-based passive ISAR for high resolution cross-range profiling of moving targets",
Submitted to the IEEE Transactions on Geoscience and Remote Sensing.

2 Paolo Falcone, Fabiola Colone, and Pierfrancesco Lombardo,
"Potentialities and Challenges of WiFi-Based Passive Radar",
IEEE Aerospace and Electronic Systems Magazine, November 2012 Issue.

1 Fabiola Colone, Paolo Falcone, Carlo Bongioanni, and Pierfrancesco Lombardo,
"WiFi-Based Passive Bistatic Radar: data processing schemes and experimental results",
IEEE Transactions on Aerospace and Electronic Systems, April 2012 Issue.

Conference Proceedings Publications

12 Paolo Falcone, Fabiola Colone, and Pierfrancesco Lombardo, "Localization of moving targets with a Passive Radar System based on WiFi transmissions", IET International Radar Conference 2012, Glasgow, UK, 22-25 October 2012.

11 Paolo Falcone, Carlo Bongioanni, Antonio Macera, Fabiola Colone, Debora Pastina, Pierfrancesco Lombardo, Enrico Anniballi, and Roberta Cardinali, "Active and Passive Radar Sensors for Airport Security", Tyrrhenian Workshop 2012 on Advances in Radar and Remote Sensing, Naples, Italy, 12-14 September 2012.

10 Paolo Falcone, Fabiola Colone, Antonio Macera, Debora Pastina, and Pierfrancesco Lombardo, "Advances in ISAR processing for high resolution cross-range profiling with passive radar", International Radar Symposium, IRS 2012, Warsaw, Poland, 21-26 May 2012.

9 Paolo Falcone, Fabiola Colone, Antonio Macera, and Pierfrancesco Lombardo, "Localization and tracking of moving targets with WiFi-based passive radar", IEEE Radar Conference, RADAR 2012, Atlanta, Georgia, USA, 7-11 May 2012.

8 Paolo Falcone, Fabiola Colone, Pierfrancesco Lombardo, and Debora Pastina, "WiFi-based passive ISAR for high resolution cross-range profiling of moving targets", 9th European Conference on Synthetic Aperture Radar, EUSAR 2012, Nuremberg, Germany, 23-26 April 2012.

7 Fabiola Colone, Paolo Falcone, and Pierfrancesco Lombardo, "Passive Bistatic Radar based on mixed DSSS and OFDM WiFi transmissions", European Radar Conference, EURAD 2011, Manchester, UK, 12-14 October 2011.

6 Fabiola Colone, Paolo Falcone, Antonio Macera, and Pierfrancesco Lombardo, "High Resolution Cross-Range Profiling with Passive Radar via ISAR processing", International Radar Symposium, IRS 2011, Leipzig, Germany, 7-9 September 2011.

5 Paolo Falcone, Fabiola Colone, and Pierfrancesco Lombardo, "Doppler Frequency Sidelobes Level Control for WiFi-Based Passive Bistatic Radar", 2011 IEEE International Radar Conference, Kansas City, Missouri (USA), 23-27 May 2011.

4 Fabiola Colone, Paolo Falcone, and Pierfrancesco Lombardo, "Ambiguity Function analysis of WiMAX transmissions for Passive Radar", 2010 IEEE International Radar Conference, Washington DC, USA, 10-14 May 2010.

3 Paolo Falcone, Fabiola Colone, Carlo Bongioanni, and Pierfrancesco Lombardo, "Experimental Results for OFDM WiFi-Based Passive Bistatic Radar", 2010 IEEE International Radar Conference, Washington DC, USA, 10-14 May 2010.

2 Diego Cristallini, Mauro Caruso, Paolo Falcone, Diego Langellotti, Carlo Bongioanni, Fabiola Colone, Stefano Scafè, and Pierfrancesco Lombardo, "Space-Based Passive Radar Enabled by the New Generation of Geostationary Broadcast Satellites",

IEEE Aerospace Conference, Big Sky, Montana, USA, 6-13 March 2010.

1 Paolo Falcone, Fabiola Colone, Pierfrancesco Lombardo, and Tullio Bucciarelli,
"Range sidelobes reduction filters for WiFi-Based Passive Bistatic Radar",
European Radar Conference, EURAD 2009, Rome, Italy, 30 September-2 October 2009.

Speeches at National & International Conferences

4 Paolo Falcone, Fabiola Colone, and Pierfrancesco Lombardo,
"Advanced signal processing for WiFi-Based Passive Bistatic Radar",
presentazione alla Riunione Annuale GTTI 2011, Messina, 20-22 Giugno 2011.

3 Fabiola Colone, Paolo Falcone, Carlo Bongioanni, and Pierfrancesco Lombardo,
"Advanced techniques for WiFi-Based Passive Bistatic Radar",
presentazione al 3rd PCL Focus Day, FHR Wachtberg (Germany), 3-4 May 2011.

2 Fabiola Colone, Paolo Falcone, Carlo Bongioanni, and Pierfrancesco Lombardo,
"WiFi-Based Passive Bistatic Radar for Local Area Surveillance",
presentazione al 2nd PCL Focus Day, FHR Wachtberg (Germany), 18 November 2009.

1 Fabiola Colone, Paolo Falcone, Pierfrancesco Lombardo, and Tullio Bucciarelli,

"Ambiguity Function Side-Lobes Reduction in WiFi-Based Passive Bistatic Radar",
presentazione alla Riunione Annuale GTTI 2009, Parma, 23-26 Giugno 2009.

ATOM Project's Technical Reports

3 Section 2.3 of Deliverable D9.1 of the "ATOM" (Airport detection and Tracking Of dangerous Materials by passive and active sensors arrays) project funded by the European Commission, 7th framework program, Theme #7 Transport (including Aeronautics), Grant agreement no.: 234014, "Integrated prototype of ATOM system", submitted to the European Commission in June 2012.

2 Deliverable D5.2 of the "ATOM" (Airport detection and Tracking Of dangerous Materials by passive and active sensors arrays) project funded by the European Commission, 7th framework program, Theme #7 Transport (including Aeronautics), Grant agreement no.: 234014, "System study of a passive radar network", submitted to the European Commission in November 2011.

1 Deliverable D5.1 of the "ATOM" (Airport detection and Tracking Of dangerous Materials by passive and active sensors arrays) project funded by the European Commission, 7th framework program, Theme #7 Transport (including Aeronautics), Grant agreement no.: 234014, "System design of a single passive radar sensor concept", submitted to the European Commission in May 2011.

Presentation of the research results during the ATOM Project's internal meetings

7 ATOM Final Workshop, Rome (Italy), June, 26 2012. Presentation of the most important research achievements obtained within the ATOM project to the Officer of the European Commission.

6 ATOM Validation day, Tirgu Mures (Romania), June, 7 2012. Presentation of the demonstration results to the ATOM's User Group. The capability of the conceived passive sensor to properly take the Range, Doppler frequency and echo's direction of arrival measures has been shown with reference to experimental tests performed in indoor environments. The localization capabilities of the WiFi-based passive radar have been shown as well.

5 5th ATOM internal meeting, Delft (The Netherlands), January, 27 2012. Investigation of the possibility of improving the resolution capabilities of the conceived passive radar through the analysis of the Doppler-rate response. Presentation of preliminary experimental results related to the Ambiguity Function evaluation and control.

4 4th ATOM internal meeting, Budapest (Hungary), June, 24 2011. Design of an optimization procedure able to find the sensors geometry which yields the best obtainable target localization accuracy. Presentation of a set of optimum sensor geometries that differ for the number of receiving sensors, the coverage level and the worst admissible localization accuracy.

3 3rd ATOM internal meeting, Vigo (Spain), January, 20 2011. Design of processing strategies able to control the peak-to-side lobes ratio in the Doppler frequency dimension of the WiFi signals Ambiguity Function. Design of a disturbance removal algorithm for cancellation of the undesired (direct signal from

the transmitter of opportunity, clutter and multi-path) contributions received by the passive sensor together with useful signals. Development of a software tool for simulation of the passive radar working within the ATOM scenarios. Characterization of the obtainable performance.

2 2nd ATOM internal meeting, Bonn (Germany), July, 7-8 2010. Analysis of the WiFi signals Ambiguity Function. Design of processing strategies able to effectively control the peak-to-side lobes ratio in the range dimension for differently modulated pulses.

1 1st ATOM internal meeting, Athens (Greece), January, 25-26 2010. Analysis of the electro-magnetic sources typically available in the public indoor area of an airport and selection of the most suitable for passive radar surveillance purposes.

Bibliography

[1] Special Issue on Passive Radar Systems, IEEE Proceedings on Radar, Sonar and Navigation,Vol. 152, Issue 3, June 2005, pp. 106-223.

[2] Special Issue on Passive Coherent Location, IEEE Aerospace and Electronic Systems Magazine, November 2012 Issue.

[3] ARGUS3D project, funded by the European Union, 7th framework programme, Theme #10 Security, Grant agreement no.: 218041. Website http://www.argus3d.eu

[4] IEEE Standard for Local and Metropolitan Area Network: "Part 16: Air Interface for Fixed and Mobile Broadband Wireless Access Systems" (IEEE Std 802.16^{TM}-2004) - and following Supplements and Amendments (IEEE Std 802.16e^{TM}-2005)

[5] IEEE Standard for Information technology: "Part 11: Wireless LAN Medium Access Control (MAC) and Physical Layer (PHY) specifications" (IEEE Std 802.11^{TM}-1999) - and following Supplements and Amendments (IEEE Stds 802.11a^{TM}-1999, 802.11b^{TM}-1999, 802.11b^{TM}-1999/Cor 1-2001, and 802.11g^{TM}-2003)

[6] M.I. Skolnik; , "Introduction to radar systems," p. 318, 3rd Ed. New York: Mc-Graw-Hill, 2000.

[7] Colone, F.; Woodbridge, K.; Guo, H.; Mason, D.; Baker, C.J.; , "Ambiguity Function Analysis of Wireless LAN Transmissions for Passive Radar," *Aerospace and Electronic Systems, IEEE Transactions on* , vol.47, no.1, pp.240-264, January 2011.

[8] Saini, R.; Cherniakov, M.; , "DTV signal ambiguity function analysis for radar application," *Radar, Sonar and Navigation, IEE Proceedings* - , vol.152, no.3, pp. 133- 142, 3 June 2005.

[9] Bicocchi, R.; Bucciarelli, T.; Melacci, P.T.; , "Radar sensitivity and resolution in presence of range sidelobe reducing networks designed using linear programming," *Radio and Electronic Engineer* , vol.54, no.6, pp.244-250, June 1984.

[10] M. Grant and S. Boyd. CVX: Matlab software for disciplined convex programming (web page and software). http://cvxr.com/cvx, December, 2009

[11] Colone, F.; O'Hagan, D.W.; Lombardo, P.; Baker, C.J.; , "A Multistage Processing Algorithm for Disturbance Removal and Target Detection in Passive Bistatic Radar," *Aerospace and Electronic Systems, IEEE Transactions on* , vol.45, no.2, pp.698-722, April 2009

[12] weblink: http://www.xilinx.com/ /support/documentation/boards_and_kits/ug230.pdf

[13] Li Xi; Liu Guosui; Jinlin Ni; , "Autofocusing of ISAR images based on entropy minimization," *Aerospace and Electronic Systems, IEEE Transactions on* , vol.35, no.4, pp.1240-1252, Oct 1999

[14] ATOM project, funded by the European Union, 7th framework programme, Theme #7 Transport (including Aeronautics), Grant agreement no.: 218041. Website http://www.atom-project.net

[15] P. Lombardo, F. Colone, R. Cardinali, "Detection and Identification of Dangerous Materials for Airport Security", 2011. in G. Franceschetti, M. Grossi eds., "Homeland security Threats, countermeasures and privacy issues", pp. 173-199, Artech House